technische universität dortmund

astroparticle physics

We are number one

Searching for Gamma-Ray Emission from the Radio-Galaxy M87 in Data of the First Large-Sized Telescope of the Cherenkov Telescope Array Observatory

Lukas Nickel

2024

A document submitted in partial fulfillment
of the requirements for the degree of
Doctor rerum naturalium
at
TU Dortmund University, Department of Physics

Supervised by
Prof. Dr. Dr. Wolfgang Rhode and Prof. Dr. Johannes Albrecht

Abstract

Using the current-generation experiments of Imaging Atmospheric Cherenkov Telescopes (IACTs), a plethora of gamma-ray sources have been found in the sky. Nonetheless, there remain fundamental open questions in the field: How are cosmic rays accelerated? What can be learned about the extreme environments around black holes or supernovae? Will dark matter ever be found?

Fully solving these questions will require experiments that are much more sensitive than currently available as well as more advanced methods of data analysis. To this end, a new observatory is currently under construction: the Cherenkov Telescope Array Observatory (CTAO). The first prototype telescope, the Large-Sized Telescope Prototype (LST-1) on La Palma was inaugurated in 2018. It is since taking data and producing the first scientific results as part of the commissioning while more telescopes of the CTAO are built.

In this thesis, data from observations of the radio galaxy M87 taken with the LST-1 between April 2021 and January 2024 is analyzed using the low-level analysis pipeline for the LST-1, `lstchain`, and the CTAO science tool `gammapy`. A three-dimensional analysis is developed and performed, including the construction of three-dimensional background models. From the produced background models, it is apparent that the assumptions of radial symmetry are in general not fully met and more general forms need to be considered to describe the detector response. The measured excess from the position of M87 is not incompatible with the background expectation, so a detection of the source can not be claimed. However, modeling the measured excess, it is found to be consistent with previous measurents of the source during periods of low source activity.

Zusammenfassung

Eine Vielzahl von Gammastrahlungsquellen wurde milthilfe der aktuellen Generation von Imaging Atmospheric Cherenkov Telescopes (IACTs)-Experimenten gefunden. Dennoch verbleiben fundamentale Fragen offen: Wie werden die Teilchen der kosmischen Strahlung beschleunigt? Was können wir über die extremen Umgebungen nahe von schwarzen Löchern und Supernovae lernen? Wird die Dunkle Materie jemals gefunden werden?

Um diese Fragen zu beantworten, werden sowohl Experimente benötigt, die um ein Vielfaches sensitiver als die derzeit verfügbaren sind, als auch neue Methoden der Datenanalyse. Zu diesem Zweck wird derzeit ein neues Observatorium errichtet, das Cherenkov Telescope Array Observatory (CTAO). Der erste Teleskopprototyp, das Large-Sized Telescope Prototype (LST-1) auf La Palma wurde 2018 eingeweiht. Seitdem nimmt es als Teil des Inbetriebnahmeprozesses Daten auf und bringt erste wissenschaftliche Erkenntnisse hervor während die weiteren Teleskope errichtet werden.

In dieser Arbeit werden Daten aus Beobachtungen der Radioquelle M87 analysiert, die von dem LST-1 zwischen April 2021 und Januar 2024 aufgenommen wurden. Dazu kommen die low-level Software des LST-1, `lstchain`, und das CTAO Science Tool `gammapy` zum Einsatz. Eine dreidimensionale Analyse wird entwickelt und Modelle für die Untergrundabschätzung erstellt. Diese zeigen, dass die Annahme radialer Symmetrie im Allgemeinen nicht erfüllt ist und die Detektorantwort in einer allgemeineren Form beschrieben werden sollte. Der gemessene Überschuss aus der Richtung von M87 ist nicht inkompatibel mit der Untergrunderwartung, sodass eine Detektion der Quelle nicht möglich ist. Allerdings ergibt eine Modellierung des Quellüberschusses Ergebnisse, die kompatibel zu früheren Messungen von M87 während Phasen niedriger Aktivität sind.

In gamma-ray astronomy as a subfield of astroparticle physics, the most extreme phenomena and enviroments in the universe are studied by measuring the highly-energetic particles produced.

In the following sections, I will give a brief introduction into gamma-ray astronomy, starting with the history of the field in Section 1.1.

The scenarios leading to the observed emission of particles are still only partially understood, but some general classes of models and source types can be defined, some of which are explained in Section 1.2. In this thesis, most of the analysis focuses on the radio galaxy M87, which has been observed extensively in multiple wavelengths including multiple detections in gamma rays and the famous imaging of the central black hole. The current status of research is discussed in Section 1.3.

At the highest energies, gamma-ray astronomy is pursued with ground-based telescopes despite the fact, that the atmosphere is non-transparent to gamma rays. The underlying principles are presented in Section 1.4 from a general point of view, before then discussing the construction of the next-generation instrument, the Cherenkov Telescope Array Observatory (CTAO), and the telescope used throughout this thesis, the Large-Sized Telescope Prototype (LST-1), in Section 1.5.

1.1 Astroparticle Physics

Astronomy is one of the oldest forms of science pursued by humankind. In contrast to modern times, prehistoric cultures did not separate between astrology and astronomy and associated the objects in the sky with powerful beings that could change the course of the world. Some of the celestial objects are named after ancient gods to this day, such as the planets of our solar system.

They did, however, also perform complex calculations to understand the movement of planets and stars. Early civilizations closely observed the regular course of the moon, sun, and the planets to create calendars and find the best time to harvest. But even with the invention of the telescope in the seventeenth century, the sky was still only observed in optical wavelengths, which — as we know today — is only a small part of the electromagnetic spectrum as indicated in Figure 1.1.

It was not until the nineteenth century that astronomers extended upon this limitation with the observation of infrared radiation. As one of the first targets, the moon was observed in 1856 by Charles Piazzi Smith [3]. The existence of electromagnetic waves at other wavelengths was

known from Maxwell's equations [4], but technical limitations and an incomplete understanding of the role of the atmosphere held back further advancements.

A fundamental discovery and arguably the birth of astroparticle physics was the discovery of cosmic rays by Victor Hess in 1912 [5]. Trying to understand the mystery, that the level of ionizing radiation increases with height above the ground instead of decreasing as expected if the only source of radiation was terrestrial radioactivity, he concluded the existence of extraterrestrial radiation. From there on out, advancements in particle physics were closely tied to astroparticle physics, with both the positron and muon first discovered in cosmic rays by Carl David Anderson. These discoveries resulted in the 1936 Nobel prize of Physics shared between the two [6].

Radio-astronomy followed when Karl Guthe Jansky found the connection between a periodic radio signal, that interfered with plans of transatlantic voice communication, and the alignment of the antennas relative to the Sagittarius region of the Milky Way in 1933 [7].

The search for radiation in the X-ray regime could not be carried out from ground-based observations due to the absorption of the atmosphere. Before satellites could be used to search for X-rays, the US Army already launched rockets to detect radiation coming from the sun [8].

The same fundamental problem applies for gamma rays, requiring again observations from space. The first such telescope in orbit was Explorer-11, which detected 22 gamma-ray events over multiple months [9]. At first, only a diffuse gamma-ray background could be measured, but in 1979, a source of gamma rays was discovered in the form of a line-spectrum at 2.2 MeV originating from neutron capture during a solar flare [10].

Nowadays, a diffuse gamma-ray background is established, but also individual point sources have been measured with more than 7000 known sources listed in the fourth Fermi Large Area Telescope catalog (4FGL) [11]. The current knowledge of the diffuse fluxes from different particles measured with various experiments is summarized in Figure 1.2, which highlights a fundamental problem: The count rates decrease with higher energies, which restricts the statistics at these high energies. A consequence of this is, that detectors have to be larger to

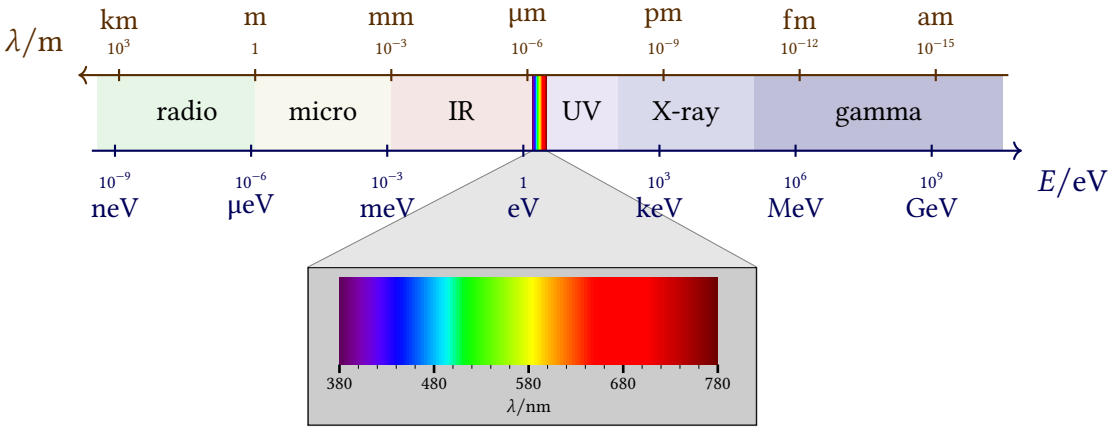

Figure 1.1: Spectrum of electromagnetic radiation. Visible light only makes for a small fraction of the observable wavelengths. Graphic adapted from [1, 2].

increase the collection area, but this is only of limited applicability to satellites, that need to be brought into orbit via rocket launches.

As a countermeasure to the low event rates of gamma rays at the highest energies, the technique of Imaging Atmospheric Cherenkov Telescopes (IACTs) was developed in the 1960s: While gamma rays do not reach the ground due to interactions with the atmosphere, they leave behind measurable signatures when entering the atmosphere due to the relativistic speeds of secondary particles produced in the process. The first such telescope, the Whipple 10m-telescope at Mount Hopkins University detected the Crab Nebula in 1989 [12]. Since gamma rays span such a large range of energies, one speaks of very-high-energy gamma rays at energies above $\approx$ 1 to 10 GeV, to differentiate from gamma rays at MeV energies, which are observed from space.

Apart from photons and charged cosmic rays, it is also possible to measure astrophysical neutrinos and gravitational waves. In all bands besides gravitational waves, scientists found evidence of an emission from the location of the Milky Way, so there is now an extensive image of our galaxy, as can be seen in Figure 1.3.

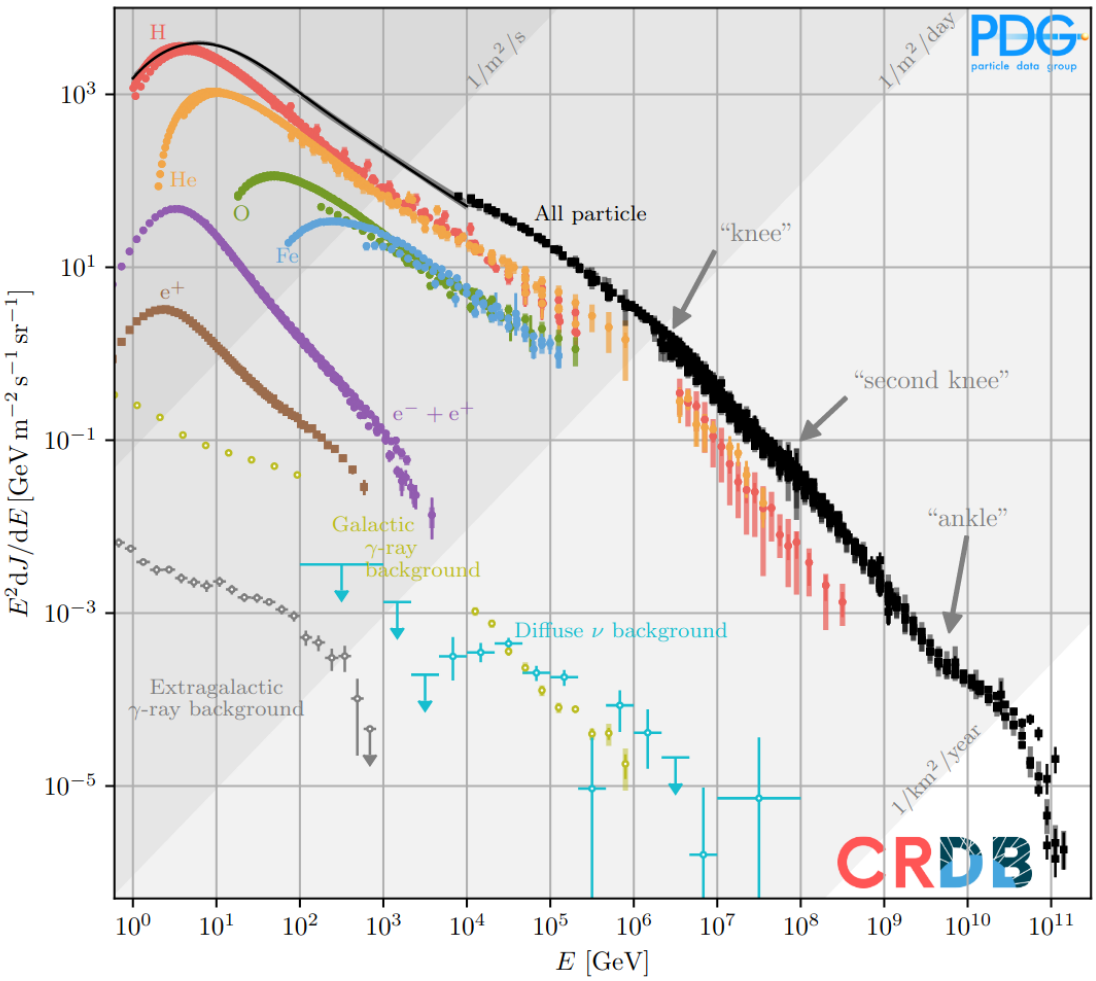

Figure 1.2: Spectrum of diffuse particle fluxes of cosmic origin over eleven decades in energy. Shown is both the all-particle spectrum with the characteristic features of the knee(s) and ankle and measurements of individual particle types. Charged cosmic rays are measured to much higher energies than gamma-rays and neutrinos, but even at lower energies, they are much more common. Graphic copied from [13].

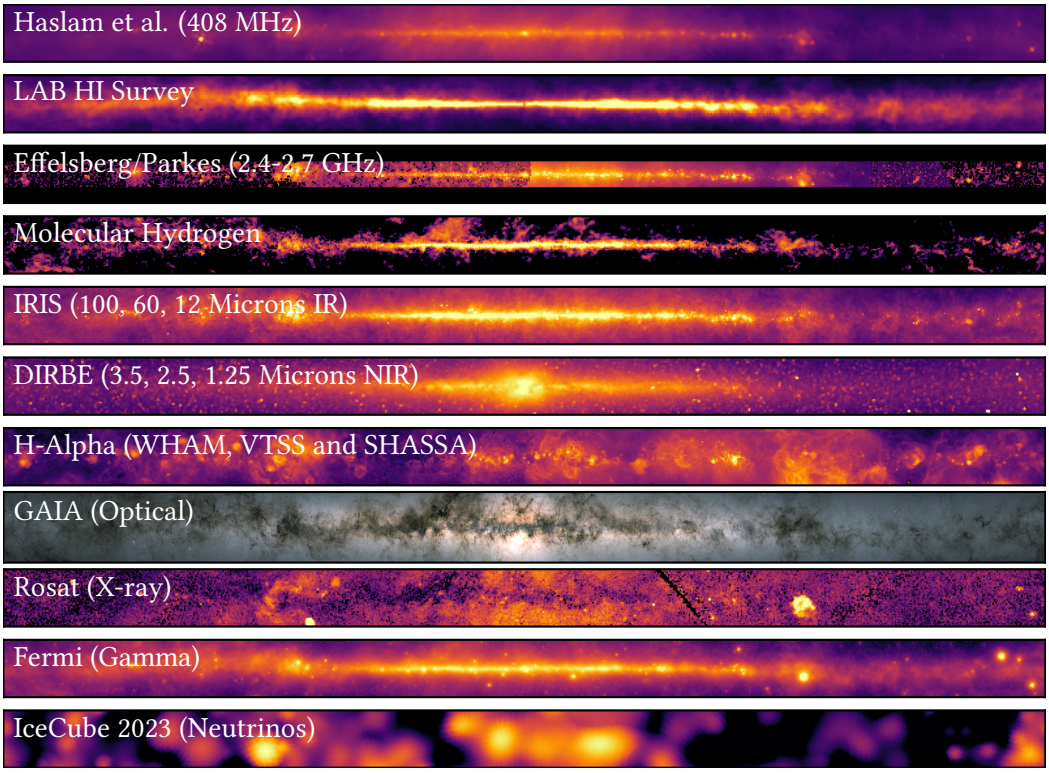

Figure 1.3: Observations of the center of the Milky Way using different messengers. Some features, such as absorbing dust clouds, can not be observed in all wavelengths. Graphic adapted from [14] with data from [15, 16, 17, 18, 19, 20, 21, 22, 23, 24, 25, 26, 27, 28, 29, 30, 31, 32, 33].

1.2 Origins of Gamma-Ray Emission

Particles at these extreme energies cannot be efficiently produced by thermal radiation: For stellar surface temperatures of a few thousand Kelvin, radiation is actually mostly emitted in the visible range as shown in Figure 1.4.

Instead, gamma rays are produced non-thermally, whereby the exact processes are still subject of current research. There exist, however, two general classes of explanatory approaches: Leptonic and hadronic production. In both cases, highly energetic charged particles experience energy losses in the form of emitting photons, which means they must first be accelerated.

For the emitted gamma rays to reach their high energies, the spectrum of charged particles needs to extent to energies far beyond what human-made accelerators can produce. The basic mechanism leading to these accelerations is believed to be Fermi acceleration, which is divided into acceleration of the first and second order [34, 35].

The main idea behind Fermi acceleration of the second order is that charged particles bounce between magnetic mirrors in the form of magnetized interstellar clouds and stochastically gain energy because the particle is moving relative to the mean movement of the clouds. If a particle with velocity v moves through a medium with arbitrarily arranged mirrors, it will hit a cloud with velocity v_c, at an angle of θ. The particle is assumed to be highly relativistic, whereas the

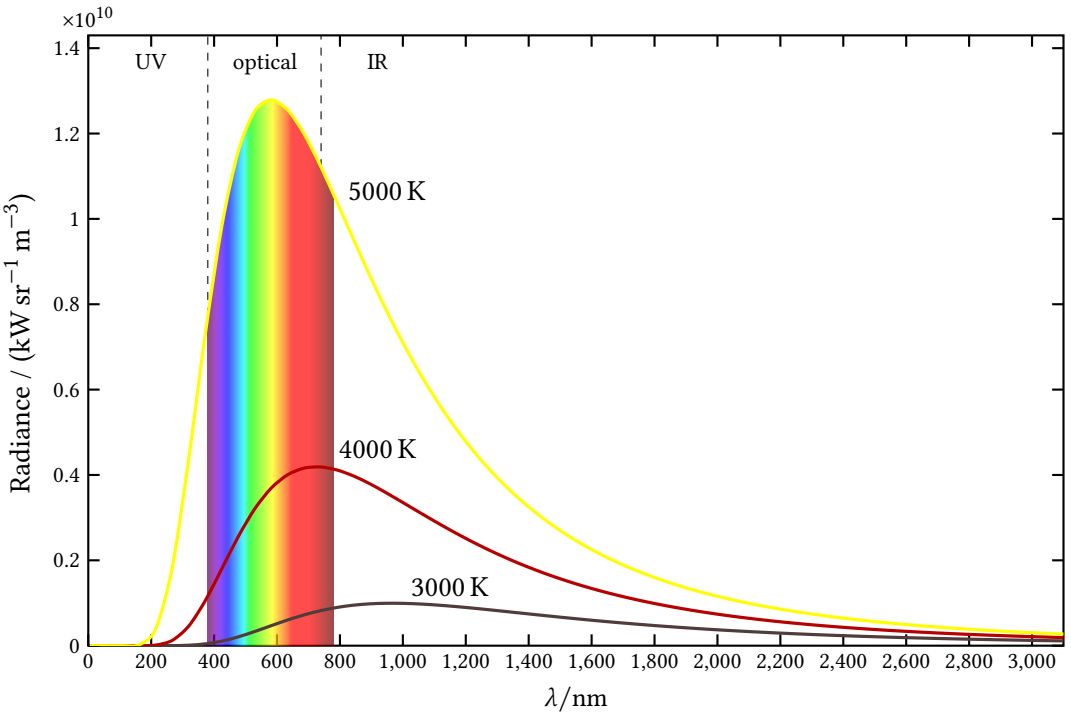

Figure 1.4: Spectral energy density emitted from an ideal black-body. Radiation occurs mostly at wavelengths at around the ones of visible light and extends only partially into the ultraviolet regime.

cloud's velocities are on the order of a few $\mathrm{km\,s^{-1}}$.

Each collision then provides a fractional energy gain of

$$\frac{\Delta E}{E} = 2v_\mathrm{c}\left(v\cos\theta + v_\mathrm{c}\right), \tag{1.1}$$

which can also lead to a decrease in energy depending on θ.

While there might be no preferred orientation of the clouds in the observer's frame, the velocity of the cloud projected on the direction of the particle's movement is $v_\mathrm{c}\cos\theta \neq 0$. For this reason, the probability that a collision occurs under an angle θ is

$$\mathrm{d}P(\cos\theta) \propto (1 + v_\mathrm{c}\cos\theta)\,\mathrm{d}\cos\theta. \tag{1.2}$$

This means that collisions with projected velocities opposite to the particle's direction – which are the ones gaining energy – are more likely to occur than the other way around.

It can further be shown that the average energy gain per collision is

$$\frac{\Delta E}{E} \propto \frac{v_\mathrm{c}^2}{c^2}. \tag{1.3}$$

Thus, particles can, in fact, gain energy in a randomly distributed system of magnetized clouds. According to Equation 1.3, the gained energy is minimal, though, as it only scales to the second order in the cloud velocities.

However, if the clouds were moving fast in a preferred direction, most collisions would occur such that $\cos\theta > 0$ and the first term in Equation 1.1 dominates the energy gain. With that, the energy gain could be as efficient as $\propto v_c/c$, which is why it is called the first-order Fermi mechanism. These conditions would be met if the particles are accelerated through diffuse shock-fronts [36]. While the details are intricate to probe, it is generally accepted that such shock fronts can occur in astrophysical contexts, for example, through supernova explosions.

In **leptonic models**, gamma rays are then produced from highly energetic electrons through synchrotron radiation and inverse Compton scattering. Synchrotron radiation occurs due to the movement of the charged particle through an interstellar magnetic field: Similar to ordinary bremsstrahlung, where the particle is accelerated tangentially to its direction, it is accelerated perpendicular through the Lorentz force. Synchrotron radiation occurs for all charged particles, but the power carried by the radiation decreases sharply with increasing particle mass according to the relativistic Larmor formula [37]:

$$P_\gamma \propto \frac{\beta^4\gamma^4}{r^2} \propto m^{-6}. \tag{1.4}$$

The emitted power is, therefore, much lower for particles heavier than electrons, such as protons.

Additionally, gamma rays are produced through the process of inverse Compton scattering: In ordinary Compton scattering, a photon collides with a resting electron. Through the collision, not only the direction is changed, but the photon also transfers part of its energy to the electron. If the electron is not at rest but is instead at relativistic velocities, the same scattering process can transfer energy from the electron to the photon. This way, a low-energy photon field, which could, for example, stem from starlight or the Cosmic Microwave Background (CMB), can be upscattered to much higher energies.

In the **hadronic model**, gamma rays are produced instead starting from an initial proton spectrum. If gamma rays are dominantly produced from protons, one would expect to see a bump from neutral pions because the decay $\pi^0 \to \gamma\gamma$ produces a line spectrum in the rest frame of each pion. This line is smeared out in the rest-frame of the observer because the kinetic energy of the pions differs and becomes a bump in the spectrum.

Another hypothetical source of gamma-ray emission is as a byproduct of the decay or annihilation of dark matter. While dark matter particles are generally constructed not to interact electromagnetically, they could produce standard-model particles via weak interactions. These would then produce measurable photon fluxes in energy ranges that depend upon the mass of the dark matter particles. Since the parameter space for a possible dark matter particle is vast, observations in different wavelengths are carried out to either detect an emission without a known point source or constrain the parameter space by setting limits on the interaction cross-section (for example, in [38, 39]). So far, the only hint towards actual emission from dark matter comes from the Fermi Gamma-ray Space Telescope, but its significance is disputed given the systematic measurement uncertainties [40, 41, 42, 43].

A prominent class of gamma-ray sources are Active Galactic Nuclei (AGNs). AGN are supermassive black holes at the center of galaxies with masses up to several billion solar masses [44]. While supermassive black holes are at the core of most galaxies; only a few emit radiation, which seems to be related to the active accretion of matter in these objects [45]. In that

case, the accretion disk heats up and can produce highly energetic photons. In addition, some AGN also produce a relativistic outflow of matter perpendicular to the plane of the accretion disk. This is illustrated in Figure 1.5. These "jetted" AGN can also be detected at gamma-ray energies if the jet points towards the Earth because the photons then appear doppler-boosted. In some cases, AGN have also been found to emit gamma rays even if the jet is not aligned with the direction of the Earth [46].

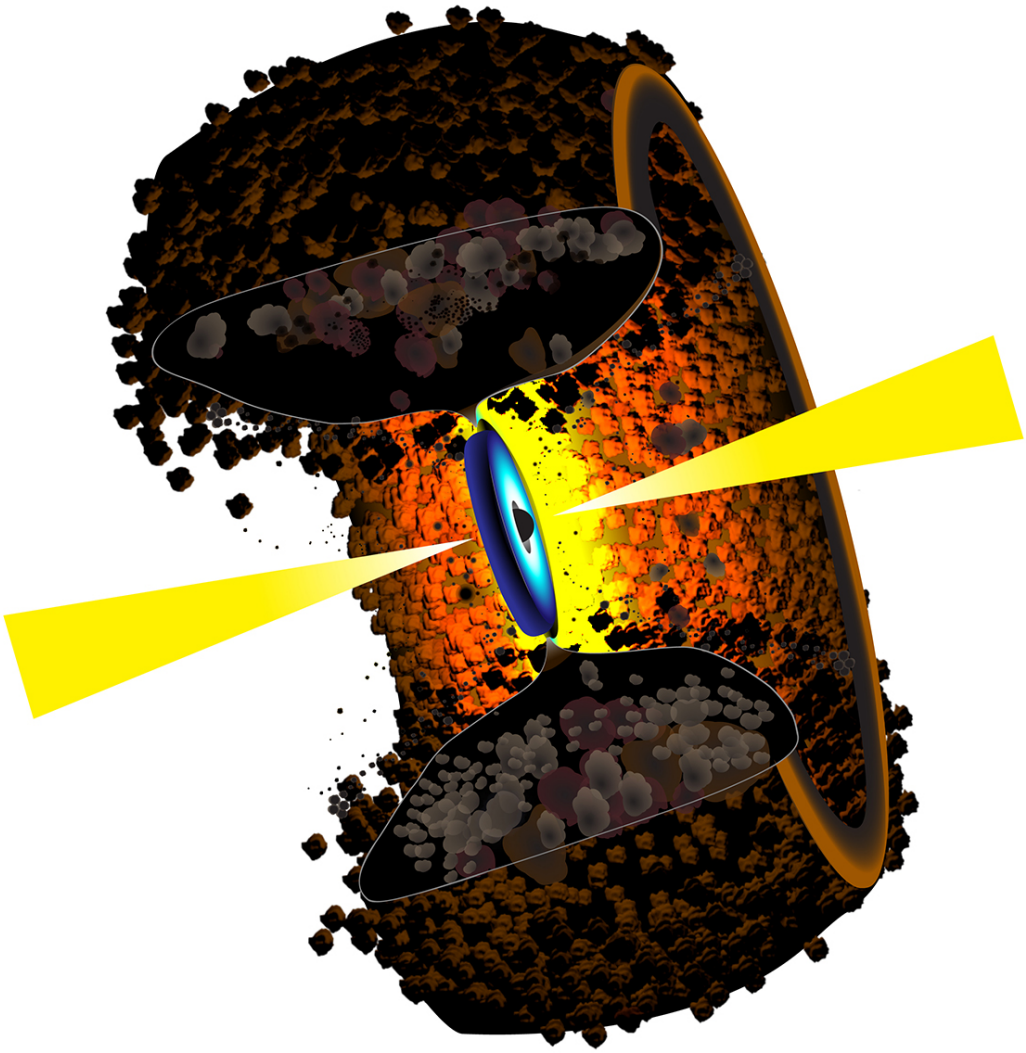

Figure 1.5: Artist's conception of the dust torus surrounding a supermassive black hole. The accretion disk rotates around the black hole and heats up through collisions. A jet of highly energetic particles is produced perpendicular to the plane of the accretion disk in both directions [47].

Once gamma rays have been emitted, their propagation to the Earth is relatively straightforward: Magnetic fields do not affect the path the photon follows so measured gamma rays can be attributed to a source measured in other wavelengths. This is in contrast to charged

cosmic rays, where the information about the source position is nearly completely lost due to our ignorance about the precise distribution of the galactic and intergalactic magnetic fields. Only at the very highest energies do the gyroradii get large enough to say anything about the original direction [48].

1.3 M87 - A Supergiant Galaxy

M87 is the eighty-seventh source listed in the extended version of the original Messier catalogue [49]. Upon its detection in 1781, it was first classified as a nebula, but it is, in fact, one of the most giant galaxies in the local universe. Unlike our galaxy, the Milky Way, M87 does not have any spiral arms but is instead considered an elliptical galaxy following the findings of Edwin Hubble [50].

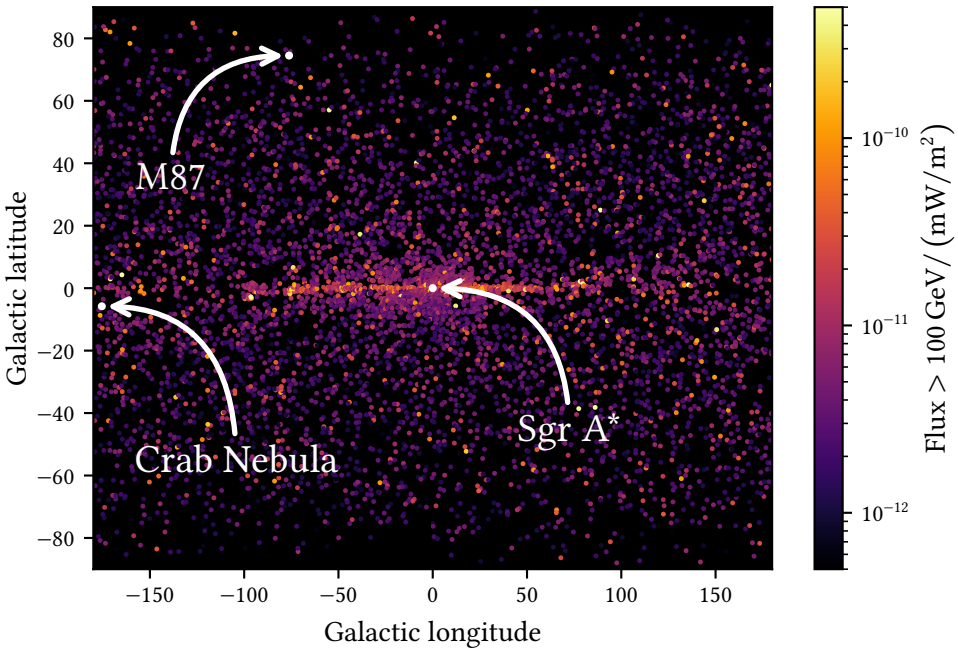

Figure 1.6: Location of the source M87 in galactic coordinates with all sources in the fourth Fermi Large Area Telescope catalog (4FGL) [11]. Gamma-ray sources have been found in all directions of the sky, but at the position of the Milky Way at 0 deg latitude, a clear excess in the number of sources can be made out. M87 is located far from the galactic disk, reducing the risk of contamination during measurements.

M87 is considered to be located at the center of the Virgo galaxy cluster, which hosts over a thousand individual galaxies [51]. The distance to earth is small in astronomical scales with common estimates ranging from 15 Mpc to 17 Mpc [52] and the line-of-sight (l.o.s.) is not obstructed by the disk of the Milky Way as illustrated in Figure 1.6. Because of this, M87 has been observed extensively in different wavelengths.

Multiwavelength observations

The AGN of M87 has first been observed at radio frequencies in 1947 [53]. At this point, the source was still called Virgo-A, which was later found to be at the position of the core of M87 [53]. In radio frequencies, a jet is known to exist, and further large-scale outflows of matter have been observed as can be seen in Figure 1.7.

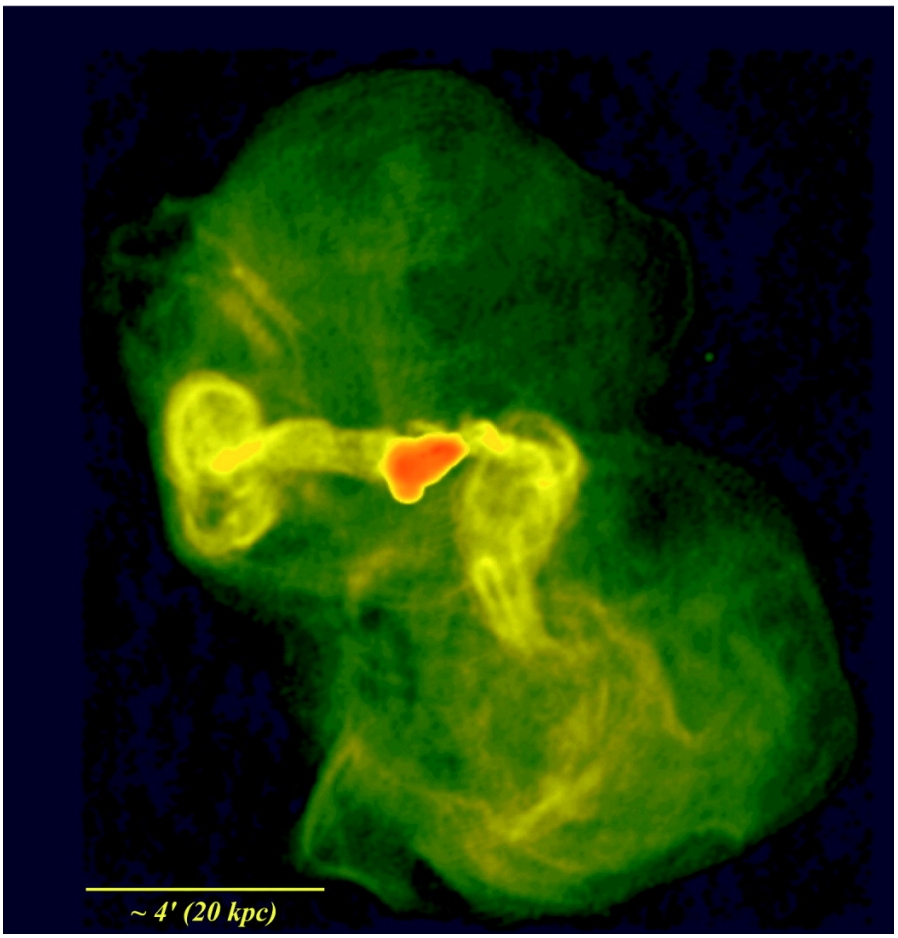

Figure 1.7: Image of the central region of M87 in radio-waves at 90 cm. The structure can be seen outside the innermost region (red-orange), where the jet is located. Image taken from [54]. Note that a distance of 17 Mpc is assumed in the analysis, leading to slight differences in the conversion from angular distances to kpc.

The black hole itself was also famously imaged by the Event Horizon Telescope (EHT) in 2017 [55]. A revised image is shown in Figure 1.8.

M87 was identified as a source of X-ray radiation through rocket missions in the 1960s [56].

Later observations found a clear structure in the jet that matches the features found in optical and radio measurements [57].

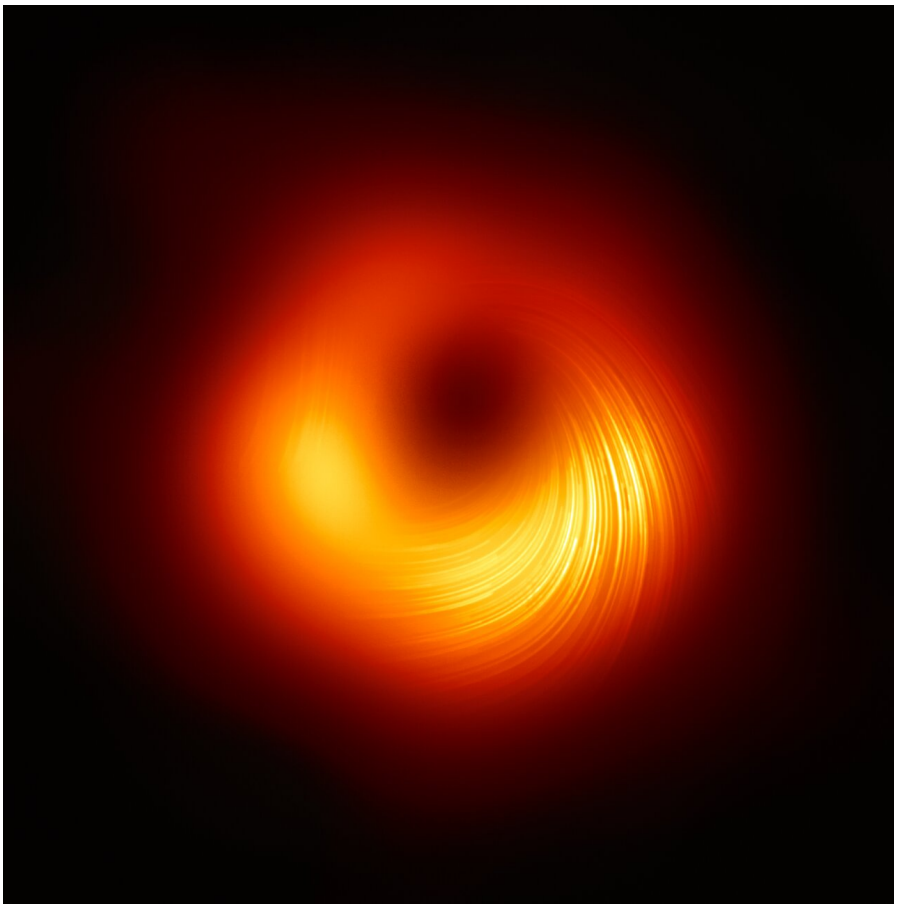

Figure 1.8: The black hole at the center of M87 in polarized light. Image published by the EHT collaboration [58].

Gamma Ray Observations

Since the jet of M87 is not pointed towards Earth, it is not apparent why gamma rays should be emitted from M87. Nevertheless, M87 was detected as a source of gamma-ray emission in 2003 at energies ≥ 730 GeV by the HEGRA observatory [46].

From there on out, different experiments confirmed the detection. Furthermore, it was found that the flux is not constant over time with the observation of a high-state in 2006 and possible day-scale flux variations [59].

In 2008, VERITAS detected M87 at energies above 250 GeV [60]. The temporal correlation between the gamma-ray flare and a flare in X-rays from the core region implies that the measured gamma rays also come from this region instead of secondary positions in the jet.

In 2009, the Fermi Gamma-ray Space Telescope observed M87 also at lower energies of 100 MeV and above [61].

From 2012 to 2015, MAGIC found the flux at longer timescales to be constant [62]. During these low-states, M87 is a pretty dim source, just at the edge of detectability for IACTs.

At gamma-ray energies, sources can not be resolved to the same precision yet. When talking about the source M87 in this thesis, the position of the AGN from radio-observations is therefore used, which is at a right ascension of 187.706 deg and a declination of 12.391 deg in the International Celestial Reference System (ICRS) [63] with an adopted distance of 16.5 Mpc.

1.4 Ground-Based Gamma-Ray Astronomy

The Atmosphere as Detector

The atmosphere is not transparent to photons at all energies. Only select wavelengths arrive at the ground, namely visible light and radio waves.

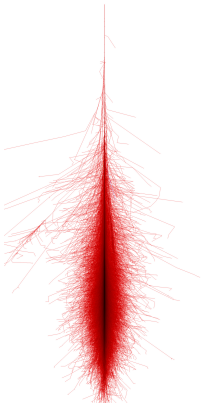

1 TeV gamma-ray shower [64].

While this makes it challenging to perform ground-based observations at wavelengths outside these windows, it effectively makes the atmosphere a giant calorimeter in which the particles deposit their energy leading to large detector volumes if one can integrate the atmosphere into the detector: When such an incoming particle arrives at Earth and if its energy is high enough, the interactions in the atmosphere produce secondary particles whose traces can be reconstructed to obtain information about the primary particle, that entered the atmosphere.

In the case of highly energetic photons, the presence of nuclei leads to pair production of a relativistic electron–positron pair. These produce additional high-energy photons via bremsstrahlung, which can pair-produce again leading to a cascade of electrons, positrons, and photons [65]. This simplified model of shower development is shown in Figure 1.9. It essentially leads to a doubling of particles in each epoch with evenly distributed energies until the photon energy falls below the energy threshold for pair production.

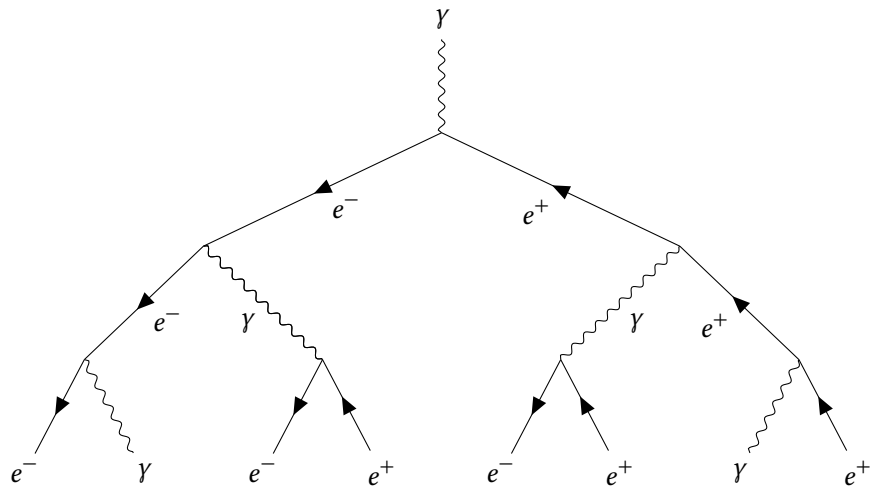

Figure 1.9: Illustration of the development of an electromagnetic shower in the atmosphere. A highly energetic photon enters the atmosphere from above and produces a cascade of secondary particles through repeated processes of bremsstrahlung and pair-production.

In contrast, hadrons can interact via the strong force and thus produce more complex showers with different secondary particles. Most of these have higher masses than electrons, and their interactions produce higher transversal momenta. For this reason, hadronic showers are more spread out compared to electromagnetic ones of the same total energy.

There are, however, also always electrons produced in a hadronic shower, and once an electron or photon is produced, it again generates an electromagnetic subshower as illustrated in Figure 1.10. For this reason, hadronic showers are the main background for ground-based gamma-ray telescopes.

Depending on particle energy and atmospheric properties, a typical air-shower forms at a height of ≈ 8 km to 10 km above sea level [66]. A detector to measure these interactions would preferably be located at high altitudes because the energies of the particles quickly fall below the detection threshold.

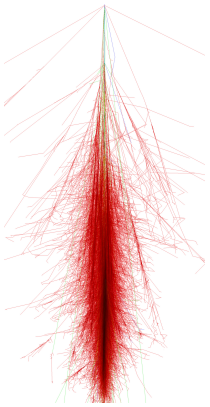

1 TeV proton shower [64].

At energies above a few TeV, these showers can actually extend to multiple km and the secondary particles can reach the ground, where they can be measured. An example of an experiment measuring these showers is the HAWC observatory, which uses water-tanks at 4100 m above sea level [67].

With IACTs, a different approach is taken: Instead of measuring the particles that reach the ground, they measure the Cherenkov radiation, that is emitted during the traversal through the atmosphere, which can travel much further. For this reason, the shower does not need to extend all the way to the ground and the observable energy range extends down to a few GeV.

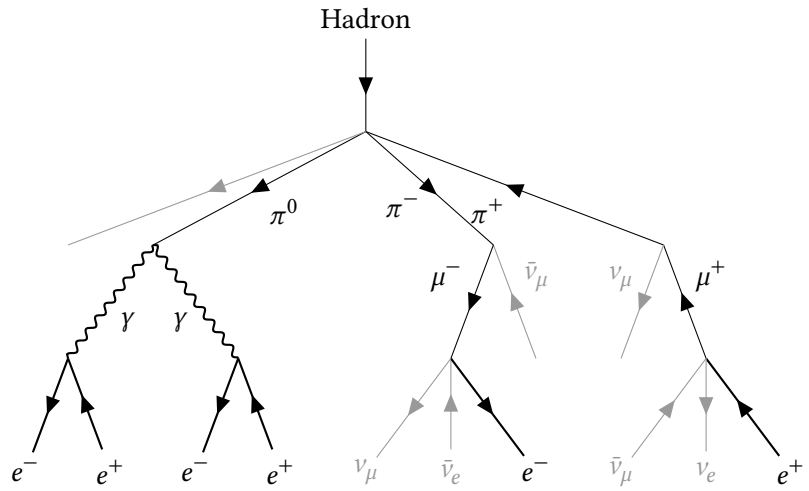

Figure 1.10: Illustration of the development of a hadronic shower in the atmosphere. Only the most relevant interactions for the generation of electromagnetic subshowers are drawn. Through interactions via the strong force, neutral and charged pions are produced. At energies observed with IACTs, their lifetime is too short to reach the ground. Electrons and photons are produced through different decay processes, producing electromagnetic subshowers.

Cherenkov Radiation

Cherenkov radiation occurs due to the interaction of relativistic charged particles with dipole moments in the surrounding matter [68, 69]. In an air shower, it is produced by the charged secondary particles that exceed the local speed of light c.

Calculating the full Cherenkov light that is produced from a shower requires complex simulations of the shower development and the interactions of the emitted radiation in the atmosphere [70]. Here, only a simple derivation is discussed to motivate the measurement process of IACTs with some assumptions:

In an electromagnetic shower, the only charged particles are electrons and positrons. The different secondary particles do not interact with each other in any significant way, and their mean free path length is small in the atmosphere. The effect of the Earth's magnetic field is ignored.

With this, the first relevant block is the Cherenkov light emitted by a single electron, but this can also be extended to electron bunches (see e.g. [69]).

Starting from the Lienard-Wiechert potential of a single electron in cylindrical coordinates, the z-component of the electrical field (in the direction of the shower development) in a distance r is given in Equation 1.5 with α in Equation 1.6 with the Modified Bessel function of the second kind K_0.

$$E_z(r,\omega) = i\omega\frac{e\mu_0}{2\pi}\left(1-\frac{1}{\beta^2}\right)K_0(\alpha r)e^{\left(\frac{i\omega z}{\beta c}\right)} \tag{1.5}$$

$$\alpha = -\frac{\omega}{c}\sqrt{\left(\frac{c}{v}\right)^2 - 1} \tag{1.6}$$

The near field is not of interest as the telescopes are kilometers away from the interactions, so the far-field limit is applied in Equation 1.7. This leads to the requirement of a complex α to end up with radial waves, which is fulfilled if $v > c_0$, meaning the particle moves faster than the local speed of light.

$$|\alpha| r \gg 1 \tag{1.7}$$

$$K_0(\alpha r) \propto \sqrt{\pi/2\alpha r}\, e^{-\alpha r} \tag{1.8}$$

Further approximating the behavior of the atmosphere as a medium with a constant index of refraction of $n = 1.000293$, an electron exceeds the local speed of light at a few MeV, which is shown in Figure 1.11. As at least two electrons are produced in the shower, this translates to a primary gamma energy of at least a factor of two higher. This gives an absolute lower bound for the detectability of gamma rays using IACTs within the validity of this approximation. In practice, the emitted photon intensity needs to be high enough to trigger the telescope, so multiple generations of electrons in the shower need to exceed this energy leading to higher energy thresholds.

With the far-field limit applied, the electric field is then given by Equation 1.9:

$$E_z \propto e^{i(k_r r + k_z z)} \tag{1.9}$$

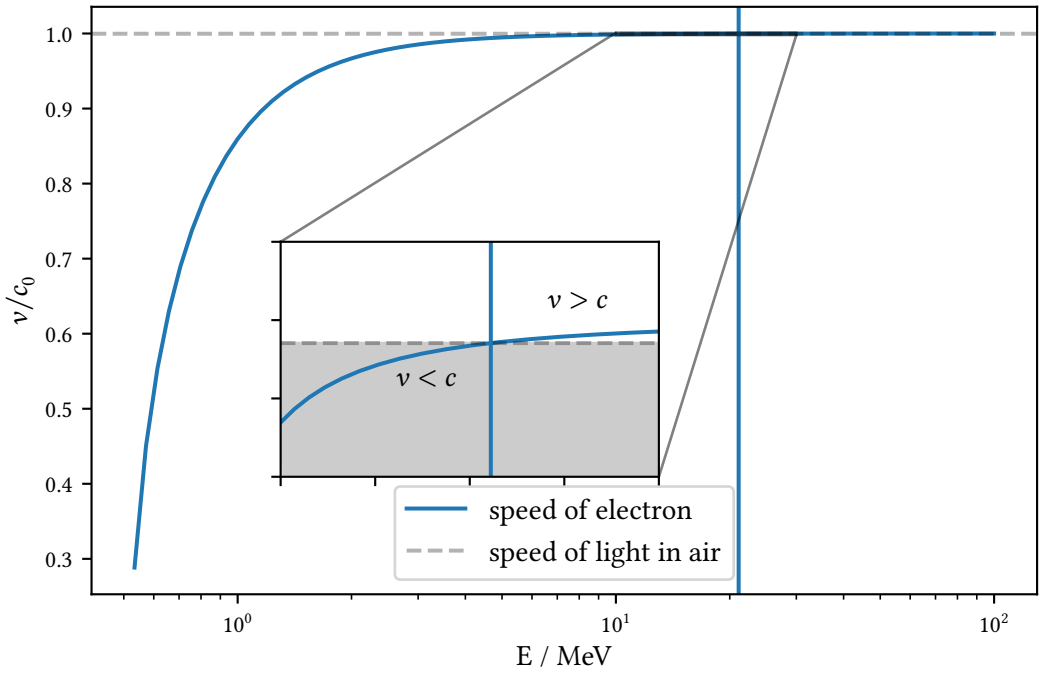

Figure 1.11: Speed of electrons at a given kinetic energy. At around 20 MeV, the electron's velocity exceeds the local speed of light and Cherenkov light can be emitted.

The Cherenkov angle, which is the angle under which the light is emitted with respect to the direction of the charged particle, then immediately follows as

$$\Theta_c = 90\,\text{deg} - \arcsin \frac{k_z}{\sqrt{k_r^2 + k_z^2}} \tag{1.10}$$

$$= 90\,\text{deg} - \arcsin \frac{1}{\beta n(\omega)}. \tag{1.11}$$

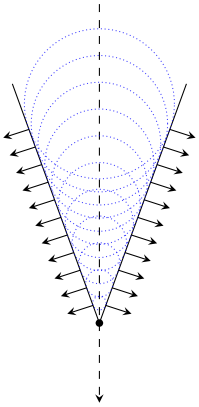

Using again the constant refraction index of air $n = 1.000293$, the Cherenkov angle follows as $\Theta_c \approx 1.5$ deg. This simplified derivation ignores absorption in the medium and any corrections from the near-field but holds well enough to understand the phenomenology of IACTs.

The main fraction of faster-than-light electrons and with that the emitted Cherenkov light is created at about 10 km above sea level. A vertical gamma-ray shower would thus create a circular footprint with a radius of $\tan(1.5\,\text{deg}) \cdot 8\,\text{km} \approx 200\,\text{m}$ if the observatory is located at 2 km above sea level.

The emitted light is not monochromatic, although Cherenkov light is often associated with blue light. In fact, all wavelengths contribute, with higher wavelengths carrying more of the emitted energy loss up until a cutoff depending on the particle's energy. This connection is expressed with the Frank-Tamm formula in Equation 1.12 [71]:

$$\frac{\partial^2 E}{\partial x \partial \omega} = \frac{1}{4\pi} \mu(\omega) \omega \left(1 - \frac{1}{\beta^2 n(\omega)^2}\right). \tag{1.12}$$

In the kilometers between the emission of the radiation and its measurement on the ground, absorption through the atmosphere can no longer be ignored, though. In Figure 1.12 the effect of the wavelength-dependent transmissivity of the atmosphere on the measured spectrum is displayed. The light reaching the telescopes peaks in the blue to near-ultraviolet range of the spectrum.

Since the index of refraction in air is close to 1, the temporal delay between photons emitted early in the shower and photons emitted later is small, with a typical shower producing a flash of light that lasts for only a few nanoseconds. The optical system of an IACT therefore has to be able to measure very faint and short signals in the near-UV to the optical range.

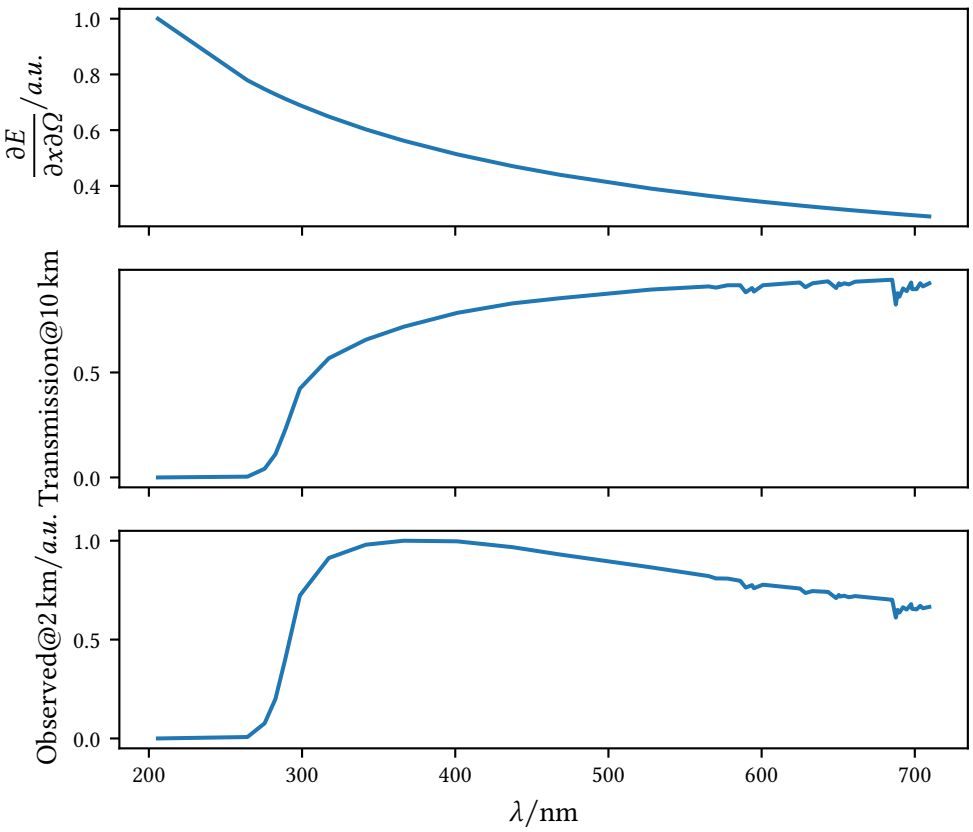

Figure 1.12: Cherenkov light produced by a single electron at c_0 in 10 km height. Top: Emitted radiation assuming constant permeability μ and index of refraction n for air according to the Frank-Tamm formula from Equation 1.12. Middle: Transmission of a standard tropical summer atmosphere from 10 km to 2.2 km in height. The profile is extracted from [66]. In practice, conditions are different between seasons and observation sites. Bottom: Remaining light that reaches the observatory. The ultraviolet part of the spectrum can not travel through the atmosphere so the measured spectrum peaks at blue wavelengths.

Optical systems

At its core, an IACT is an optical telescope observing not the primary particle itself but the light emitted in the atmosphere, so standard principles apply to the construction of the optical system. Since the light pulses are so faint and short, IACTs are built at places with little light pollution and can only observe during the night.

The first decision in the construction of an IACT is the one of the mirror design: One wants to be able to resolve the time structure of the shower, so the time dispersion of the mirror should be on the order of nanoseconds or less. At the same time, showers are not only observed head-on, so off-axis performance has to be a consideration while also keeping costs down.

Most IACTs base their mirror on a parabolic design but segment the mirror into smaller tiles to enable larger mirror areas. This design is simple to build and also makes for the shortest Cherenkov peak [70, 72]. The same design is also what is used for the Large-Sized Telescopes (LSTs) [73].

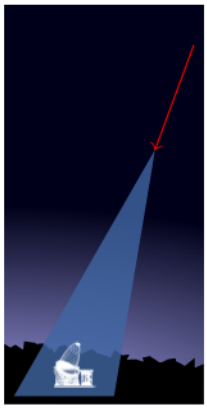

More complex mirror designs exist but are too expensive and difficult to employ for very large telescopes. In the upcoming Cherenkov Telescope Array Observatory (CTAO) , multiple different designs will be used. Besides the parabolic mirrors, also Davies-Cotton [74] and Schwarzschild–Couder [75, 76] designs will be used in the other telescope-types [72] due to their different requirements.

Shower images

To first order, the shower axis is a line that intersects the ground somewhere in the Cherenkov light pool that is emitted in a cone according to Equation 1.10.

This is illustrated in Figure 1.13 with two showers observed under different angles: The telescope is able to observe the shower if the Cherenkov cone on the ground includes the telescope's location. Depending on the impact distance and the angle under which the camera sees the shower, observed image will be more or less elongated and show an asymmetry along the shower axis.

Because a telescope can only ever observe the shower from one side, current-gen experiments use multiple telescopes. This way, multiple images of the same shower can be recorded simultaneously, which increases the reconstruction quality.

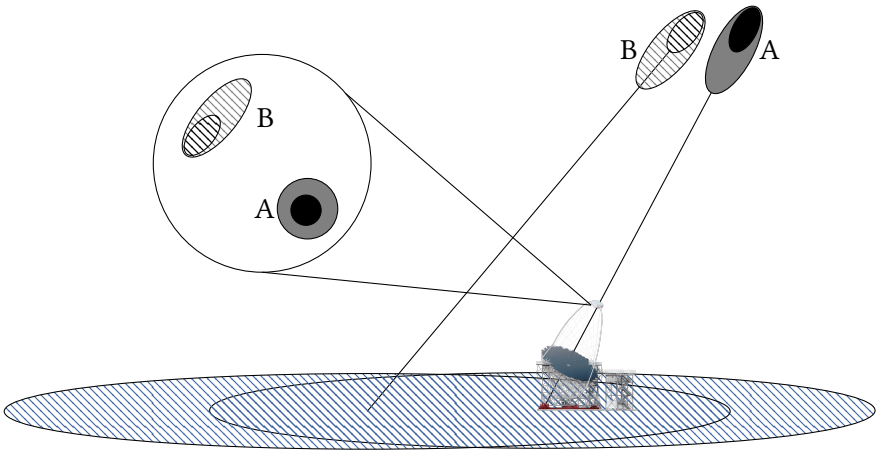

Figure 1.13: Illustration of two showers observed by the LST. The color-coding shows the intensity distribution with darker colors equating to higher intensities. Shower A hits the telescope head-on, leading to an almost circular image in the camera (upper left). The impact of shower B is further away from the telescope. The shower is observed from the side, leading to a more elliptical image with a clear asymmetry in the intensity distribution. Image recreated after [77].

1.5 CTA and LST-1

The Cherenkov Telescope Array Observatory (CTAO) aims to expand on the idea of using multiple telescopes in a few key ways [72]:

Besides combining telescopes of the same type, different telescope types will be used. This allows to extend the observable energy range beyond what a single mirror/camera combination can achieve: While low-energy showers occur often, they are challenging to observe because the amount of Cherenkov light generated is limited. Telescopes need to be able to collect a lot of light, which requires large mirrors, which drives up the cost of construction. At higher energies, individual showers are easy to observe even with smaller mirrors, but they happen rarely. To increase the rate of observed events, a larger area has to be covered with telescopes, which requires a large enough construction site and more telescopes.

In total, three classes of telescopes are foreseen to be part of the CTAO with the main differentiating factors listed in Table 1.1. The LSTs are the largest telescopes in the array and currently the second-largest IACTs with an effective mirror area of 370 m^2 losing out only to the central telescope of the High Energy Stereoscopic System (H.E.S.S). With this, it is supposed to provide the best sensitivity in the lower-energy range of the CTAO starting from 20 GeV, while the smaller MSTs and SSTs are more sensitive at higher energies. Additionally, CTAO is constructed on two sites for a larger simultaneous coverage of the sky: The southern site is located in the Atacama desert in Chile, close to the existing Paranal Observatory of the European Southern Observatory (ESO). In the approved alpha configuration, the array will consist of fourteen MSTs and thirty-seven SSTs with prepared foundations for four LSTs, that might be built in the future.

The northern site is located on the canary island of La Palma on top of the Roque de los

Table 1.1: Basic data of the different telescope types in the CTAO.

Type	Mirror diameter	Focal length	Main energy-range	Mirror design
LST	23 m	28 m	20 GeV-150 GeV	Parabolic
MST	11.5 m	16 m	150 GeV-5 TeV	Davies-Cotten
SST	4.3 m/1.8 m	2.15 m	5 TeV-300 TeV	Schwarzschild-Couder

Muchachos next to the existing MAGIC telescopes. There, the space is more constrained, and the planned array is smaller with no SSTs. In the alpha configuration, four LSTs and nine MSTs are foreseen with the first telescope, the Large-Sized Telescope Prototype (LST-1) already in operation.

Once fully constructed, the sensitivity of the full array is expected to surpass the current generation of observatories by an order of magnitude, while increasing the observable energy range to 5 GeV to 300 TeV [72, 78].

The construction of LST-1 was finished in 2018. Since 2019 the telescope is actively taking data as part of the commissioning process and is already publishing its first scientific results [79, 80].

Figure 1.14: Photo of the LST-1 in the parking position during daytime in 2022. The camera is resting on the camera tower (left) and the mirrors are defocused.

Before conclusions about the distribution of observed gamma rays can be drawn, several steps have to be performed. These steps are loosely separated by the use of different datalevels as laid out in Section 2.1: First, Section 2.2 explains how the measured charges are digitized and analyzed on a per-pixel basis before the recorded images are prepared for further reconstruction in Section 2.3.

At this point, the quality of the observed data is assessed in Section 2.4 in order to avoid having data taken under problematic conditions in the final dataset.

To reconstruct the properties of the primary particle from the recorded shower images, machine-learning models trained on simulations are used. Section 2.5 describes how the problem is approached and how different properties of the images relate to the different reconstruction tasks.

Not only can models be trained from simulations, but simulating the experiment is also important to estimate the instrument response. In Section 2.6, the way this general problem is broken down into multiple components for IACTs is explained.

The models and selection cuts evaluated on simulations can then be applied to the observed data, which is done in Section 2.7 along with preliminary estimates of the source excess. To get a proper estimate, the background has to be estimated, which is so far not possible using only simulations. In Section 2.8, ways to construct a model for the background acceptance from observed data are discussed and models are build for the observations in this analysis.

2.1 Datalevels

The analysis of IACT data is a complex multi-stage process due to the indirect nature of the measurement:

1. The sources are far away and there is no ground truth to any measurement.
2. Using the atmosphere as a medium introduces systematic issues beyond direct control.
3. Most of the recorded events are of hadronic origin.

As a result, analyses are heavily dependent on simulations and supervised machine-learning methods, and there are many steps between the raw observed data and science-ready event lists.

Data levels are used to describe which steps have already been performed on the data. In the following, the use of lower-level data levels, which describe the initial handling of the observed data, is based on the definitions for CTAO [81] but avoids some of the details. In particular, the focus here is on how the measured data itself is transformed and reconstructed. The structure of auxiliary information, such as the telescope pointing in the files of a given data level, is sometimes implied but not discussed to the full extent. It has to be noted that LST-1 only roughly follows the structure defined for CTAO, but the concepts still apply.

From raw data-level 0 (R0) up until datalevel 3 (DL3), steps specific to the observing telescope and to the observation are performed with the goal to reconstruct the properties of the primary particle that initiated the atmospheric shower, from the voltage curves readout in the camera of the telescope. This part of the analysis is mostly done using the LST-1-specific low-level analysis pipeline `lstchain` [82, 83], which, amongst other general ones, is built on top of the scientific Python packages `numpy` [84], `scipy` [85], `scikit-learn` [86], `pandas` [87], `matplotlib` [88], the (gamma-ray) astronomy packages `gammapy` [89], `pyirf` [90], `astropy` [91], and the low-level data processing pipeline software for the CTAO, `ctapipe` [92]. Most of these packages are also used on their own throughout this analysis.

In the future, `ctapipe` is foreseen to handle the data from all telescopes of the CTAO, but to accommodate the specific needs of LST-1 during the commissioning, the additional project was created.

The final DL3 data follows the open gamma-ray astro data format (OGADF) [93] and is used in `gammapy` to model the source properties.

2.2 Raw Camera Data

Flashes of Cherenkov light are very dim and last only a few nanoseconds requiring the use of specialized photon detectors and analog-to-digital converters (ADCs) for the camera setup. In the case of LST-1, each of the 1855 pixels in the camera contains a photomultiplier tube (PMT) of type Hamamatsu R11920-100-20.

PMTs are able to measure single-photon signals using a combination of the photoelectric effect and a high voltage setup in an evacuated tube: If photons hit the photocathode, they can release an electron from the material. The free electron is then directed towards one or more dynodes, which are held at a positive potential, thereby accelerating the electron. It then hits the dynode and releases multiple electrons through secondary emission. This process is then repeated at every dynode until the anode is reached, where the large group of electrons can be measured as an electric current.

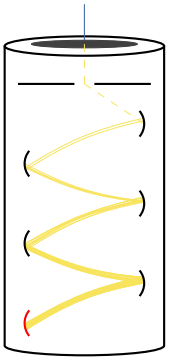

The material of the photocathode is one of the defining properties of the spectral response of the detector, which in the case of LST-1 is a bialkali material allowing the PMT to hit peak quantum efficiencies above 35% in the range of 300 nm to 550 nm [94], in which most of the Cherenkov photons arrive.

Each PMT connects to a high-voltage power supply and a preamplifier circuit specifically designed for CTAO [95]. Together, these form a pixel unit, which is then equipped with a hexagonal light guiding cone attached to the front. A complete pixel unit is illustrated in Figure 2.1.

Every seven pixel units form a module with a shared readout system. Besides the pixels, each module consists of a slow control board, the readout board with the main amplifier and the ADC conversion and a backplane [97]. A full assembly is shown in Figure 2.2.

Before the signal is digitized, the preamplified analog signal is fed into the main amplifier, which creates a low gain, high gain, and trigger line per pixel unit. For the sampling of the low and high gain channels, LST-1 utilizes the Domino Ring Sampler 4 (DRS4) chip, which is is the fourth version of a custom integrated circuit initially developed for the MEG experiment [98]. It can digitize up to eight analog signals at a time in a switched capacitor array with 1024 cells [99]

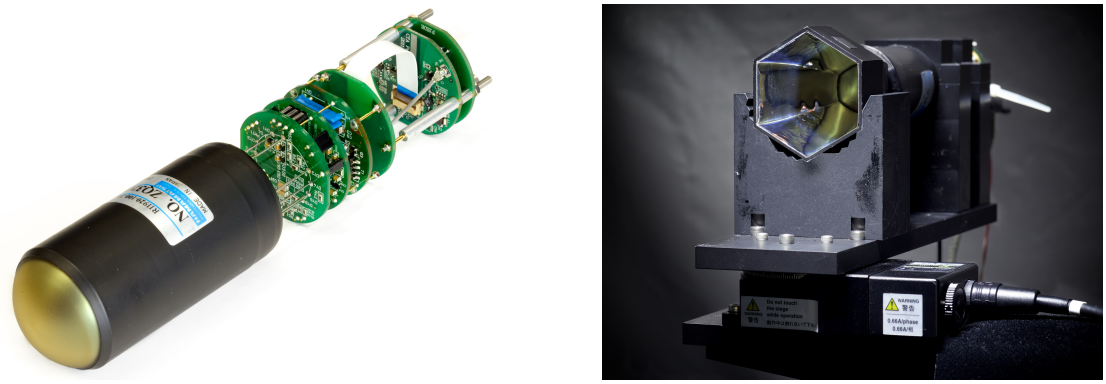

Figure 2.1: Photos of PMTs as used in LST-1 [96]. Left side: PMT with high-voltage circuit and preamplifier. Right side: PMT on a testbench with light-guide attached.

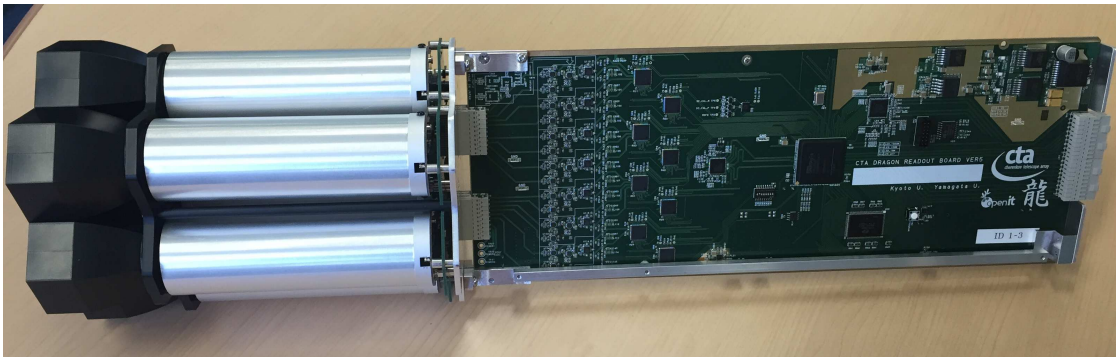

Figure 2.2: Photo of a camera module consisting of seven PMTs with light guides attached, slow control and readout board including the DRS4 chips [73].

and is also used in the MAGIC telescopes since the camera upgrade [100] in 2011.

A deeper sampling of a single channel can be obtained by connecting the same signal to multiple channels of the DRS4 chip effectively using multiple bits of the register for a single signal. On the LST-1 readout board, every pixel gain is sampled fourfold, leading to a sample depth of 4096, which results in $\approx 4\,\mu s$ at 1 GHz sampling rate. This sampling is obtained by connecting the low or high gain of two pixels to one DRS4 chip. Because mixing of the low and high gain channels would lead to cross-talk of the channels, two channels of different pixels, but the same gain, are connected to one chip. For this reason, the board contains eight DRS4 chips instead of seven, as two chips are only connected to a single channel each.

Mode 2:

Mode 3:

Mode 4:

The third generated pixel channel, the trigger signal, does not enter a DRS4 chip. Instead, it is fed towards a separate trigger circuit, level 0 trigger (L0), on the readout board. This trigger circuit sums the seven individual waveforms and sends the result to the neighboring pixel modules. In each module, different sums of these signals (according to different combinations of modules) are then accorded in the level 1 trigger (L1) system and the result is compared to a threshold [101]. Only if the trigger threshold is exceeded in any of the module combinations, the digitization of the voltages stored in the DRS4 capacitor arrays is started in a separate ADC.

The L1 trigger as well as the communication with several other subsystems is handled by the Trigger Interface Board (TIB) [102]. This allows for more trigger types than just "event-like", such as semi-random recording of background noise (pedestal events) and the calibration laser (flatfield events) at 100 Hz each. In monoscopic operation, LST-1 triggers at an event rate of up to 15 GHz [103]. In future stereo operations, once multiple telescopes are built, an additional coincidence requirement will be employed on the event trigger.

In addition to the readout board and pixels, each module contains a slow control board (SCB) that monitors the anode current, temperature, and humidity of the PMTs as well as controlling their high voltage supply [104]. On top of that, it allows the creation of test pulses for calibration purposes.

Once a waveform has been read out at R0 level, different calibration steps have to be performed on the individual waveforms before they can be used in the image extraction step.

The effects of the most important steps on a waveform recorded in a pixel containing Cherenkov signal from a rather bright shower (with the gain selection already applied) are

illustrated in Figure 2.3.

From the raw signal, a pedestal baseline is subtracted, which equates to the amount of background light not related to Cherenkov emission from the shower. This baseline has to be estimated from pedestal events as it is sensitive to the levels of Night-Sky Background (NSB) during the observation. After that, the first three and the last sample are removed from the waveforms, because they contain more noise as a consequence of the calibration procedure [105].

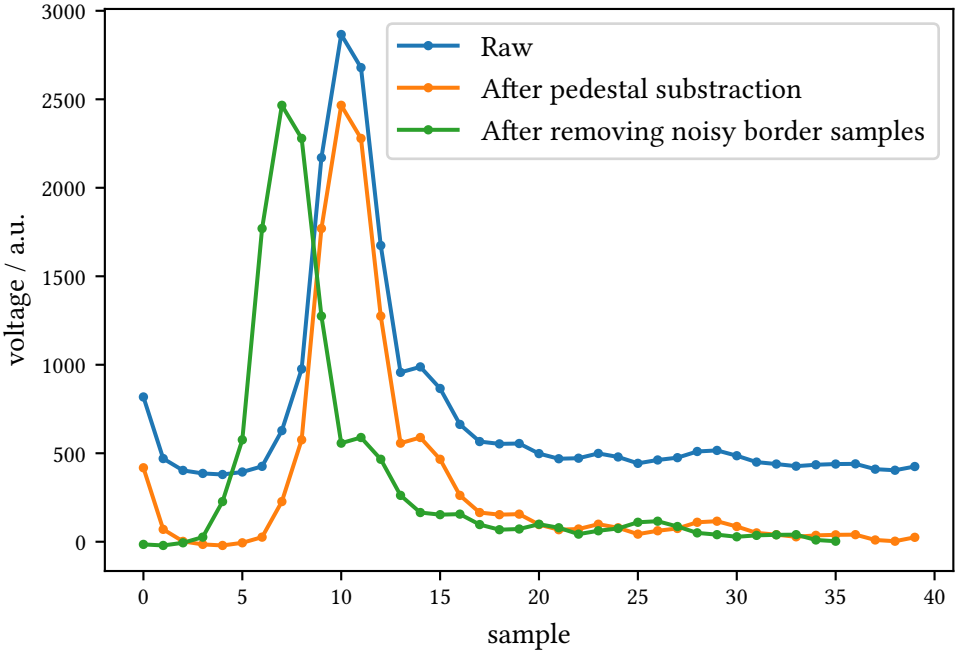

Figure 2.3: Recorded waveform of a real LST-1 event containing Cherenkov signal. Subtracting the pedestal noise moves the curve downwards towards a baseline of zero. Correcting for the offset of this pixel with respect to the rest of the camera moves the pulse toward the left (earlier times).

As a last step, the waveforms, which still have units of a voltage for the y-axis and no unit for the time, are converted to units of photon count equivalents (p.e.). The datalevel R1 consists of these calibrated waveforms.

The transition towards DL0 is a mere data reduction in which pixels likely to contain no signal from Cherenkov photons are removed, which reduces the amount of space the compressed data takes on the disks. The current plans involve performing pulse extraction and image cleaning, which are described in the following, with some preliminary settings that keep more data than what is used afterward in the step towards DL1. This is both a requirement for operation in the full CTAO array as well as a necessity for LST-1 to avoid running out of disk space.

Pulse extraction is the step from a waveform to two values per pixel: Integral charge and peak arrival time. These operations are still performed on a per-pixel basis[1]: For each pixel, an

[1]There are extractor methods that use multiple pixels to find the integration windows, but the one described

integration window is defined relative to the peak index (the index of the value containing the highest count of photoelectrons). From there, four values before and four values after the peak are included in the integration. The integrated charge is then just the sum of all charge values, and the peak time is the charge-weighted average of the sample times, which is then corrected using per-pixel calibration offsets. Figure 2.4 illustrates the main steps on the same waveform as shown in Figure 2.3 (after the conversion to p.e. has been performed).

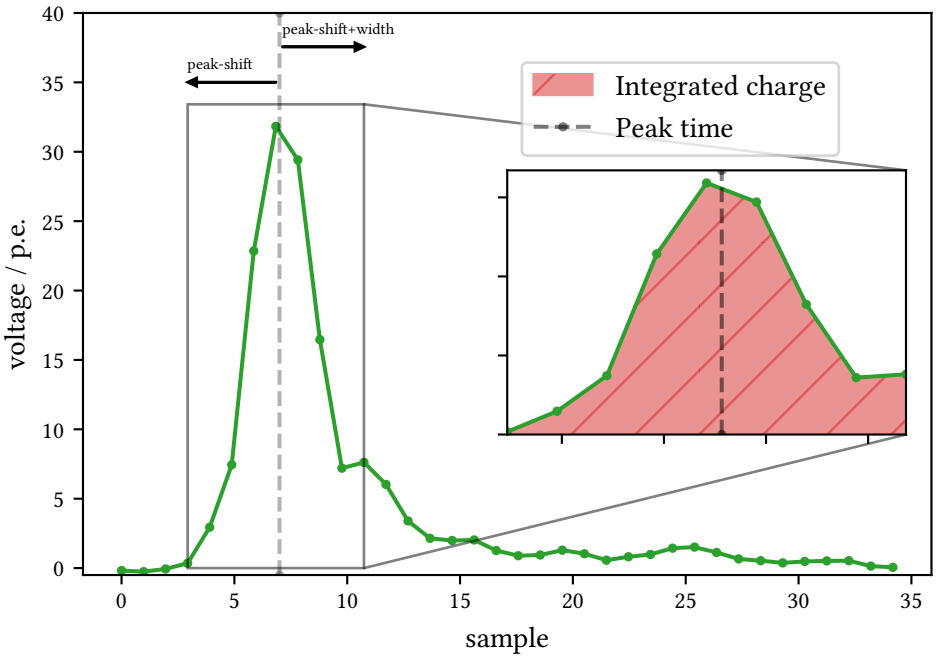

Figure 2.4: Process of image extraction on the example waveform. After finding the position with the highest charge, the start and end positions of the integration window are defined via the configurable parameters shift and width. Inlay: The charge inside the window is integrated, and the arrival time is calculated as a weighted average.

After the image extraction, an event contains two (charge, arrival time) times 1855 (number of pixels in the camera) values, which are referred to as camera images[2]. For the example event reconstructed here, the image of the integrated charges is displayed in Figure 2.5. The elliptical blob in the upper half of the image contains the Cherenkov signal from which the properties of the primary particle can be reconstructed.

(and used) here does not.

[2]Without further context, image often refers to just the image of the charges. The image of the arrival times is then highlighted separately.

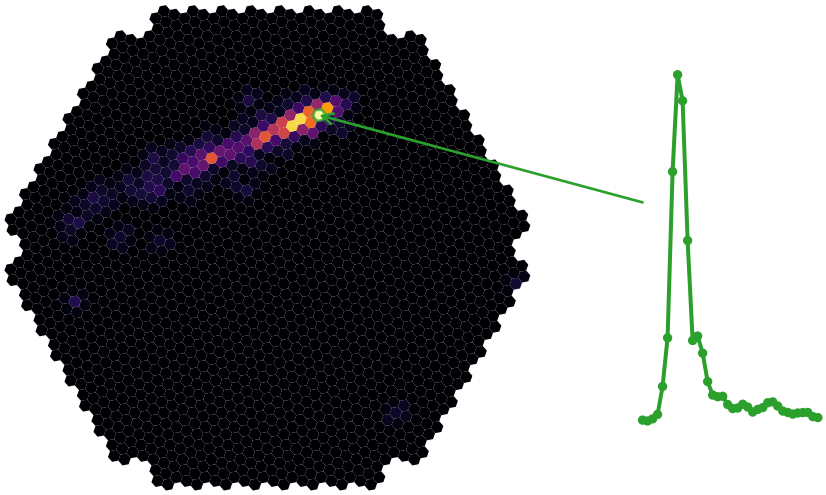

Figure 2.5: Example event after the image extraction step. Shown is only the image of the Cherenkov charges. The drawn waveform is the calibrated, p.e. converted waveform shown in Figure 2.4.

2.3 Image Cleaning

In order to make the reconstruction easier and less susceptible to the noise in the pixels without Cherenkov signal, the images are cleaned in the step towards DL1. Different cleaning methods have been developed at the predecessor experiments, but they all have the goal of selecting a subset of pixels likely to contain Cherenkov signal by comparing the image contents with some threshold values.

There is a clear tradeoff here, where harder cleaning settings (high threshold, discarding a lot of pixels) lead to less contamination and, therefore, easier to reconstruct images in the case of bright showers, but also end up with less signal overall, which limits the ability to detect very faint showers[3].

The cleaning step implemented in `lstchain` makes use of the tailcuts cleaning and time-delta cleaning algorithms implemented in `ctapipe`.

The standard tailcuts cleaning is an algorithm with three configurable parameters that works exclusively on the image of the integrated charges. In the first pass, pixels above an upper threshold are selected, and selected pixels with less than a configurable amount of neighbouring pixels are removed again from the selection. In the second pass, pixels above the second, lower threshold are selected if they have a neighbor, which was selected in the first step. This way, the fact that the shower image is brightest in the center and then gradually gets dimmer further away from the center is taken into account without selecting all pixels above the lower threshold, which would lead to more noisy images.

[3] Atmospheric conditions, pointing direction, etc. taken as constant. This means the lower energy threshold moves up as image intensity is correlated to the energy of the primary particle.

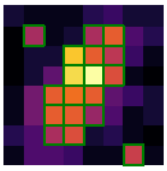

In the next step, the time-delta cleaning is evaluated on the previously selected pixels. It keeps pixels only if they have at least one neighbor that arrived in a timeframe of 2 ns, removing background pixels from the selection because of their random peak times. An additional dynamic cleaning discards pixels that contain less than a configurable fraction of the three brightest pixels if the brightest pixels contain a lot of charge.

The selected pixels for the example event are shown in Figure 2.6 on top of both event images.

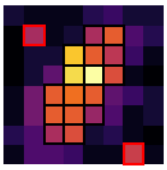

The standard analysis of Cherenkov telescope data involves an additional step before reconstructing the properties of the primary particle. In this step, parameters are calculated to describe the images. These image parameters are also part of DL1. More specifically, they form DL1B, while the cleaned images are referred to as DL1A. Some algorithms, such as deep neural networks, can work directly on the reconstructed images [106, 107], but the currently researched solutions are not part of the standard analysis pipeline.

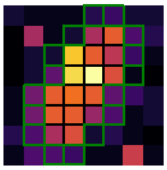

Most parameters are calculated with respect to the image of charges: a principal component analysis of the counts and positions yields two components, of which the direction of the first one is identified as the main shower axis. This direction is assumed to be the direction of the shower development. The absolute values of the eigenvalues are referred to as the length and width of the shower image. Together with the sum and the intensity-weighted average of the pixel positions, these are usually called the Hillas parameters because their use was initially proposed by A. M. Hillas [108]. Besides the first and second moments length and width, the third and fourth moments of the distribution are calculated as well (skewness and kurtosis).

A set of leakage parameters measures how much of the recorded intensity is located in the outermost parts of the camera. This gives an estimate of how much light from the shower arrived outside the F.o.V. and, subsequently, how complete the image is.

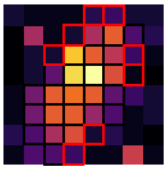

On the image of the peak times, similar parameters can be calculated: To first order, the arrival times should follow the main shower axis because the position of the emission along the shower axis (in 3D space) defines the distance to the start position of the shower and the camera and thus the time a Cherenkov photon is emitted and arrives at the telescope[4]. The measured arrival times are projected on the reconstructed main shower axis and a linear regression is performed.

An illustration of the parameter calculation is given in Figure 2.7 using just the pixels that survived the previous cleaning step.

[4]With the small subtlety, that the photons that were emitted first arrive last, because the electrons move faster than the light in the atmosphere.

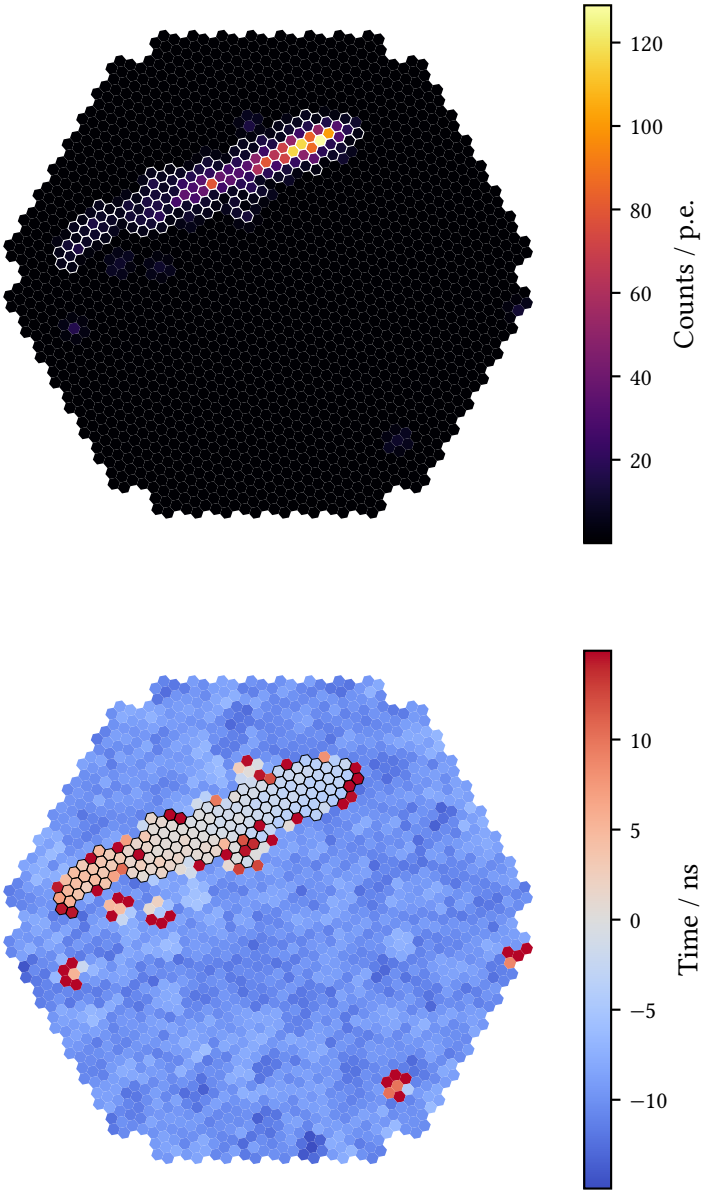

Figure 2.6: DL1 event images with cleaning mask. The highlighted pixels are the ones chosen as signal pixels for the subsequent analysis.
Top: The image of the integrated charges. Yellow values equate to higher photon counts, and violet values equal lower counts. Pixels in the shower blob are much brighter than the camera average.
Bottom: The image of arrival times. Bluer values refer to earlier times, and red to later ones. Pixels in the shower blob are correlated in time, while background pixels are distributed randomly.

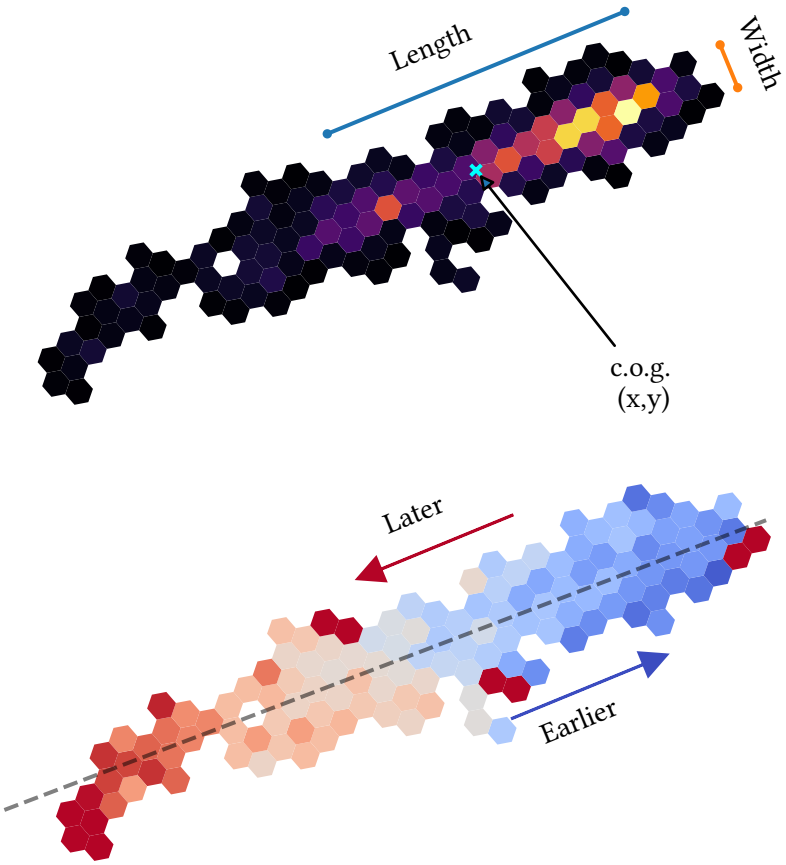

Figure 2.7: Illustration of a subset of image parameters on just the cleaned images. The dashed line is the reconstructed shower axis and follows the assumed shower development. Top: Parameters obtained from the PCA of the charges. Bottom: Relative peak times. The gradient is along the main shower axis.

2.4 Data Selection

As of `2024-01-30`, LST-1 has observed `173` individual targets[5] with a total observation time of 1997.95 h. A grand total of `112` observation runs or 28.47 h were dedicated towards observations of the source M87.

All of the observations have been performed using the wobble-method: Instead of pointing the telescope directly at the source, a slightly offset position is targeted and this position is alternated between observations. This makes it possible to define off-positions in the F.o.V., where the telescope acceptance is similar to the one in the source region. Even if there are systematic differences, they would cancel out when combining observations from multiple wobble-positions as long as the exposure at each position is equal. For the observations

[5]The term target is chosen here over source, because the stated number also includes off-observations (mainly for the Crab Nebula) and observations of source candidates, Gamma-Ray Bursts, etc., that did not lead to a detection.

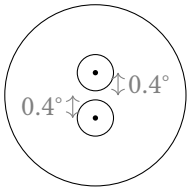

considered here, a wobble-distance of 0.4° is used.

The data is analysed on the observation site using the `LST-OSA` package up to DL1, which manages the automatic creation of analysis steps using the Slurm Workload Manager [109]. Most analyses start from the DL1 files produced by the onsite analysis. These onsite analyses are redone on all available observations whenever there are substantial changes to the underlying `lstchain` software. This means, that the aggregated runlists can contain files processed with different versions, if the changes were found to not affect the low-level performance and do not break the file format.

However, not all of the recorded data can be used for the analysis. Instead, the data quality of all observations needs to be assessed, and data with poor quality should be removed from the sample. This is the case for all experimentally obtained data, but even more relevant for LST-1, because

1. IACTs operate under changing conditions without control over the weather and atmosphere.
2. The early stage of LST-1 implies some issues in data-taking.
3. There are no simulations tailored to non-optimal observation conditions yet.

In particular, due to the last point, only close-to-optimal conditions are accurately described by the simulations.

Selecting good-quality data for further analysis should be done at as low a level as possible to avoid analyzer biases in the high-level data products. For this reason, the onsite analysis performs checks on all of the observed data as part of the next-day analysis. In this step, different metrics are calculated from the low-level data in addition to direct monitoring data, such as the pointing position and accuracy. Whilst the absolute values of some metrics, such as the rate of triggered events, can differ depending on the observation target and changes in the trigger thresholds, variations among observations of the same target can indicate issues in data-taking or the observation conditions.

Additionally, the shifters write up shift summaries for every night, noting when issues arise during data-taking. This way runs that have known issues can be marked. Not every issue in data-taking renders the quality of the observed data useless: Sometimes only short periods are affected, or the issues are not directly related to the data taken. Nevertheless, some runs have major issues noted and behave irregularly in the analysis. They are listed here first and are not taken into account when defining the range of acceptable parameter values:

```
[3744, 4507, 4508, 4509, 7185, 7186, 7187, 7188, 7189]
```

The first aspect of the changeable observation conditions regards the level of the NSB: On the one hand, the position of the F.o.V. changes the baseline expectation for the amount of light entering the camera as different regions in the sky contain more or fewer stars, secondary sources, and diffuse background light (be it truly diffuse or unresolved point sources).

For example, a high NSB is expected for the observation of the galactic center, whereas extragalactic sources oftentimes have lower levels of NSB depending on their distance from the

galactic disk. After selecting a source/region of interest, this effect should be constant for all observations, so the absolute value does not affect the selection of good runs. Instead, the more important effect lies in making sure the simulations match the observed NSB. In the case of M87, the F.o.V. is dark, as there are no known gamma-ray sources nearby, and the galactic disc is far. For this reason, no additional fine-tuning of the simulations is needed. This is in contrast to, for example, observations of the Crab Nebula, where additional noise is added on the DL1 images [79].

On the other hand, there is some variation of the NSB between runs. Besides atmospheric variations, the main effect comes from the illumination of the moon. IACTs generally do not perform normal observations close to a full moon, but in the case of a partially lit moon, observations are carried out, and the analyzers need to make sure the contamination due to the moon is not too bad. At the present time, these observations will often times cause issues in the analysis because they would need special analyses (see for example [110]) and thus have to be removed.

Estimating NSB levels is done by comparing the standard deviation of pixel charges. This follows directly from the Poissonian statistics of the measured counts, where the variance of the distribution is equal to the expected value.

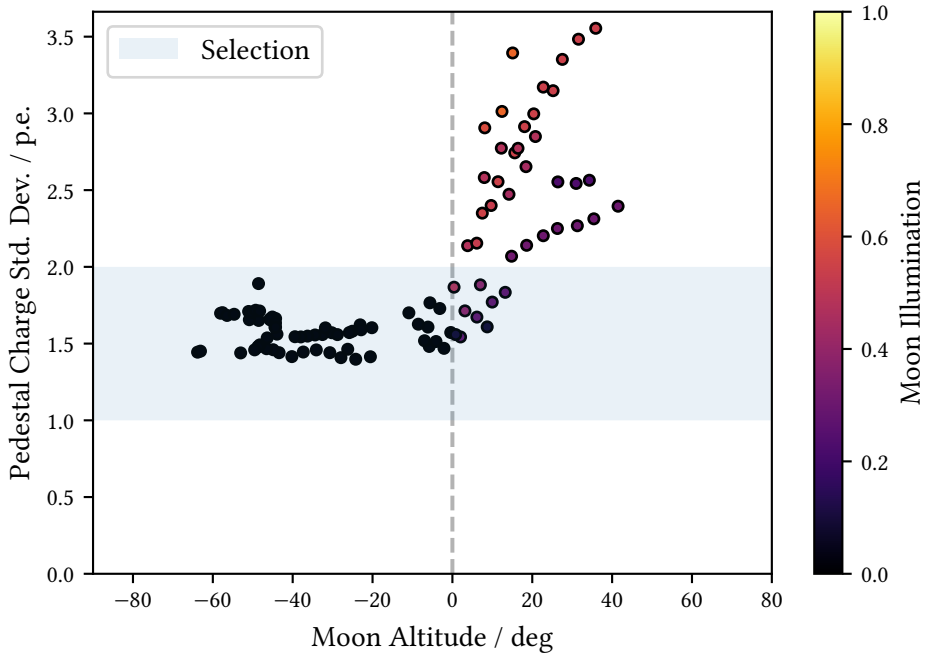

Figure 2.8: Standard deviation of charges in interleaved pedestal events with color-coded moon illumination at the time of observation. Moon illumination is set to zero if the moon is below the horizon (left side). A clear correlation is evident for the observations where the moon was above the horizon at the observatory (right half).

As can be seen in Figure 2.8, there are some runs, which were taken under moon conditions, and the fraction of illumination is correlated directly with the charge deviations of the pedestal events. As long as the moon is below the horizon, the values are stable with only minor

deviations. The selection is thus chosen with limits that do not remove any data without the influence of the moon.

Next, the effect of the atmospheric transmissivity is taken into account: unfortunately, LST-1 does not deploy any direct measurements of the atmosphere. MAGIC does, using a Lidar, but it was notoriously malfunctioning for larger periods of the observation period, leaving most runs without direct measurements of the atmospheric transmission.

The rate of triggered events can be seen as a proxy for the transmission of the atmosphere though: if the transmission is low due to humidity or clouds in the F.o.V., the atmosphere will absorb more of the Cherenkov light and less light reaches the telescope. In turn, the rate of triggered events should be roughly constant if the observation conditions are clear and the telescope is pointing at the same position. For the data sample used in this analysis, this is indicated in Figure 2.9.

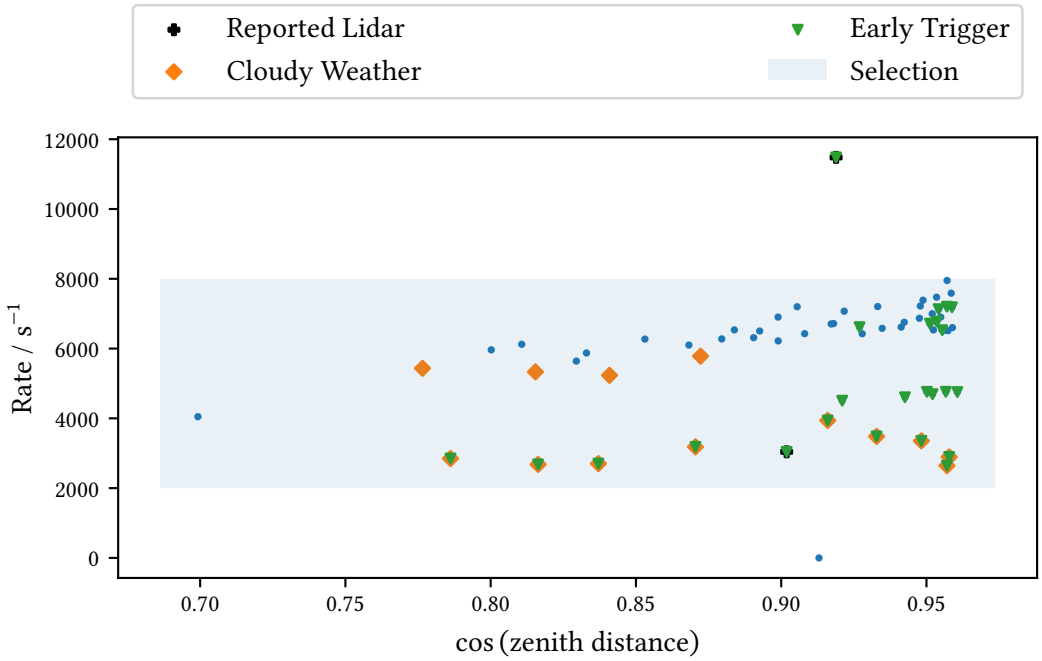

Figure 2.9: Rate of triggered cosmic events for all observations surviving the NSB selection. Highlighted are the minimum and maximum rates below/above which observations are discarded from the dataset. The observations with early trigger settings generally exhibit lower event rates.

First of all, it can be noted that the rate of triggered events is not constant over different zenith distances. Instead, the rate of triggered events is related to the airmass that the shower has to travel through. The light reaching the ground is attenuated by a factor of the inverse of the airmass, which itself is proportional to $1/\cos\theta$ to first order. This follows from the fact that for the propagation of the Cherenkov light, only the lower parts of the atmosphere matter because the primary particle already propagated through the upper parts and the Cherenkov light that reaches the ground in the near-optical spectrum. For zenith distances up to ≈ 60 to $70\,\mathrm{deg}$, a planar atmosphere can then be assumed, and the relation follows from simple geometry.

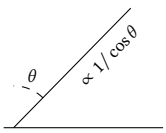

In practice, the relation is more complex, but the general trend of lower event rates at higher zenith distances remains (see e.g. [111]).

Second, there are two observations that can be classified as clear outliers. One run (8091) does not have any rate associated with it. It is known to have faulty datacheck information due to issues in data taking and should always be removed. Another one (4985) has a much higher rate than all other ones. This indicates that the reported Lidar events actually messed with the data taking.

Apart from that, there is a second population with systematically lower rates. These are the observations performed before the trigger thresholds became stable. Most of them also have clouds noted in the shift summaries. From this plot alone, it is not necessarily clear if they can be kept, as the possible influence from poor weather conditions can not be easily disentangled from the effect of trigger settings. If they are to be used, a large enough intensity filter has to be applied to avoid mismatches to the simulations in low-intensity events [79].

Before deciding how to handle these runs, an additional selection is performed on the rate of events that contain at least 10 or 30 p.e.. These rates are much lower and more directly related to the rate of events that survive the image extraction and cleaning instead of all triggered events. They are shown in Figure 2.10. There is a clearer picture here, with outliers above and below the expected rates.

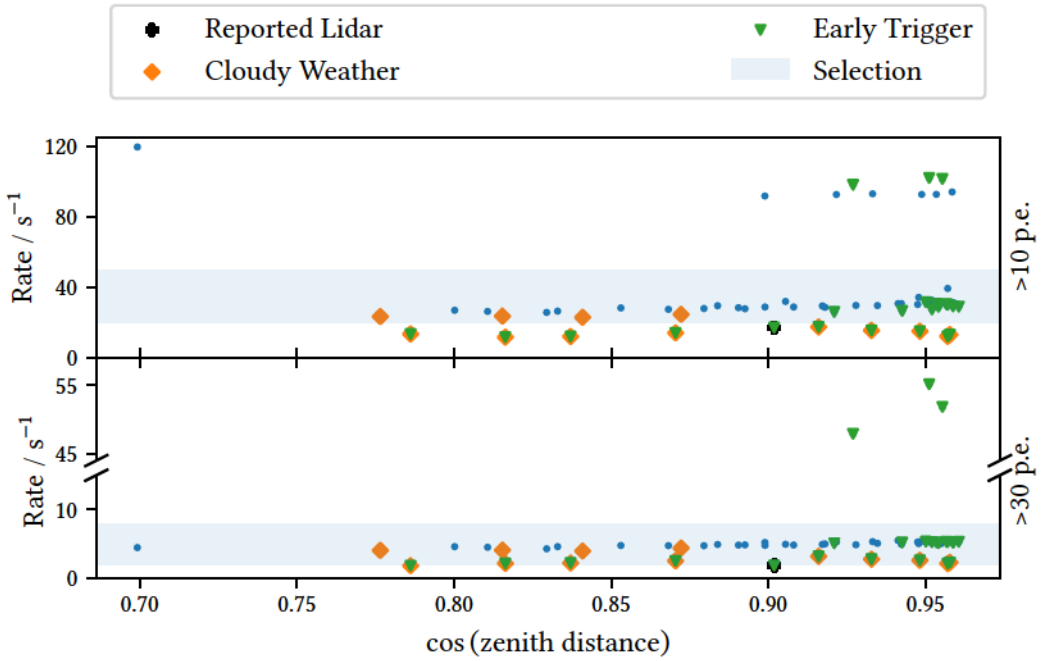

Figure 2.10: Rate of triggered events with more than 10 (left) and 30 p.e.. Some runs show rates far above or below the expectance. They are removed from further processing. Both plots show the same points. For this reason, an observation can fall into the selection window of one criterium but not the other (for example, the leftmost observation 7773).

First of all, some observations show event rates of events above 10 p.e. far above the

expectation. Those that have been taken with older trigger settings are also outliers above 30 p.e., the ones with final trigger thresholds are not. To make sure that this effect is not related to different periods of source activity, the same rates are also plotted against their run number in Figure 2.11.

It can be noted that there are other observations close to the affected ones that do not show this behavior, which leads to the conclusion that these observations do, in fact, show unwanted features. Some of them have minor issues reported, but most do not. Since their rates differ so much from all the other runs, they are removed.

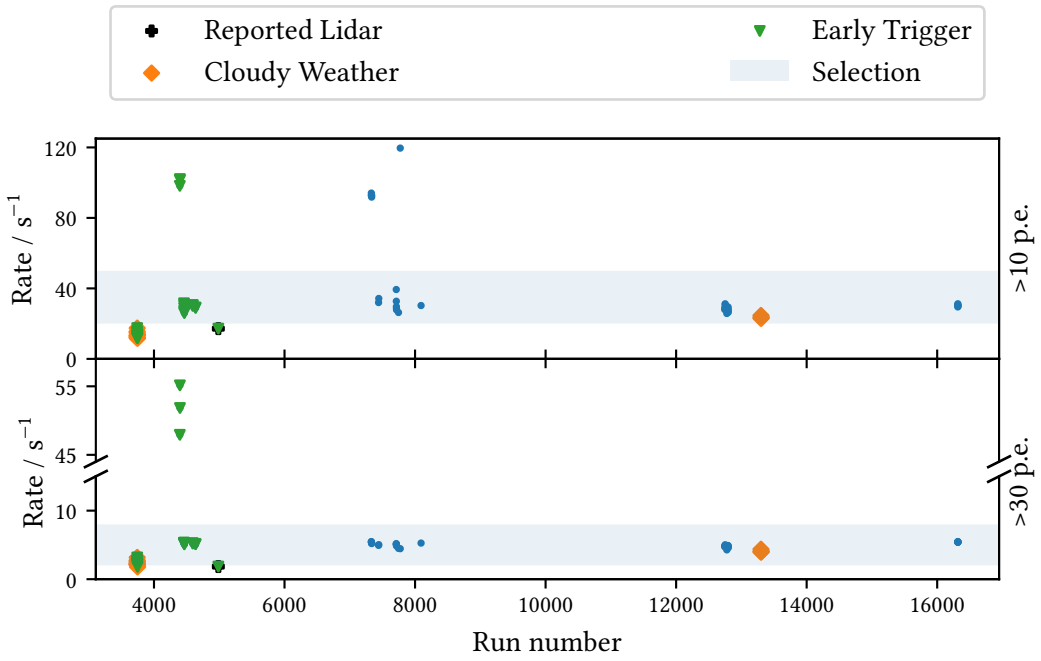

Figure 2.11: Rate of triggered events with more than 10 (top) and 30 p.e. (bottom) against run number. Same data as in Figure 2.10.

Looking at the observations with lower-than-expected rates, it is striking that they almost exclusively consist of a single night of very early observations. All observations in this early block also have poor weather conditions noted. Since the other observations that are performed with non-final trigger settings do not show a clear bias in these rates, the clouds the shifters have observed, apparently did affect the data-taking and including them in the analysis would most certainly lead to issues. The only additional outlier has issues with the Lidar reported, so it will also be removed.

After the selection, 11.12 h of data remain. The final list of observations that are used for further analysis is given in Table 2.1.

Table 2.1: Observations remaining after all data-selection steps.

Observation ID	Elapsed time / min	Start of Observation
4460	10.7	2021-04-17 23:17:52.000
4461	15.1	2021-04-17 23:32:19.000
4462	17.1	2021-04-17 23:51:10.000
4463	18.1	2021-04-18 00:12:10.000
4464	18.1	2021-04-18 00:34:32.000
4465	15.1	2021-04-18 00:56:30.000
4594	14.1	2021-05-04 22:56:30.000
4595	15.1	2021-05-04 23:12:51.000
4636	11.4	2021-05-07 22:33:31.000
4637	20.0	2021-05-07 22:50:38.000
7441	20.1	2022-03-24 00:07:45.000
7444	20.1	2022-03-24 00:49:01.000
7712	19.5	2022-04-08 00:40:39.000
7713	18.8	2022-04-08 01:01:26.000
7714	17.4	2022-04-08 01:21:23.000
7715	17.6	2022-04-08 01:41:53.000
7716	12.7	2022-04-08 02:00:45.000
7746	5.9	2022-04-09 02:48:43.000
8092	18.4	2022-05-03 22:11:31.000
12745	17.8	2023-04-18 22:09:40.000
12746	15.1	2023-04-18 22:27:56.000
12751	19.4	2023-04-19 00:09:20.000
12752	20.0	2023-04-19 00:29:08.000
12753	20.0	2023-04-19 00:49:38.000
12754	20.8	2023-04-19 01:10:08.000
12775	14.8	2023-04-20 01:22:46.000
12776	14.5	2023-04-20 01:38:05.000
12777	14.6	2023-04-20 01:53:06.000
12778	8.8	2023-04-20 02:08:05.000
12796	16.8	2023-04-21 00:52:57.000
12797	16.5	2023-04-21 01:10:17.000
12798	16.6	2023-04-21 01:27:17.000
12799	16.5	2023-04-21 01:44:21.000
13300	13.2	2023-06-14 21:50:45.000
13301	15.0	2023-06-14 22:04:22.000
13302	14.9	2023-06-14 22:19:47.000
13303	15.6	2023-06-14 22:35:10.000
16315	14.8	2024-01-11 05:30:36.787
16316	14.7	2024-01-11 05:45:47.369
16317	14.6	2024-01-11 06:00:52.148
16318	14.7	2024-01-11 06:15:48.122
16319	12.2	2024-01-11 06:30:49.262

2.5 Reconstructing the Primary Particles

Simulations

At DL1, the data still describes the Cherenkov light measured in the camera. As the next step of the analysis pipeline, conclusions are drawn about the primary particle that initiated the particle shower. A file at datalevel 2 (DL2) then contains a list of the events as the DL1B file previously did, but instead of the image parameters, the reconstructed properties of the primary particle are listed. In the present form, `lstchain` files at DL2 include not only these properties, but also the parameters and auxiliary information from DL1B.

The primary particle is properly described if five quantities are specified:

- particle type (gamma ray or hadronic background),
- energy E,
- position p, where the primary originated from (two angles on a sphere),
- time of arrival t.

The arrival time is measured directly as part of the trigger, all other properties need to be reconstructed from the measured Cherenkov light.

To perform this reconstruction, machine learning models are needed to reconstruct the primary particle's properties. Before they can be used to reconstruct observed showers, the models need to be trained, which requires the existence of a dataset that includes the true properties of each event. Since there is no way to get the true properties of actual observed showers, simulations are performed to describe the physical processes as accurately as possible.

In addition, the step from DL2 to DL3 includes estimating the absolute performance of the telescope, including the error made in the reconstruction, which again requires a truth to compare the reconstructed values against.

These simulations are performed using a combination of CORSIKA [112] and sim-telarray [70]. This way, the simulation is separated into the creation and propagation of a shower from a primary particle hitting the atmosphere including the creation of Cherenkov light and the measurement process of the telescope.

While originally developed for KASCADE, CORSIKA is nowadays widely used among different collaborations in the field of astroparticle physics. Starting from primary particles with directions uniformly drawn from a predefined region of the sky and energies drawn from a power-law distribution, the interactions of all shower particles in a set atmosphere model are simulated. This includes both continuous energy losses and stochastic interactions, where new particles can be produced that are then added to the stack of particles to propagate. Eventually, particles fall below an energy threshold and are removed. In addition to the high-energy particles of the shower, the emitted Cherenkov light can be simulated and propagated to the ground, which is the main output for IACTs.

Using the IACT/ATMO package [70], CORSIKA assumes a simplified version of the telescope-array, where telescopes are approximated as three-dimensional spheres to determine which Cherenkov photons might hit the detector and should thus be written to disk.

While this approximation is simple, it limits the output that needs to be processed at the next step and is more efficient than using a horizontally flat detector.

In the next step, the photons that hit the telescope are propagated through the telescope optics and electronics using the software sim-telarray. A ray-tracing simulation follows the path of the Cherenkov photons to the PMTs, simulating the optical properties of the mirror tiles as well as any background light, a trigger response, and the readout of the electronics.

The final output closely resembles observed raw data with the addition of simulation-specific information, such as the simulation settings and the primary particle's true properties, from which the performance of the reconstruction can be estimated. From there on, simulations are processed mostly in the same way as observed data: The pipeline integrates the raw waveforms and performs any pre-selection steps to end up with cleaned, parametrized images of showers (DL1). In contrast to observed data, the information about the primary particle producing the shower, that lead to the image in the camera, exists as well. On the computing clusters, this work is orchestrated using the software `lstmcpipe` [113].

Since mismatches between the data and the simulations are known to exist (especially for the observations before August 2021), events with low recorded intensity (<80 p.e.) are removed from both data and simulations (see [79] for details).

In addition, a cut on the leakage parameter is performed to remove events with a high percentage of the reconstructed charge in the outermost parts of the camera. The missing information can not be properly reconstructed in the standard analysis leading to unreliable reconstructions.

While they are vital to the operation of the telescope, simulations are expensive to perform in terms of computing resources and time, which is why there is usually a limited set of simulations, that is used until changes in the experiment characteristics necessitate new simulations instead of performing new simulations for each observation. One reason for a difference in performance between the physical telescope and the simulated one is the deterioration of the mirrors over time, another one is the replacements and upgrades that take place over time.

MAGIC uses the term Monte Carlo period to describe when simulations are accurately describing the experiment. LST-1 does not have such a concept and instead uses the same set of simulations for all observations.

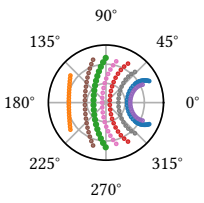

Simulations are performed with different pointing positions of the telescope, as the observed event rates and images differ with zenith distance and azimuth. This is referred to as the grid of simulations. The way this grid is constructed in LST-1 is somewhat convoluted as there are two separate grids: A training grid for training the models and a test grid for estimating the performance for the case of a pointlike analysis.

While the training grid is composed of points on the paths that some predefined sources follow over the sky, the test grid is coarsely distributed over the sky in a way to best cover the parameter space, and only samples gamma rays from positions in a ring around the telescope pointing that matches the wobble offset. For some analysis cases, it is enough to follow this predefined split, but if the analysis includes the creation of spatial excess maps, simulated gamma rays from all positions in the F.o.V. are needed.

The training grid consists of simulations of primary gamma rays and primary protons. Fortunately, the simulations contain more simulated gamma rays than would be needed for the training of the models, which allows for a split of the former training dataset into a new, slightly reduced training dataset and a new test dataset.

Model Training

In the training step, each model's parameters are varied in order to get the best estimate of the target variable on the training set: given the two-dimensional matrix of image features X, where the dimensions are the input features and the number of events, the model parameters are varied in a way that some quality-of-fit metric comparing the true value of the dependent variable y and the reconstructed values $\hat{y}$ is minimal. The input features consist of some of the DL1B parameters and the telescope's pointing position because there is only one model of each kind for all the pointing positions in the grid.

This metric is named the loss-function hereafter and differs between regression tasks, where a continuous variable is predicted, and classification tasks, where the dependent variable can only adopt discrete values.

In theory, it is possible to train a single model to reconstruct all dependent variables at once, but in practice, the pipeline trains multiple models: One model to differentiate between signal (incoming gamma ray) and background (other particles), one to estimate the energy of the primary gamma ray, and two models for the reconstruction of the shower direction.

Splitting the task into multiple models has some advantages: It is easier to implement correctly in software, not all parameters are relevant for each of the tasks, and it allows using the reconstruction of one model as additional input for the other model(s). In particular, the information about the reconstructed energy improves the reconstruction of the classification model.

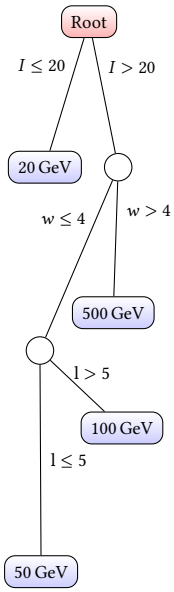

Different model architectures can be used for these tasks; the current `lstchain` implementation makes use of a total of four Random Forests implemented in `scikit-learn`[86].

A Random Forest is composed of an ensemble of individual binary decision trees, which are models consisting of a root node that recursively perform binary splits of the training data in order to obtain the best separability minimizing the loss-function.

On each node, a single split on one feature is performed that separates the dataset into subsets. The partitioning continues until there are not enough samples remaining at a node or a maximum depth has been reached. At that point, the node becomes a terminal node, and the corresponding prediction the mean of the target feature (regression) or the proportion of the signal class (classification) of selected training events. The prediction of an event is then obtained by following the splits until a terminal node is reached, starting from the root of the tree. In practice, learning an optimal decision tree is an NP-hard problem [114], which is why greedy algorithms are used to find locally optimal splits.

From their construction, some of the disadvantages of decision-tree models can be anticipated: The chosen splits are very specific to the training dataset, which might lead to overfitting and generally means that the constructed trees are unstable with respect to variations in the training data. Furthermore, predictions are not smooth but instead piecewise constants, which can be a problem for continuous variables such as the particle energy.

Still, decision trees are a popular class of statistical models because they are fast to construct (both in terms of computing resources and data preparation) and their output is easily explainable. For this reason, models based on decision trees that try to overcome their shortcomings are used widely. One class of such models is the aforementioned Random Forest [115]. In a Random Forest, multiple decision trees that each get a random subset of events to fit on are trained

separately. In addition, the individual trees are further randomized by only having access to a random subset of features. This way, a forest of different trees is constructed. The ensemble prediction is then the mean of the individual trees, which avoids both the overfitting and the discrete nature of the predictions.

Training the models is a single script in `lstchain`, where all models are built sequentially. For the energy, a RandomForestRegressor is used (as the energy is a continuous variable), whereas the background rejection is done using the RandomForestClassifier class from `scikit-learn`. For the direction reconstruction, a combination of a regressor and classifier is needed. All models share similar feature sets and hyperparameters.

In particular, the depth is limited, and no further splits are performed if a node does not contain more than 10 events.

Energy Regressor

As the first step of the pipeline, the energy regressor is trained on a set of gamma-ray showers. The loss function for this model is the mean squared error (MSE):

$$\mathrm{MSE} = \frac{1}{n} \sum_{i}^{n} (y - \hat{y})^2 \tag{2.1}$$

Since the energy spans a large range of values, the highest energy events would dominate the loss function if the energy was predicted directly. Instead, the model is trained to predict the logarithm of the energy.

In general, energy estimation is rather simple conceptually because the propagation of gamma-ray showers in the atmosphere is well understood. Since the simulations do not alter the atmosphere properties and partially contained events are not part of the dataset, the collected light together with the pointing altitude and the features correlated to the distance of the impact position describe the problem well. The importance of the individual features, as estimated with `scikit-learn` is shown in Figure 2.12 with the feature importances of the individual trees marked as scatter points.

Direction Reconstruction

In the second step, the models for reconstruction of the arrival direction are trained. The used "disp" method is applied in different variations at all major gamma-ray telescopes and was originally developed for the Whipple telescope [77]. Disregarding any noise in the camera and assuming a sufficiently bright shower, the main shower axis of the image translates to the path of the primary particle in the sky, and some point on this axis corresponds to the origin of the primary particle (recall the general discussion around Figure 1.13). This simplifies the general two-dimensional regression of finding a point in the camera plane to a one-dimensional one (any point on the line). In practice, the main shower axis can be offset from the true axis due to the finite light yield and the limited resolution of the camera. The assumption still largely holds and is difficult to improve on without assuming a position of the source a priori, which is sometimes done under the label of a source-dependent analysis.

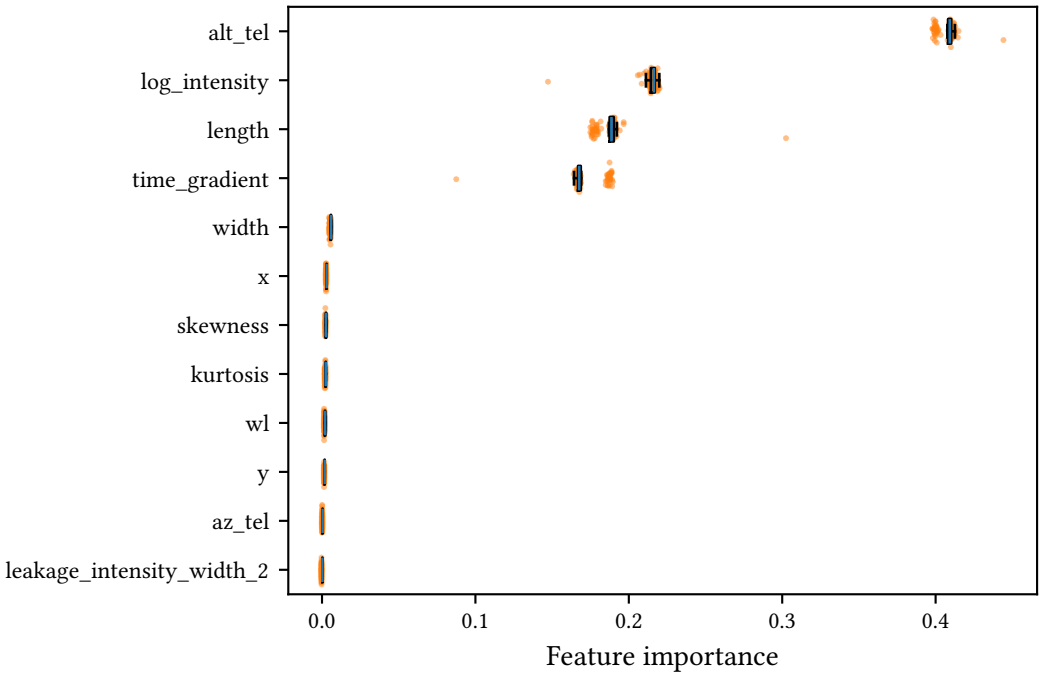

Figure 2.12: Feature importance for the energy regressor. Pointing altitude, captured light and the shower elongation (as a measure for the distance of the impact point) contain most of the information.

For monoscopic telescopes, there exists an additional limitation in that it is difficult to decide on which side of the image the origin position lies. While the third-order moments of the charge distribution and the direction of the linear fit of the arrival times allow for an almost perfect classification at high energies, images with low intensity or with small impact distances (low ellipticity) are difficult to reconstruct.

As the shower can be oriented in any direction in the camera, there is no statistical preference for one of the two sides and reconstructions with the correct absolute value, but the wrong direction heavily affects the loss function. For this reason, the task is split up into two independent models in `lstchain`. DISP, referring to the absolute value of the displacement, which then results in two possible source positions and SIGN, which is a binary value indicating which side of the shower to choose. See Figure 2.13 for an illustration of the head-tail ambiguity.

This is why, for the lowest energies, the angular resolution of a monoscopic telescope drops off rapidly as the share of events with wrong-reconstructed signs increases, and these events are then reconstructed far away from the actual source position in a circle around the actual source position. In a stereoscopic setup, the reconstruction of the sign can be avoided because the reconstructed shower axes of the individual telescopes (nearly if n>2) intersect, leaving just one possible direction.

This way, the regression task is simpler to learn using again the MSE as loss function. As can be seen from Figure 2.14, the most important features are the ones related to the ellipticity and time gradient in the image. This is expected from the close relation between the DISP

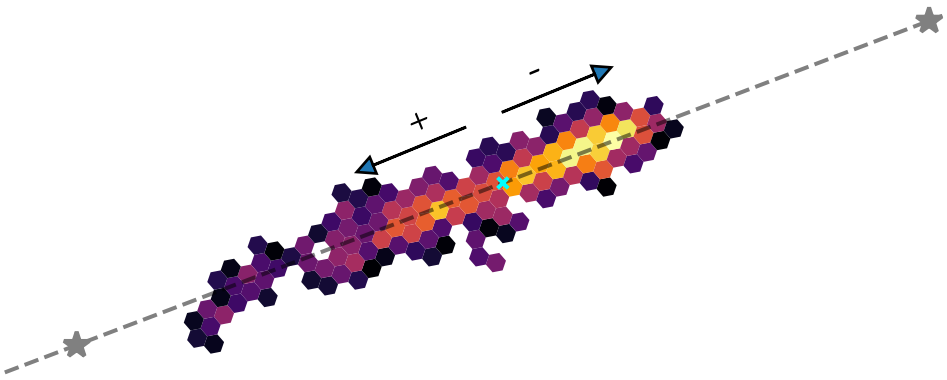

Figure 2.13: Illustration of the disp method to reconstruct the source position. Before the head/tail disambiguation, two points on the main shower axis at the same distance to the cog are candidates for the shower origin. The SIGN model predicts which side is the most likely to be the shower origin.

parameter and the distance to the impact point.

The reconstruction of the sign is a binary classification with two balanced classes (as the showers are randomly oriented in the camera). Training involves minimizing the gini impurity as given in Equation 2.2 which for a sample in node m involves calculating the proportion p_{mk} of events belonging to class k (either in the direction of the main shower axis or in the opposite direction).

$$\text{Gini impurity} = \sum_{k=\{+,-\}} \hat{p}_{mk}\left(1 - \hat{p}_{mk}\right) \tag{2.2}$$

The model is able to predict a score in the range $[0, 1]$, but as there is no preference for any side, only the binary value corresponding to a value above or below 0.5 is kept. Most of the predictive power lies in the time gradient and the third-order moments, which require a certain image brightness to calculate with confidence, see Figure 2.15.

Background Rejection

The gamma/hadron separation model additionally uses simulated showers originating from protons as the background to separate the gamma-ray showers from. These are simulated at the same grid nodes as the gamma-ray showers. Limiting to just gamma rays and protons is a simplification because, in reality, the background also contains electrons/positrons and

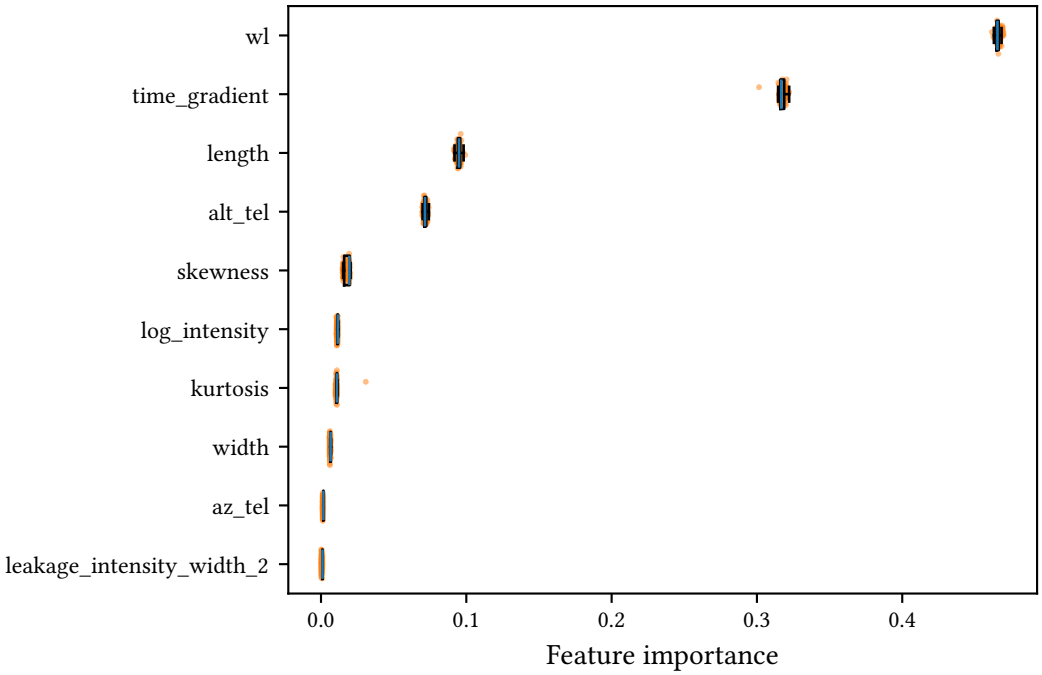

Figure 2.14: Feature importance for the DISP regressor. The ellipticity measures *wl* and the time gradient contain most of the information.

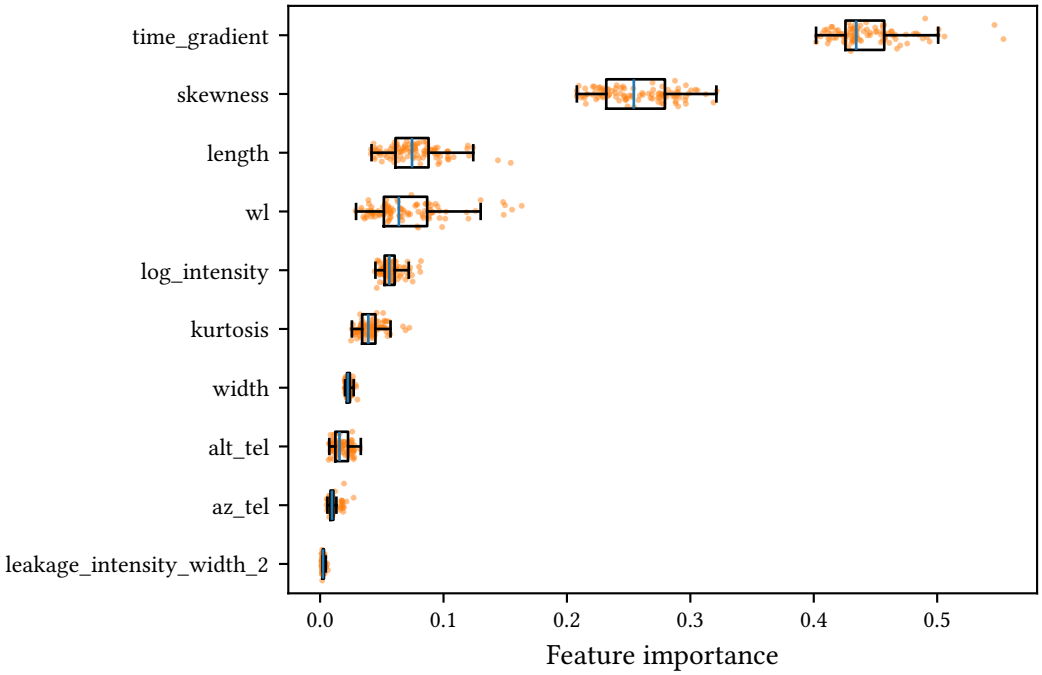

Figure 2.15: Feature importance for the SIGN classifier. Different features contribute to the decision, with the time gradient and the skewness of the charge distribution being the most important ones.

heavier nuclei, such as helium or iron. For the purpose of separating gamma rays this is largely sufficient because electrons are almost impossible to separate from gamma rays as the showers develop almost identically, whilst other nuclei differ from gamma rays and electrons in much the same way qualitatively: The presence of nuclear interactions in hadronic showers leads to a less regular image in the camera, often consisting of multiple islands that survive the image cleaning. Taking into account these other contributions is relevant, especially when constructing a background model from simulations or when analyzing the cosmic-ray spectrum itself, such as in [116]. For the training of the gamma/hadron separation model, the gini impurity is used again.

Different parameters contribute to the model decision, as evident by Figure 2.16. As the parameters are constructed assuming regular gamma-ray showers, they often do not describe the hadronic images well. Notably, there are additional features used for the classification, namely the output of the energy regressor and disp/sign models. The rationale is that hadronic and gamma-ray showers produce images of different intensities at the same primary particle energy because the produced particles are heavier and thus produce less Cherenkov light at the same energy of the primary particle. A parameter that might be expected to show up here is one that counts the number of non-connected islands in the cleaned image. It is not used in analyses of LST-1 anymore due to its sensitivity to misaligned mirrors that can produce ghost images in the camera.

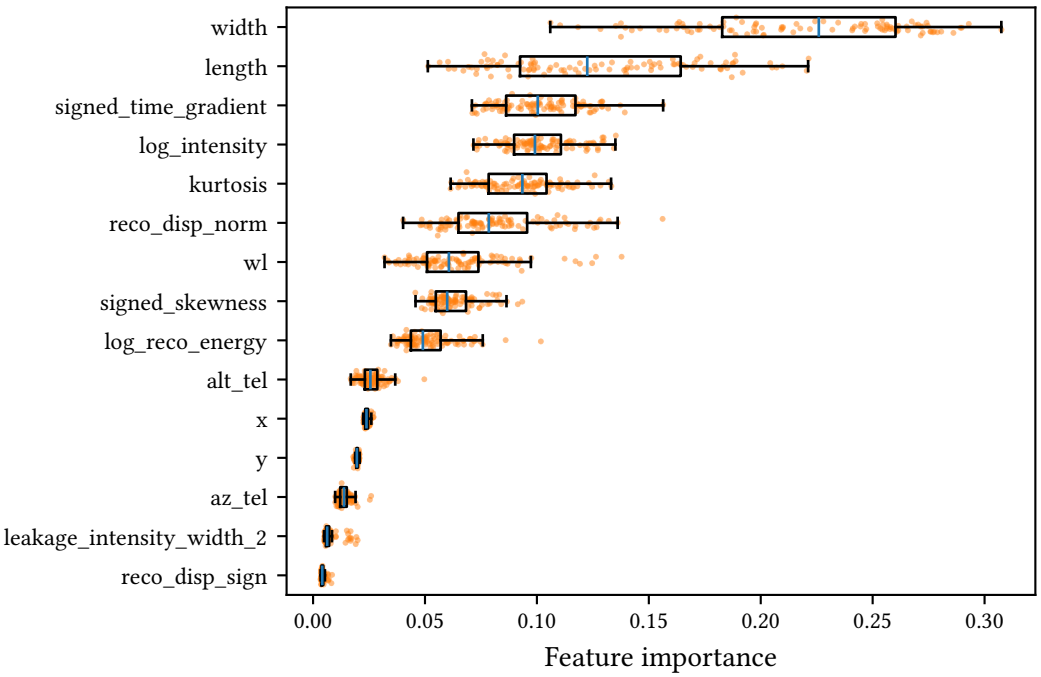

Figure 2.16: Feature importance for the gamma/hadron separation model. A plethora of different features contribute significantly to the decision.

With the trained models available, the data can be reconstructed up to DL2 in a single step. For the energy model, this includes reversing the logarithmic transformation of the energy. For

the disp/sign models, the reconstructed position in the camera is evaluated and then transformed to a position in the sky using the event-wise time and pointing information.

Before the observed data can be analyzed and quantitative conclusions about the sources be drawn, the performance of the measurement process and reconstruction needs to be qualified. The performance includes, but is not limited to, the machine learning models, as events are already lost before that.

This requires defining the inverse problem that every measurement faces.

2.6 Instrument Response

Inverse Problem

The goal of measuring astrophysical sources is to calculate which causal factors led to the observed rates of events without being able to measure the causes themselves directly. To get to a quantitative description of the physical process, one has to include the effects of the measurement.

On the one hand, the telescope does not observe all events that are emitted from within the F.o.V., because

1. Not all events trigger the measurement (not enough recorded light, deadtime, ...)
2. Not all triggered events can be reconstructed up to DL2 (no pixels surviving the cleaning, partially contained, ...)
3. Not all signal events survive the background separation

On the other hand, the properties of the surviving events are not perfectly reconstructed. Both the reconstructed energy and direction deviate from the true properties, and all of these effects depend at least on the energy of the primary particles. On top of that, the dataset will always contain a fraction of hadronic events that survived the selection.

In general, there exists a function R describing the full instrument response, which at a time t gives the probability of reconstructing an event with true physical position p and energy E as one with the reconstructed values $\hat{p}$ and $\hat{E}$. As not all events are reconstructed, the probability to reconstruct a particle at all is generally smaller than one. Since the higher-level analysis involves binning the events in space and energy, this function is best described as a matrix. The measured counts N relate to the true flux Φ as given by Equation 2.3 with some background b.

$$N\left(\hat{E}, \hat{p}\right) = \int \mathrm{d}E\,\mathrm{d}p\, \frac{\mathrm{d}^2\,\Phi(E,p,t)}{\mathrm{d}E\,\mathrm{d}p} R\left(\hat{E}, \hat{p} \mid E, p, t\right) + b\left(\hat{E}, \hat{p}, t\right) \tag{2.3}$$

This is an inverse problem as the measurement only ever provides the reconstructed values. Estimating the instrument response requires labeled data, which go through the full reconstruction chain, including the models trained on the training set. For this, the previously created test dataset is used.

Unfortunately, the matrix R can, in practice, not be estimated due to the high dimensionality of the problem. The resulting matrix is simply too sparsely filled with reasonable amounts of simulated data.

IACTs simplify the problem of describing the instrument response by making the assumption that the general, full response can be decomposed into three independent components, splitting up the detection efficiency and the reconstruction error on the energy and position. In addition, it is assumed that the detector response stays constant over the course of a single observation block of 20 min. With that, the time dependency can be eliminated, and the problem simplifies to Equation 2.4 where R now only describes the instrument response of a single run.

$$R(\hat{p}, \hat{E} \mid p, E) \approx A_{\text{eff}}(p, E)\, E_{\text{disp}}\left(\hat{E} \mid p, E\right) PSF\left(\hat{p} \mid p, E\right) \tag{2.4}$$

The three matrices A_{eff}, E_{disp} and PSF describe the effective area, energy dispersion and point-spread function respectively. They are referred to as Intrument Response Function (IRF)-components and can be calculated from the DL2 test-datasets yielding one set of IRF-components per available node on the simulated grid.

Each observation run, in theory, requires a specific IRF, but as the grid of simulated pointing positions is not expanded for every source, only some discrete points are available. Although `lstchain` supports interpolating IRF-components between different grid points, the methods are still under development [117], and the performance impacts are not fully understood. I therefore decided to use the standard approach of matching to the nearest neighbor as illustrated in Figure 2.17. The parameters used to calculate the distance between an observation and a simulated grid node are the cosine of the θ and the sine of the δ, which is the angle between the orientation of the magnetic field and the telescope's pointing direction.

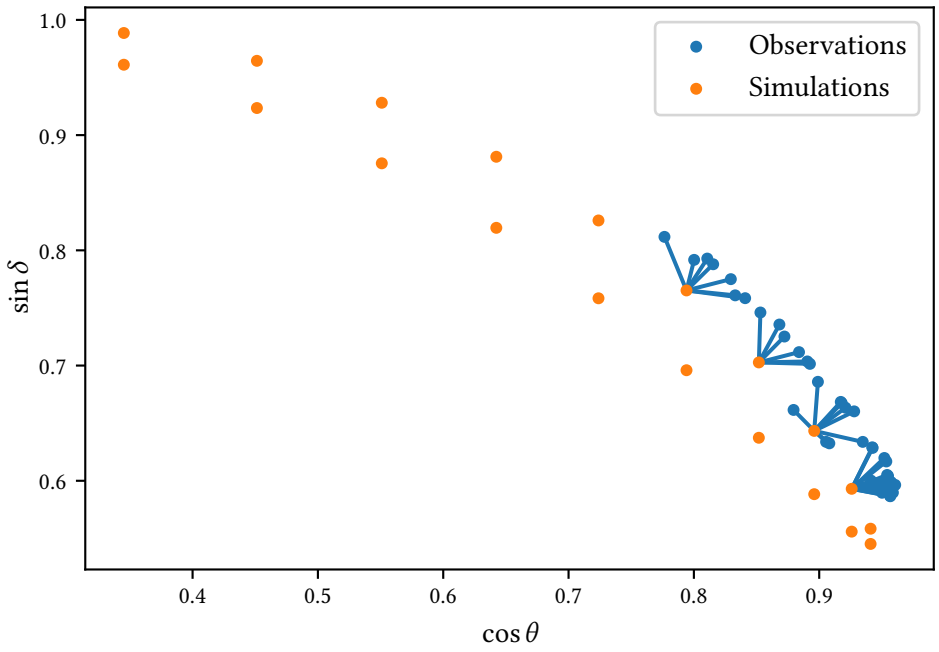

Figure 2.17: Pointing positions of all observations and available nodes on the simulated grid. The lines indicate the closest points on the grid. Only some nodes are matched because the zenith range of the observations is limited, and the simulated declination line does not match the location of the source exactly.

Whether or not the background b of Equation 2.3 should be included in the IRF depends on whether one sees it as a property of the experiment or the physics happening outside the atmosphere. It is usually estimated at least in parts on the observed data itself and not the simulations. For this reason, I will skip it here and return to it after the DL3 files are constructed.

Since, for observed data, most of the recorded images are of hadronic origin, the calculation of the IRF-components is tightly coupled to how strict the signal selection is, with a stricter

selection reducing detection efficiency and background but also changing the reconstruction quality of the remaining dataset. These selection criteria can be chosen in a different way based on the goal of the analysis. For LST-1, they are calculated as quantiles of surviving (simulated) gamma-ray events in each bin of reconstructed energy based on the score of the classifier model. In this analysis, the classifier threshold is calculated to keep 90 % of simulated gamma-ray events. The same threshold values are then evaluated on the observed data.

If the position of the source is known a priori and its extension is minimal, it can be of benefit to also include a cut on the direction of incoming gamma rays as most of the F.o.V. is of no interest. In the present case, where a full three-dimensional analysis is performed, the complete F.o.V. is retained and the IRF-components are calculated in 5 radial bins around the center of the F.o.V..

Generally, all components of the IRF could be non-radially symmetric as well, but at present only radially-symmetric ones are included in the open gamma-ray astro data format (OGADF) schema [93, 118], that is used throughout the LST-1 analyses.

The main causes for a deviation of radial symmetry would be multi-telescope experiments or observations with high zenith distance where the gradient in the F.o.V. can not be ignored. While LST-1 can, to a certain extent, get away with disregarding these effects at low zenith ranges, the full CTAO will have to deal with more general parametrizations of the IRF-components.

Effective Area

First, the analysis has to compensate for the limited detector efficiency depending on the true primary's energy.

For IACTs there is no strict boundary of the detector, as any particle, that creates a pool of Cherenkov light can be measured as long as the telescope stands somewhere in the pool. This creates a problem in the simulations, where the simulated cone needs to be large enough to include all observable showers. The detection efficiency is then directly dependent on the size of this assumed cone: If the simulated cone size is increased, the detection efficiency reduces as additional showers far away from the observatory do not trigger the telescope.

To get to a value that does not depend on the precise simulation settings, the simulated cone size is multiplied with the detection efficiency to get the effective area A_{eff}. This is a constant as long as the simulated cone size is large enough to contain all showers, that would trigger the telescope. Additionally, it also allows for comparisons between experiments and analysis chains and fixes the units in Equation 2.3 where a detector area needs to enter to get a flux of particles per area.

Naturally, the detector efficiency depends on the energy of the particle, as there is a limit to how dim a shower can be to trigger the telescope, and the amount of light depends on the energy.

The matrix depends only on the true properties and can vary with both energy and position. The projection of the effective area on the two axes true energy and true offset from the center of the F.o.V. is shown in Figure 2.18 for all observations: At a fixed offset of 0.4 deg, which roughly equals the wobble-distance in observed data, the effective area rises steeply with energy until a saturation point is reached (left side). The lowest observable energies, as well as the

maximum effective area that can be reached, depend on the zenith distance. In the F.o.V., the effective area is relatively stable with a slight decline at offsets > 1 deg (right side).

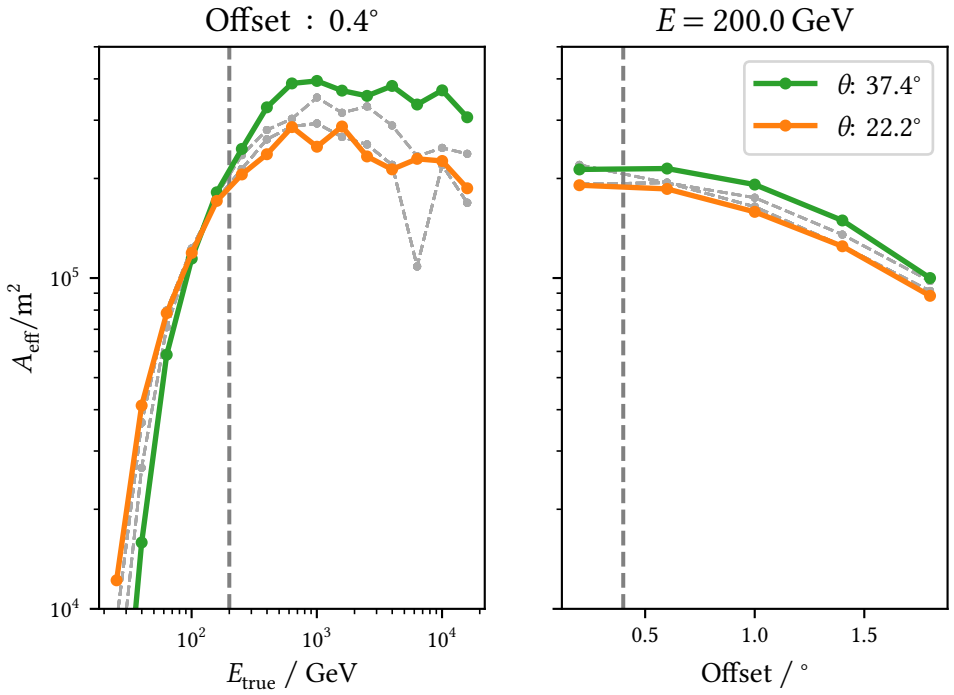

Figure 2.18: Effective area of all observations. Highlighted are the lowest and highest zenith-distance observations. Left: Trend with energy at a fixed offset of 0.4 deg. Higher distances to the zenith increase the effective area at high energies and increase the energy threshold. Right: Performance at different distances to the camera center at a fixed energy of 200 GeV. The effective area degrades only slightly at higher offsets.

Energy migration

In the next step, the effect of the energy estimation is taken into account with the energy dispersion translating between true and reconstructed energies in bins of true energy and F.o.V. offset.

At this point, no more events are lost; but instead, they are dispersed into different bins, so the resulting matrix stores probability density functions $\mathrm{d}P\,/\,\mathrm{d}\mu$ for the energy migration μ, that are normalised to unity:

$$\mu = \frac{E_{\mathrm{reco}}}{E_{\mathrm{true}}} \tag{2.5}$$

$$\int_0^\infty \frac{E_{\mathrm{reco}}}{E_{\mathrm{true}}}\,\mathrm{d}\mu = 1. \tag{2.6}$$

Describing the effect of the energy dispersion to be relative to the true energy allows to set a reasonable range on the μ axis, which shrinks the matrix compared to a matrix with two energy axes.

From the energy migration, the bias and resolution can be calculated at different energies and offsets, which allows for an easier comparison of different energy migrations. In this context, they are defined as:

$$\text{Bias} = \mu - 1 = \frac{E_{\text{reco}} - E_{\text{true}}}{E_{\text{true}}} \tag{2.7}$$

$$\text{Resolution} = \frac{\sqrt{Var(E_{\text{reco}})}}{E_{\text{true}}}. \tag{2.8}$$

The bias of the energy regression is presented in Figure 2.19 showing how far the predictions deviate from the true values on average. At low energies, the model systematically overpredicts, which is linked to selection effects at the threshold: Showers with below-average light-yield for a given true energy are simply not triggered or do not survive the image cleaning at low energies.

The energy resolution in Figure 2.20 shows how much the predictions scatter around the predicted mean energy with a decreasing trend towards higher energies and no trend with offset distance.

Point Spread Function

Lastly, the reconstruction error on the origin direction is taken into account. The *PSF* describes how smeared out a point source will be recorded by the telescope. For IACTs this does not relate to the optical imaging of the Cherenkov photons in the atmosphere but the statistical distribution of the reconstructed positions of many gamma-ray showers in the sky, that originate from the same true position.

Different parametrizations are foreseen in the OGADF-schema. LST-1 uses the most general form of tabulated values.

A typical benchmark value for the *PSF* is the radius at which 68 % of reconstructed values are contained in the circular region of this radius around the true position. This is shown in Figure 2.21 for all observations. Similar to the resolution of the energy migration, the performance generally improves with energy.

A poor directional reconstruction can lead to issues at later stages of the analysis: For the estimation of the background, a region around the assumed source position is excluded, and the background is estimated from other parts of the F.o.V.. This applies to one- and three-dimensional analyses, so the same precautions must be taken: If events are reconstructed so far away from the true source that they end up in the other half of the F.o.V., they inadvertently end up biasing the background estimation.

For the established experiments such as MAGIC this is not a problem in practice because the *PSF* at low energies benefits a lot from stereoscopic observations.

To illustrate the problem, Figure 2.22 shows the 95 % containment radius instead. At energies below $\approx$ 500 GeV, the containment radius exceeds 0.4 deg.

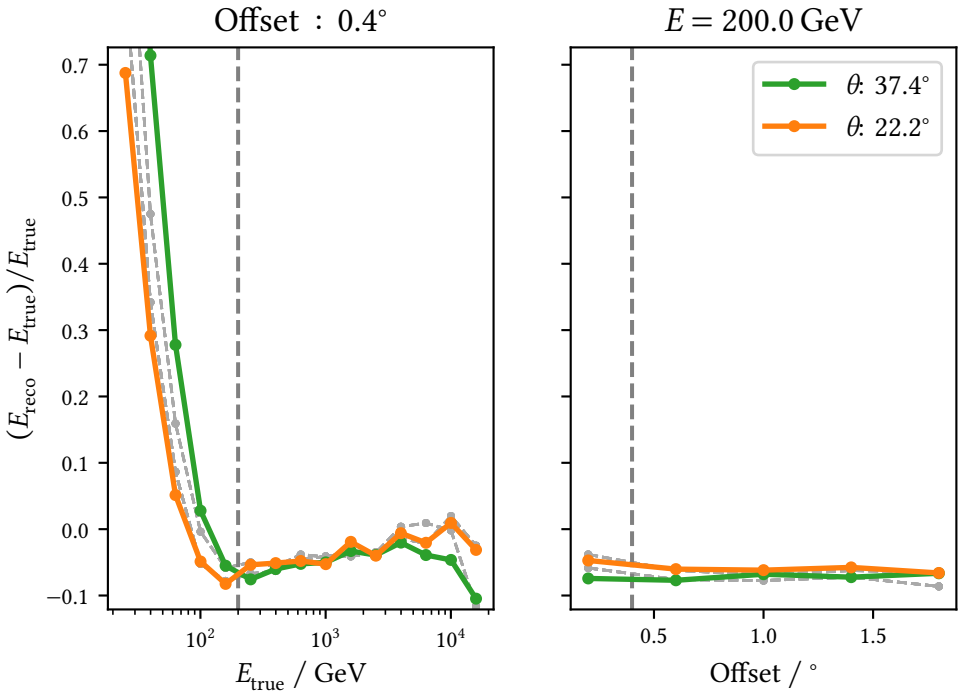

Figure 2.19: Bias of energy dispersion for all observations. Highlighted are the lowest and highest zenith-distance observations. A similar shift of performance with zenith distance as in Figure 2.18 can be observed. Left: Trend with energy at a fixed offset of 0.4 deg. At low energies, the estimator systematically overestimates the true energy. Right: Performance at different distances to the camera center at a fixed energy of 200 GeV. No trend with increasing offset is visible.

This exceeds the wobble-distance of 0.4 deg for the observations considered here and most of all LST-1 observations. LST-1 could choose to observe at higher offsets from the source position to improve on these issues at low energies, but decided to keep the same distance as used in MAGIC for the benefit of simultaneous observations, that could be analyzed together on a low data level as a three-telescope setup.

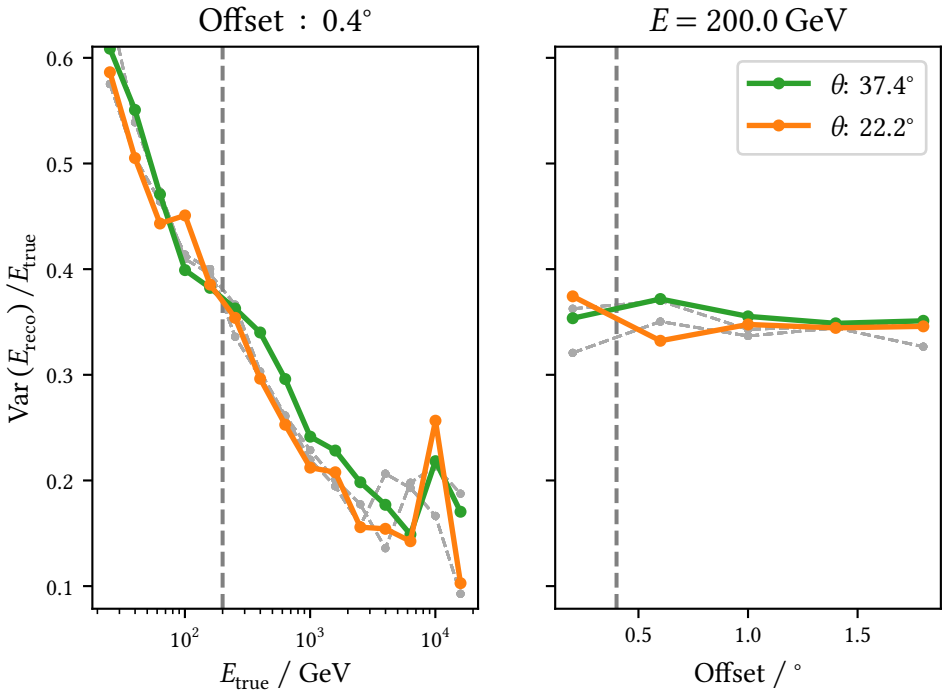

Figure 2.20: Resolution of energy dispersion for all observations. Highlighted are the lowest and highest zenith-distance observations. Left: Trend with energy at a fixed offset of 0.4 deg. At higher energies, the spread of predictions reduces. Right: Performance at different distances to the camera center at a fixed energy of 200 GeV. No trend with offset is visible.

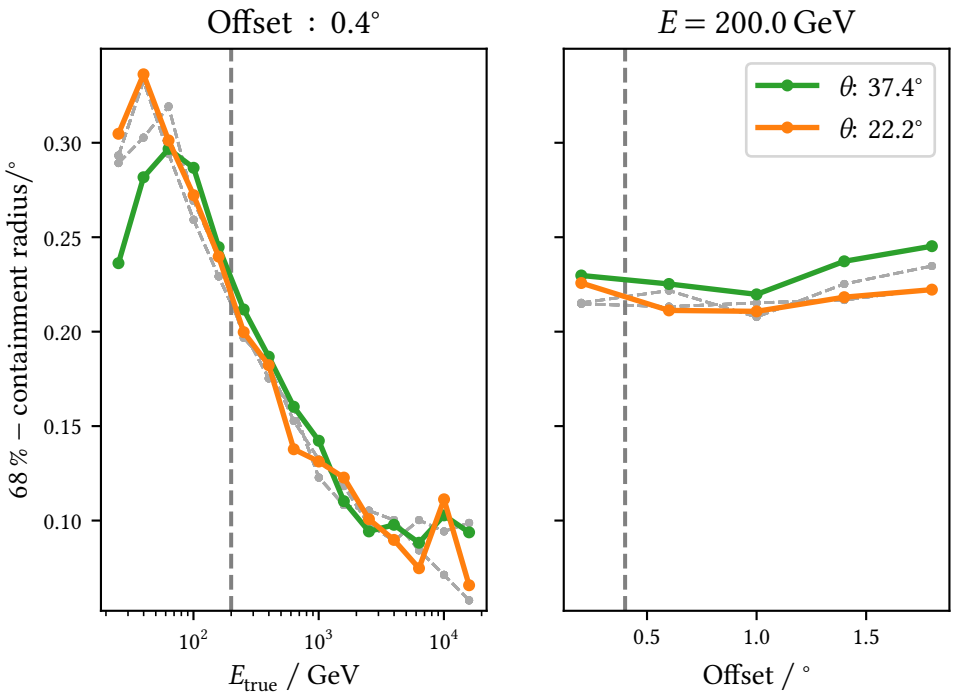

Figure 2.21: 68 %-containment radius of the *PSF* at different energies and offsets. Highlighted are the lowest and highest zenith-distance observations. Left: Trend with energy at a fixed offset of 0.4 deg. At higher energies, the radius decreases as showers become brighter and easier to reconstruct. Right: Performance at different distances to the camera center at a fixed energy of 200 GeV. At offsets > 1 deg a slight worsening of the *PSF* can be observed.

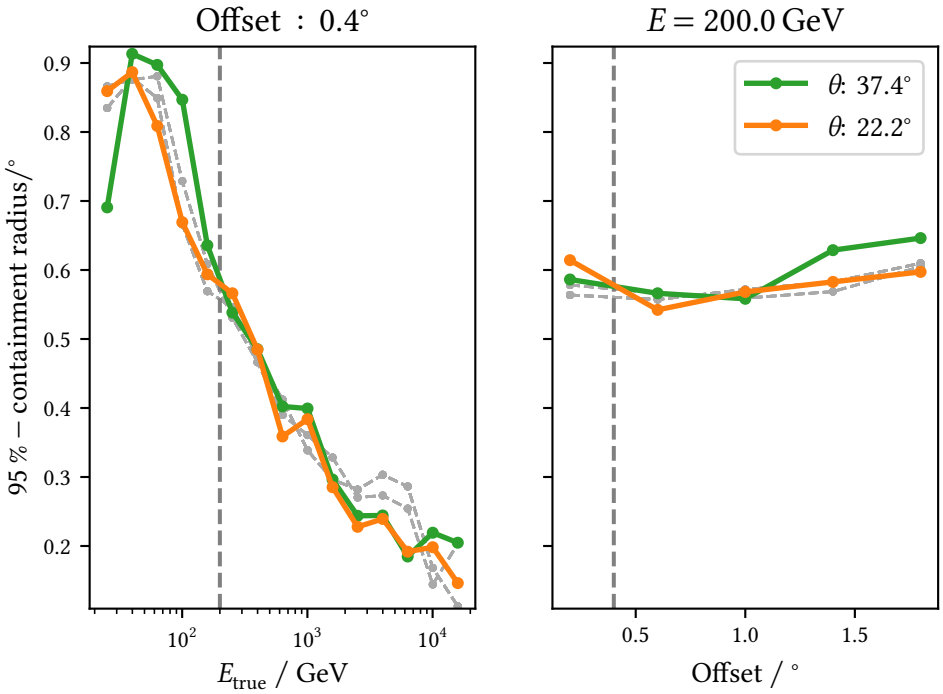

Figure 2.22: Same illustration as in Figure 2.21, but with the 95 %-containment radius instead. At lower energies not all reconstructed showers end up within 0.4 deg.

2.7 Gamma-like Events

With the events that survive the cut on the classifier threshold and the set of IRF-components, the DL3 files can be constructed.

In Figure 2.23, the events of all observations have been added and are shown together with the pointing positions of the observations. Four different pointing positions have been observed. Depending on the source intensity and the used classifier thresholds, an excess around the assumed source position would already be visible here.

In this case, no such excess is visible, and the F.o.V. looks very regular with the counts decreasing towards the edge of the F.o.V..

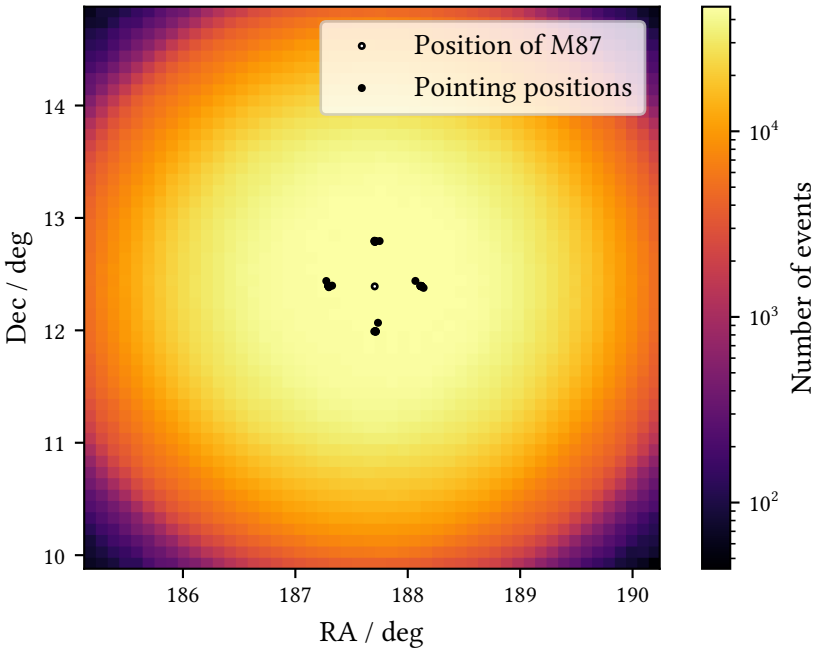

Figure 2.23: Skymap of all gamma-like events at DL3. No clear excess is visible from the position of M87.

A more robust check to see whether there is an excess in gamma-like events coming from the source position is to construct a θ^2-plot. Here θ is the angular distance between the reconstructed shower position and the assumed source position, not to be confused with the θ.

To get a baseline for the number of counts expected if there was no excess, one or more off-positions are chosen in camera coordinates by using an equivalent position in the F.o.V. as another pseudo-source to calculate the distance to. These off-positions are placed in the same radial distance to the center of the camera without overlap. Due to the large *PSF* at low energies, LST-1 analyses use only one off-position at the mirrored position.

The result of this construction is shown in Figure 2.24 in different bins of reconstructed energies. Counts at low energies far exceed the ones at higher energies due to the limited classifier performance and higher event rates.

Using a fixed threshold of $\theta^2 \leq 0.1\,\mathrm{deg}^2 \approx (0.32\,\mathrm{deg})^2$ for all energies, the signal-to-noise ratio S/N and the significance σ [119] can be calculated as

$$N_S = N_{\mathrm{On}} - N_{\mathrm{Off}} \tag{2.9}$$

$$S/N = \frac{N_S}{N_{\mathrm{Off}}} \tag{2.10}$$

$$\sigma = \frac{N_S}{\sqrt{N_{\mathrm{On}} - N_{\mathrm{Off}}}} \tag{2.11}$$

for a single off-position, with N_{On} the counts close to the source position and N_{Off} the counts close to the off position.

The measured distribution of counts near the source position is generally compatible with the background expectation. The non-zero excess from the source position is not statistically significant to the point that a detection could be claimed.

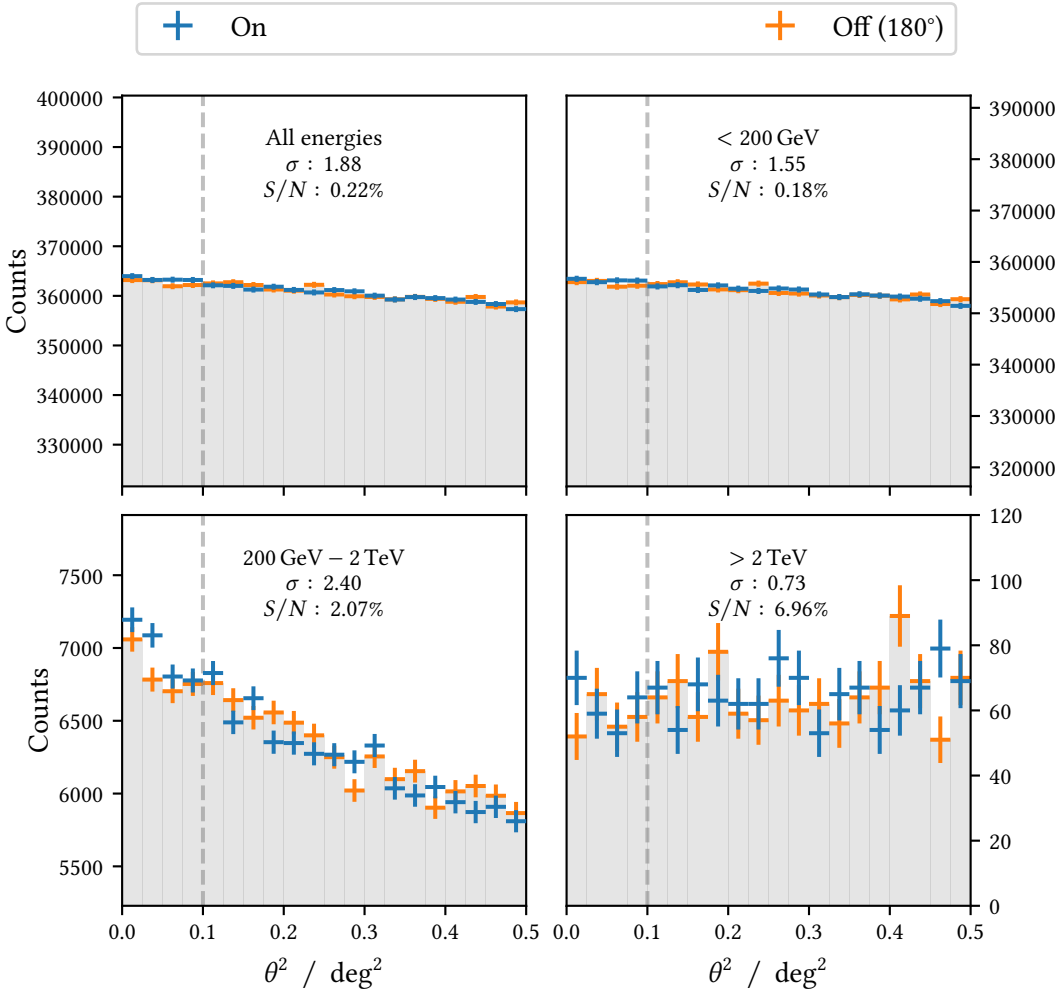

Figure 2.24: θ^2-plot of the gamma-like events at DL3. The distribution of counts in the on-region is very similar to the one in the off-region. At energies above 200 GeV, a small excess can be seen by eye. The stated significance and S/N are calculated on the events with an angular distance of $\theta^2 \leq 0.1\,\mathrm{deg}^2$ as indicated by the vertical line in each plot ($\theta \approx 0.32\,\mathrm{deg}$).

2.8 3D Background Estimation

In addition to the components of the IRF provided by `lstchain`, a three-dimensional analysis requires a background description in the complete F.o.V.. Since a proper background modeling using simulations is not feasible with the available simulations, the approach presented here is based on previous studies within MAGIC [120, 121] and H.E.S.S [122] as well as the related software packages `pybkgmodel` [123] and `acceptance_modelisation` [124].

The approach involves excluding regions with known or expected gamma-ray signal and using the remaining events to estimate the acceptance within the F.o.V.. Since there are multiple pointing positions in the observations, the exclusion region(s) ends up in different positions in the camera and one can fill the complete F.o.V..

This can be done either with the observations of the source directly or with independent observations. Both approaches have their advantages and disadvantages with respect to the available statistics and the associated systematics: On the one hand, using (additionally) observations with no or little sources in the F.o.V. increases the measured counts and disentangles the observed counts from the background prediction. On the other hand, the observing conditions need to match the source observations precisely.

The effects introduced by different observation conditions can in principle be corrected [121, 122], but this requires a telescope performance that is both stable over time and understood to high precision, and a high amount of automation in the data analysis. At the current stage of LST-1 this is not trivial to fulfil because of the limited comparability of the available provenance data. Also, the manual selection and fine-tuning of the simulations and reconstruction models for each observed source might lead to systematic differences in the background acceptance. For these reasons, the current studies describing the background acceptance of LST-1 focus on using the on-source observations directly, which is also what is done here.

Unfortunately, the accuracy of the method at the lowest energies is fundamentally limited by how many gamma-ray events from the excluded source are reconstructed outside the region. At the same time, the size of the exclusion region is limited to the distance of the source to the pointing position, which is close to 0.4 deg, to be able to still fill the complete F.o.V.. This mainly affects the low-energy region where the directional reconstruction is worse. In this analysis, the source is not very bright (recall Figure 2.24), which limits the potential influence. However, it leads to the odd situation where bright sources, such as the Crab Nebula, that usually acts as a benchmark and cross-check for analyses, are harder to model correctly, at least at low energies. A larger offset distance would help LST-1 but also make it more difficult to observe parallel to MAGIC, which has a smaller F.o.V.. Note that while a three-dimensional background construction is more sensitive to this issue, events being reconstructed far away from the source position also affect the standard one-dimensional background estimation. It is also an issue that will be resolved by adding the other LSTs and observing in stereo.

In contrast to the IRF components, the current format ([93, 118]) already allows for the background models to be saved either in two dimensions with only an offset axis or in three dimensions in a cartesian spatial grid. The three-dimensional approach does allow for a better description of the background if the shape is not radially symmetric and event statistic is of no concern, whereas the two-dimensional approach makes it possible to describe a radially

symmetric background even with very limited statistics.

In principle, the same arguments as for the effective area apply: To first order the background of single telescope observations at low zenith distances should be radially symmetric. However, it is more critical to correctly describe the shape of the background acceptance because any misrepresentation directly influences the resulting excess calculation, whereas the effective area enters at a later stage, transforming the excess counts to physical flux units. A three-dimensional parametrization is therefore preferred if the available statistic allows for it.

To take the exclusion region into account, a two-dimensional (spatial) grid is constructed first in coordinates relative to the pointing direction of each observation. The same energy binning as for the IRF-components is used to avoid interpolation between energies. As an intermediate product, the following maps are then produced for every observation on this grid:

- a map of event counts for every bin in energy
- a map of the observation time

Bins that fall into the exclusion region have their value set to zero. To fill the maps, the observations are split up in multiple bins of observation time to account for the movement of the source in the F.o.V.. This is shown illustratively in Figure 2.25 for one bin of energy and observation.

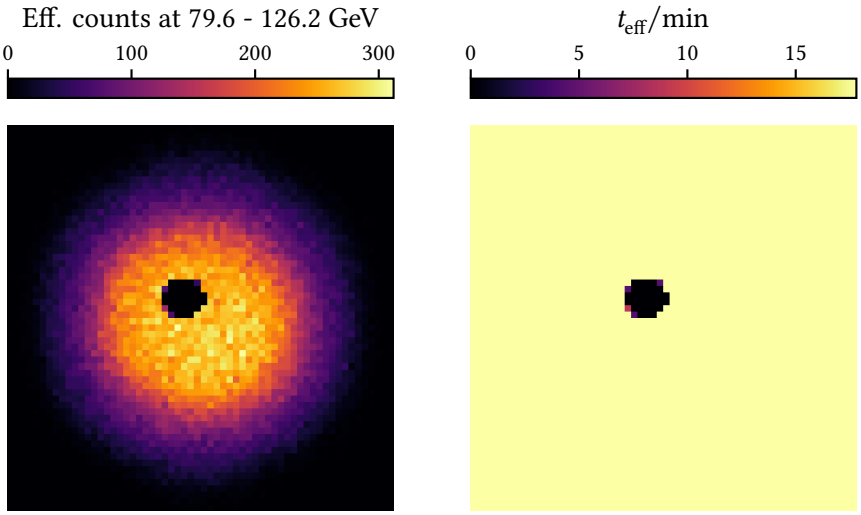

Figure 2.25: Example maps for the background creation using the data from observation 12745. The excluded region enters with an observation time of zero, and all counts are discarded. Due to the movement of the source in the F.o.V. some bins at the edge of the region are only partially excluded. Left: Measured counts in one bin of energy. Right: Effective observation time.

To fill the missing part in the F.o.V., multiple observations with different pointing positions relative to the source are then combined. This is always a compromise between available count statistics and systematic differences between different observations. For this analysis, I define three groups of observations to combine individually as highlighted in Figure 2.26.

First of all, there is a group of observations that was taken before the eruption of the volcano at La Palma, which are also the only observations in this dataset without the final trigger

settings. While the analyses of Crab Nebula data [79] suggest that with the low-level selection criteria applied in this analysis, the distribution of excess events is similar to later data, it would be a stretch to make conclusions about the rates of non-excess events in other parts of the F.o.V. from this fact alone. Therefore, it seems like a natural step to treat them individually.

The second group includes all observations after the volcano eruption with a distance between the pointing position of the telescope and distance to the zenith of ≤ 30 deg. With the strict selection on the observation conditions applied before, there is no reason why there should be a systematic difference between these observations.

Lastly, all observations with higher zenith distances are collected into one group. This set of observations does not contain any pre-volcano data.

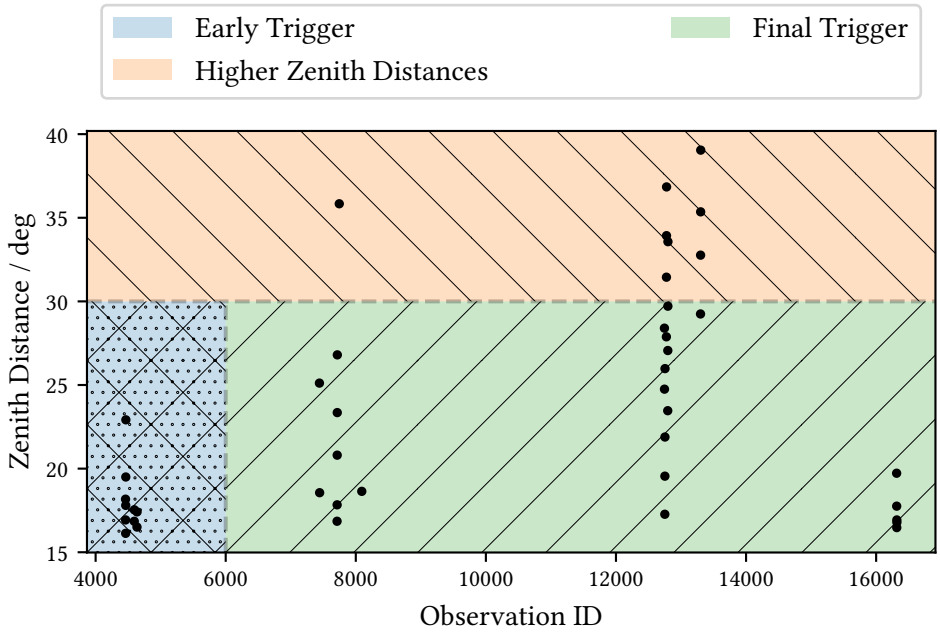

Figure 2.26: Grouping of observations for the background creation. Observations are binned in time and zenith distance, with the early observations taken before both the final trigger settings and the volcano eruption.

From the per-observation maps, the three-dimensional background maps are then created by stacking the counts and exposure maps individually and dividing the results which is illustrated in Figure 2.27 in one bin of energy.

This way, maps of the predicted event rate are created for every bin of energy. The result for the post-volcano low-zenith observations is shown in Figure 2.28. At low energies, the F.o.V. does not extend over the full range, but all bins within are filled. A clear asymmetry can be seen at low energies below ≈ 200 GeV. At energies above ≈ 1 TeV, the counts extend over the full range of bins, but empty bins occur. The acceptance is no longer maximal in the center of the F.o.V., but instead, in a ring around the center. This is a known feature related to the size of shower images at high shower energies and their containment in the camera. It follows from the fact that more light is produced at higher energies of the primary particle and the camera

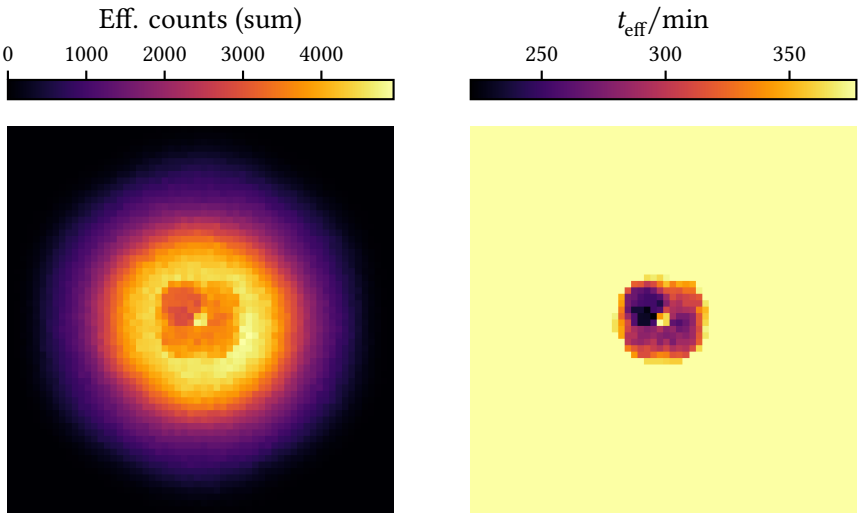

Figure 2.27: Illustration of the effective counts and time maps produced for the background creation. Left: Effective counts stacked over all energies divided by the effective observation time. Right: Effective observation time. The observation time is constant where no exclusion is applied.

images are larger. As there is an offset between the center of gravity of the intensity distribution and shower impact, showers coming from the center of the F.o.V. end up in the outer parts of the camera, where they are often not fully contained anymore and are removed in the analysis.

In order to avoid interpolation artifacts in `gammapy`, it is important to produce background models that are mostly free of empty bins. Figure 2.29 illustrates how the ratio of filled spatial bins changes with energy. A coarser spatial binning could improve the situation at higher energies slightly at the expense of a less accurate description at lower energies.

In contrast to the fine three-dimensional maps, Figure 2.30 shows the maps resulting from a two-dimensional model with just eight offset bins. This binning is the same as for the other IRF-components. It fails to capture the asymmetry at low energies but provides a smooth model at higher energies. For this reason, spatial analyses within LST-1 so far focus mostly on the higher energy regions where the asymmetry is less pronounced and such a model provides a sufficient description.

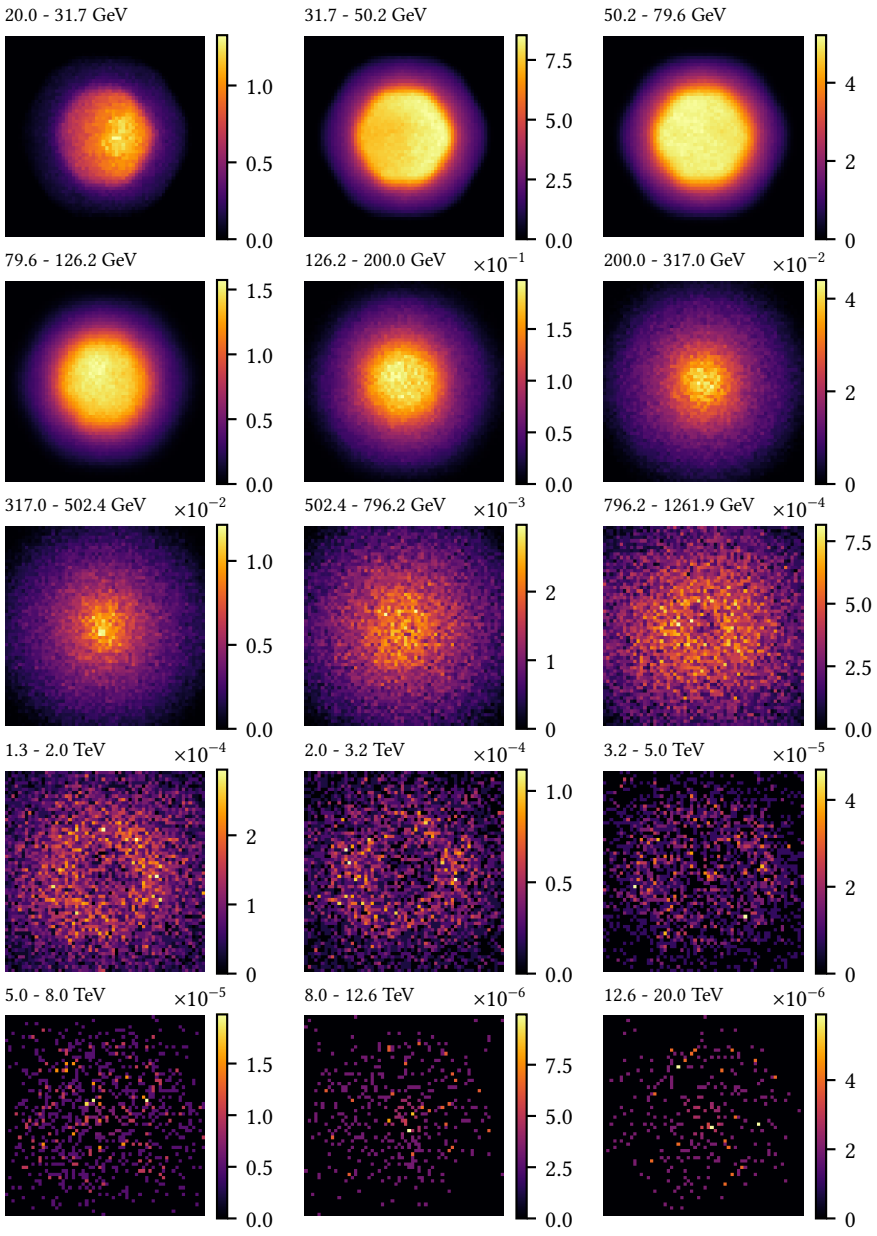

Figure 2.28: Event rates predicted by the three-dimensional low zenith distance post-volcano background model in units of $\mathrm{MeV}^{-1}\,\mathrm{s}^{-1}\,\mathrm{sr}^{-1}$. Besides the absolute count rates also the spatial shape changes with energy: At low energies, the acceptance is highest in the center of the F.o.V. while at higher energies a ring forms and increases in radius.

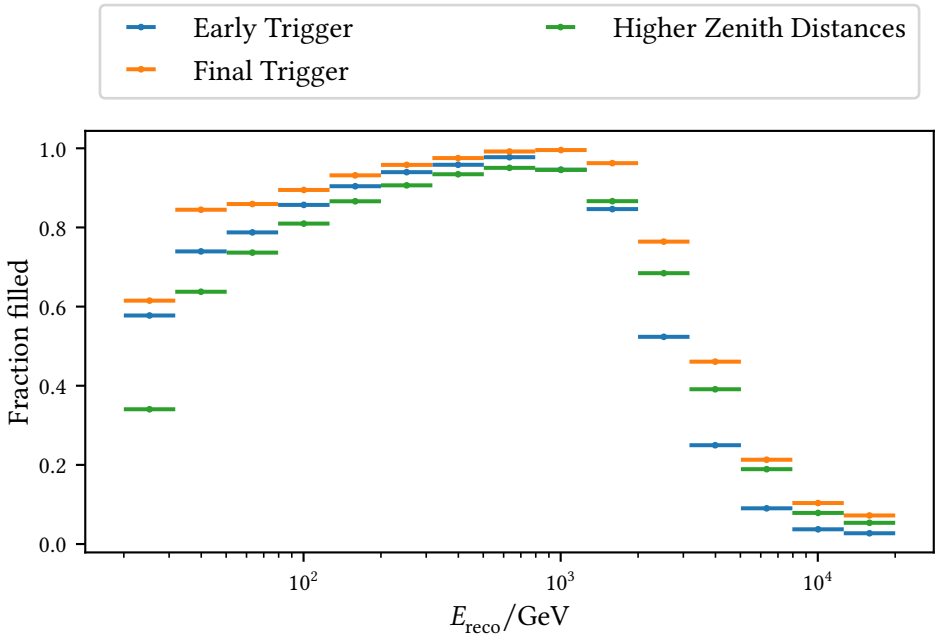

Figure 2.29: Fraction of filled spatial bins for the intermediate stacked count maps in each of the groups marked in Figure 2.26. At low energies, the F.o.V. does not extend over the full range, whereas at higher energies, the measured count statistic is limited.

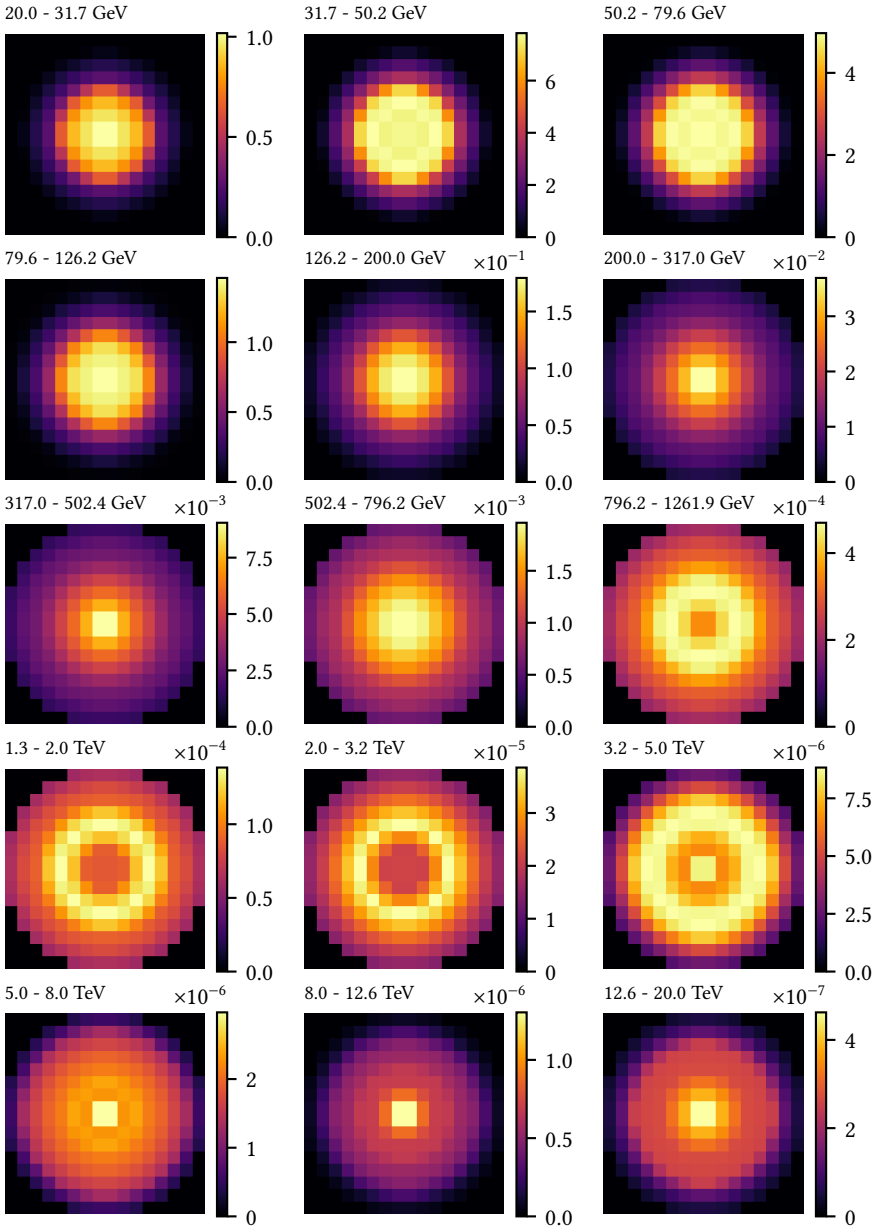

Figure 2.30: Event rates predicted by the two-dimensional low zenith distance post-volcano background model in units of $\mathrm{MeV}^{-1}\,\mathrm{s}^{-1}\,\mathrm{sr}^{-1}$ evaluated in spatial bins at different energies. The acceptance is radially symmetric by construction.

With the telescope-specific steps performed, the data can be analysed using the high-level framework `gammapy`. The analysis is based on the evaluation of likelihood-functions as explained in Section 3.1. Section 3.2 describes how the final dataset on which the likelihoods can be evaluated, are created.

In the final sections, the measured excess is modeled: First, significance maps are constructed in Section 3.3 to quantify the measured excess using the complete background description. Next, in Section 3.4, a model for the spectral distribution of the excess is fitted to the data and the results compared to previous measuremts of the source. Lastly, in Section 3.5, the results are used to constrain dark-matter annihilation from the halo, that is expected to have formed around M87.

3.1 Maximum Likelihood Method

The statistical fitting and test routines in `gammapy` use likelihood-based methods where every bin in the DL4 datasets contributes an independent term to the likelihood. It is assumed, that the event counts in each bin are distributed according to a Poissonian distribution:

$$P\left(N_{\text{obs}} \mid N_{\text{pred}}\right) = \frac{N_{\text{pred}}^{N_{\text{obs}}}}{N_{\text{obs}}!} \exp\left(-N_{\text{pred}}\right). \tag{3.1}$$

The full likelihood for an observation is then obtained as the product of the likelihood terms:

$$L = \prod_i P\left(N_{\text{obs, i}} \mid N_{\text{pred, i}}\right). \tag{3.2}$$

Here, the variable i combines all bins and observations.

The data is best described by the model when the likelihood is maximal. In practice, the equivalent description of minimizing the negative logarithm of the likelihood is used instead, which transforms the product in Equation 3.2 to a sum over the individual contributions with an additional factor of two, that makes the result asymptotically X^2-distributed.

$$l = -2 \log L = 2 \sum_i -N_{\text{obs, i}} \log\left(N_{\text{pred, i}}\right) + N_{\text{pred, i}} + \log\left(N_{\text{obs, i}}!\right) \tag{3.3}$$

As the last term does not include the predicted counts, it does not depend on the model parameters. This constant term is, therefore, ignored since the absolute value of the likelihood does not contain any information. With this, one ends up with Equation 3.4.

$$C = 2 \log L - \sum_i \log \left(N_{\text{obs, i}} \right) = 2 \sum_i N_{\text{pred, i}} - N_{\text{obs, i}} \log \left(N_{\text{pred, i}} \right) \tag{3.4}$$

This is the cash statistic for low count Poisson data [125], which is used in `gammapy` whenever the background is described by some model and not estimated from an independent measurement. The expected event counts N_{pred} are the result of folding the physical flux Φ, that is obtained from the evaluation of the source models, with the instrument response and adding the expected background counts according to Equation 3.5.

$$N_{\text{pred}} \, \mathrm{d}p \, \mathrm{d}E = t_{\text{obs}} \circ \left(E_{\text{disp}} \circ PSF \circ A_{\text{eff}} * \phi(\Theta) + b \right) \tag{3.5}$$

The minimization is performed using the package `iminuit` [126, 127].

3.2 Binned Datasets

The first analysis step in gammapy is a further reduction of the observed DL3 data to binned datasets on which the likelihood terms can be calculated. For this, a geometry is defined with axes for reconstructed and true energy as well as spatial bins in ICRS coordinates.

For the spatial binning, a quadratic sky-region with a side-length of 4 degrees is constructed with the assumed source position in the center and a binsize of 0.04 deg.

To avoid the regions in the parameter-space that are known to be associated with the highest systematic uncertainties, gammapy is able to define regions that should be masked in further analysis. The highest uncertainty generally occurs at the edges of the F.o.V. and at the lowest energies.

For this reason, the contribution of each observation is restricted to the inner 1.5 deg around the pointing position. Furthermore, a mask is applied in energy based on the value of the effective area: Energy bins for which A_{eff} is below 5 % of the maximum value also do not contribute to higher-level data products.

The specific percentage value does not contain much information, especially because it is applied on the reconstructed energy, whereas A_{eff} is defined in terms of the true energy. It does, however, provide a way to define a lower energy bound that scales with the observation conditions. In practice, the lowest energy bin from 20 GeV − 31.7 GeV is masked for all observations. For higher zenith distances, the second bin from 31.7 GeV − 50.2 GeV is also masked.

While the observed events can be directly binned in the sky-region geometry, the IRF-components need to be evaluated at this new geometry, which is not expressed in F.o.V.-coordinates.

The result of the evaluation of the background models on the sky geometry is shown in Figure 3.1 for the three-dimensional model and Figure 3.2 for the two-dimensional model for a single observation. To interpolate between the different spatial bins, nearest neighbor interpolation is used. The relative difference between both is shown in Figure 3.3. This indicates again that a two-dimensional background model is insufficient at low energies.

Note that although the energy bins are the same in the construction of the model and the sky geometry, gammapy will still try to interpolate between energies. This is a side-consequence of the flexible approach in gammapy where the content in the new bins is obtained as an integral between the values at the new edges. At the same time, the model is assumed to be defined exclusively at the bin center and the edge values are obtained via linear interpolation in a log-log space of the neighboring bin centers. While this makes it possible to evaluate models at arbitrary geometries, a lot of information about the spatial shape is diffused between bins. If the binning is the same between model and sky geometry, this step is completely superfluous and, in my opinion, harmful, which is why it is avoided in this analysis.

Therefore, a hybrid approach is chosen to model the background at this data level, making use of the three- and two-dimensional parametrizations: Within the inner 1.5 deg, the maps are filled also at low energies as shown in Figure 3.4. This makes is possible to use the three-dimensional model for energies up to 2 TeV. For the energies above, the two-dimensional parametrization is used.

During the creation of the datasets, the background map is further adapted to better match

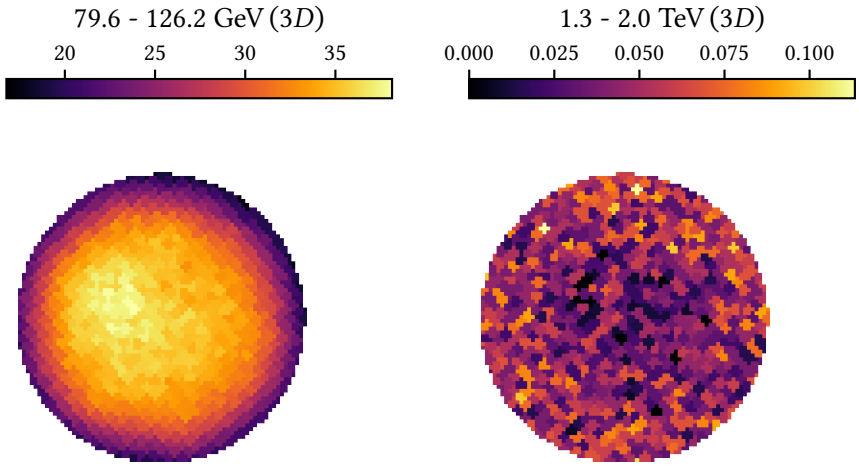

Figure 3.1: Predicted background counts in a region of 1.5 deg center of the F.o.V. for the three-dimensional background-model on one observation. Counts outside this region are masked in the analysis. Since the sky geometry is centered on the assumed source position, but the pointing of the telescope is offset, the region is not in the center.

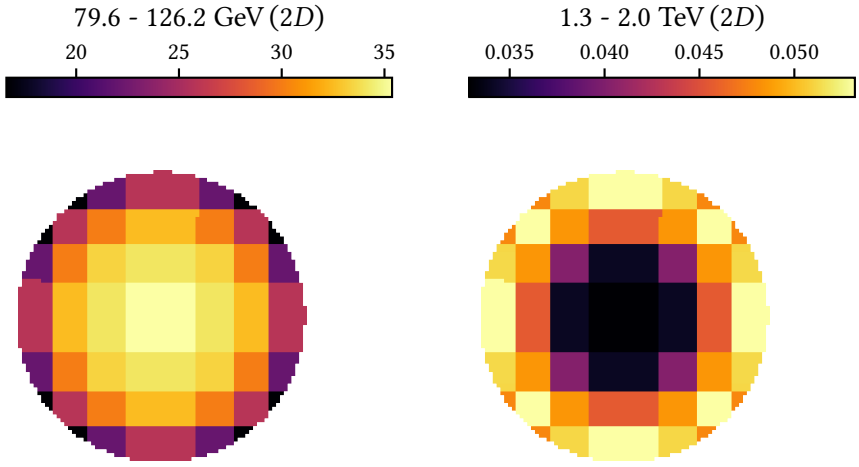

Figure 3.2: Predicted background counts in a region of 1.5 deg center of the F.o.V. for the two-dimensional background model on one observation. Counts outside this region are masked in the analysis. Since the sky geometry is centered on the assumed source position, but the pointing of the telescope is offset, the region is not in the center.

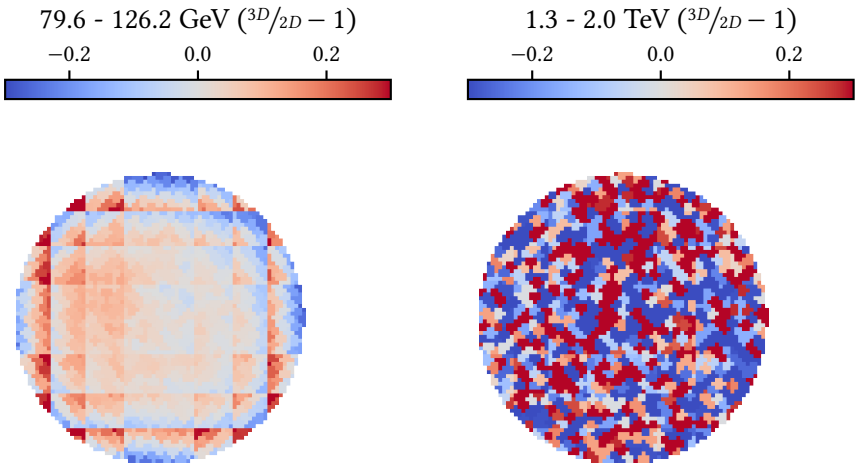

Figure 3.3: Relative difference between the three- and two-dimensional background models from Figure 3.1 and Figure 3.2. At low energies, the two-dimensional parametrization is not sufficient. The repeating gradient within the bins can be solved with a finer binning, but there is also a gradient from left to right that requires the more general model to be properly described in the data.

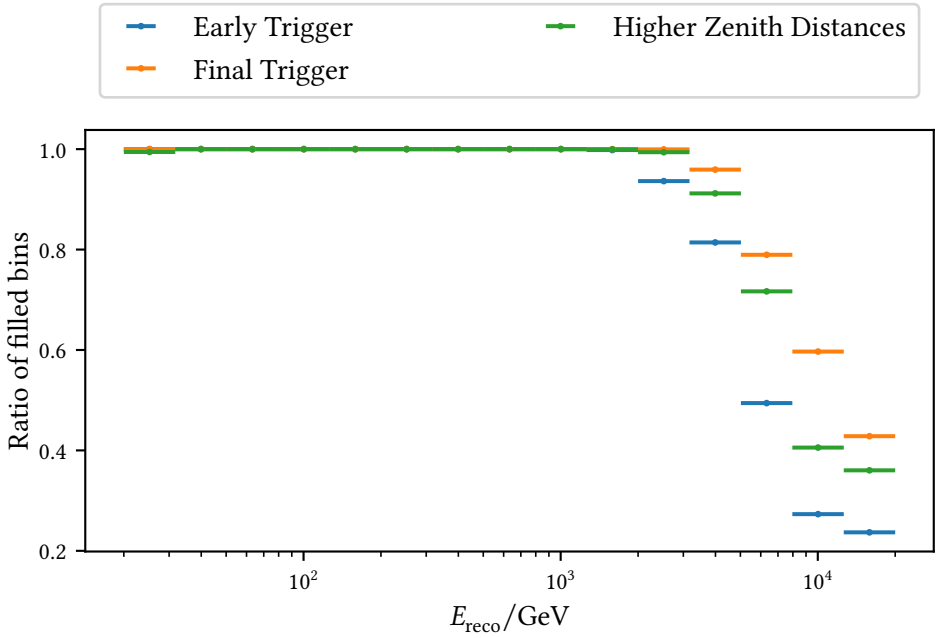

Figure 3.4: Fraction of filled spatial bins after evaluating the different background models on the DL4 sky geometry. With the restricted offset distance, most bins are filled at energies up to ≈ 2 TeV. At energies above this point, the two-dimensional parametrization is used to avoid bins with zero predicted background counts.

each single observation: In every bin of reconstructed energy, the map of predicted background counts is multiplied with a dimensionless factor. The source region is excluded once again. This makes it possible to compensate for some of the differences between observations. The best parameters are found using a maximum likelihood fit as described before.

The resulting dataset for a single observation is shown in Figure 3.5. The agreement of the event rates is much improved after the fit of the norm parameters.

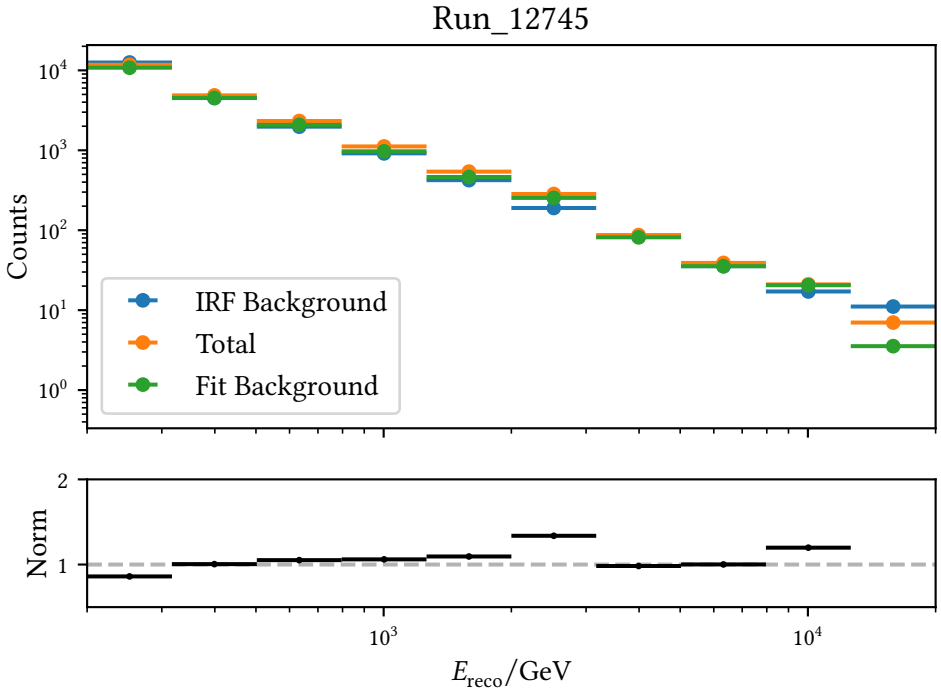

Figure 3.5: Event rates for the dataset constructed from observation 12745. Top: Event rates including the source region. Before the fit, the background model under- or overestimates the event rates in some bins. After the fit, the rates are much closer. Bottom: Background norm parameters from a fit that excludes the source region.

While it is possible to evaluate models on datasets at once, stacking individual observations can be beneficial. This reduces the number of likelihood terms and smoothes out remaining issues in the datasets. The stacked dataset is illustrated in Figure 3.6 with the background exclusion region added and the contribution of all energy bins summed.

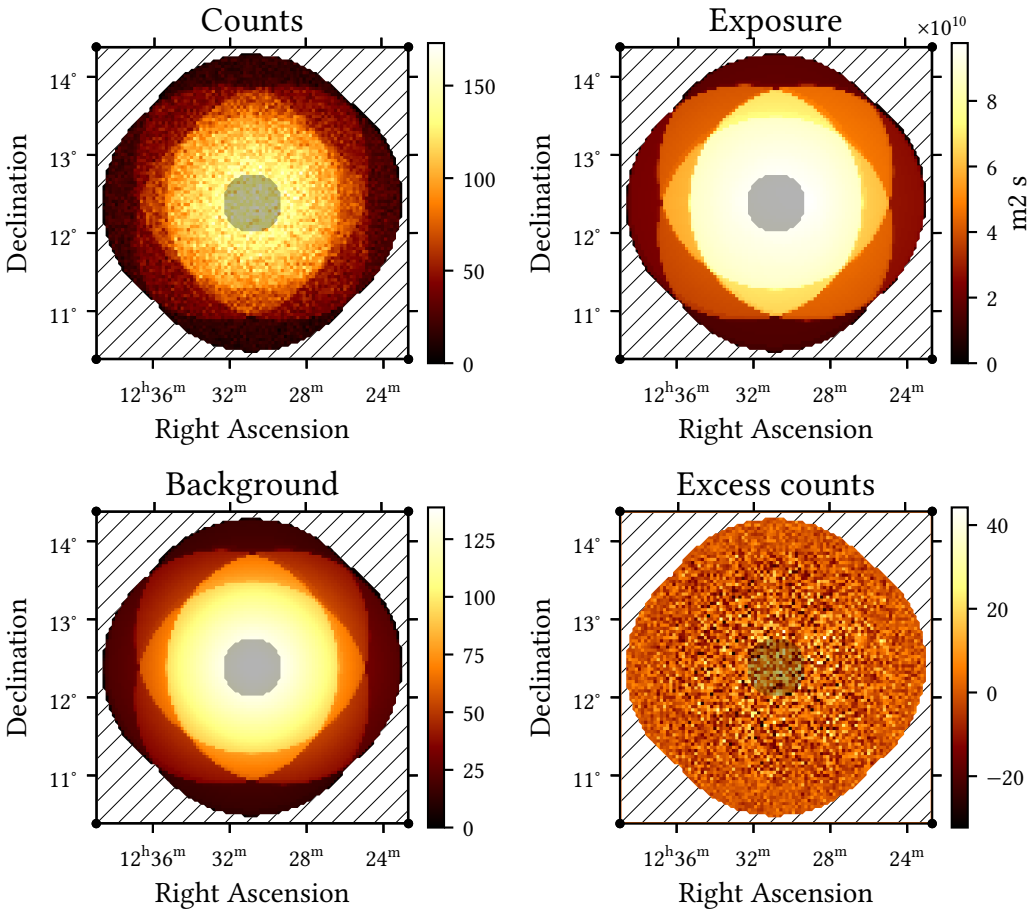

Figure 3.6: Stacked dataset at DL4 summed over all energies. The white dashed regions are masked from the analysis as they are too far away from the pointing position. The source position is in the center of the geometry, with the dark shaded region indicating the region that is excluded for the fit of the background.

3.3 Significance Maps

To draw conclusions about the measured excess counts, it is possible to create maps of the correlated excess counts and significances in `gammapy`.

Using the `ExcessMapEstimator`, significances are calculated in each spatial bin of the sky geometry from a hypotheses test using again the cash statistic Equation 3.4. In this case, the alternative to the null hypotheses of $N_{\text{pred}} = N_{\text{bkgmodel}}$ is the one maximizing the likelihood by predicting exactly the observed counts $N_{\text{pred}} = N_{\text{obs}}$.

To correlate the bins, the maps are first convolved with an isotropic circular kernel, the `Tophat2DKernel`, with a radius of 0.1 deg. The exposure in reconstructed energy is estimated assuming a power-law of the form:

$$\Phi(E) = \Phi_0 \left(\frac{E}{E_0}^{-\gamma} \right) \tag{3.6}$$

with index $\gamma = 2$.

The square root of the difference in the test statistic values Δts is then interpreted as the significance σ of the measured excess[1]. Since it is often useful to compare positive and negative excess values, negative significance values are defined according to Equation 3.8.

$$\Delta ts = ts_0 - ts_{\text{max}} \tag{3.7}$$

$$\sigma = \begin{cases} \sqrt{\Delta ts} & \text{if excess } > 0 \\ -\sqrt{-\Delta ts} & \text{if excess } < 0 \end{cases} \tag{3.8}$$

For the stacked dataset, this produces the maps displayed in Figure 3.7 for the full dataset and the one with only the energy bins > 200 GeV. No obvious features show up besides a small excess from the source region at the higher energies.

To more accurately determine if there is indeed an excess of events coming form the source region, one can now compare the significance values in bins inside and outside of the region. This also makes it possible to quantify how well the background model describes the data: At least in the asymptotic case, the significance values should be distributed according to a standard normal distribution if the model accurately predicts the Poissonian mean and differences in the measurement come only from the sampling process.

A histogram of both distributions along with a fit of a normal distribution

$$f(x \mid \mu, \sigma) = \frac{1}{\sigma\sqrt{2\pi}} e^{\frac{1}{2}\left(\frac{x-\mu}{\sigma}\right)^2}$$

is displayed in Figure 3.8 showing a reasonable agreement in the off-region with a symmetric shape centered on zero and no obvious artifacts.

The fact that the distribution in the off region is slightly wider than expected from the ideal can be attributed to small systematic problems in the creation of the background, possibly from

[1] For some reason `gammapy` refers to the difference in test statistics as *ts*. Since this is already an acronym for test statistic, I deviate from that and introduce the extra *Delta*.

signal events reconstructed outside of the exclusion. In the source region, the distribution is shifted slightly to values larger than zero. Over 200 GeV, the two distributions are more distinct and the width of the off-distribution is smaller.

There is no direct equivalent to claiming a certain significance on a source detection in a one-dimensional analysis from these values, but we can come to a similar qualitative description as from Figure 2.24 of a non-significant positive excess in the source region.

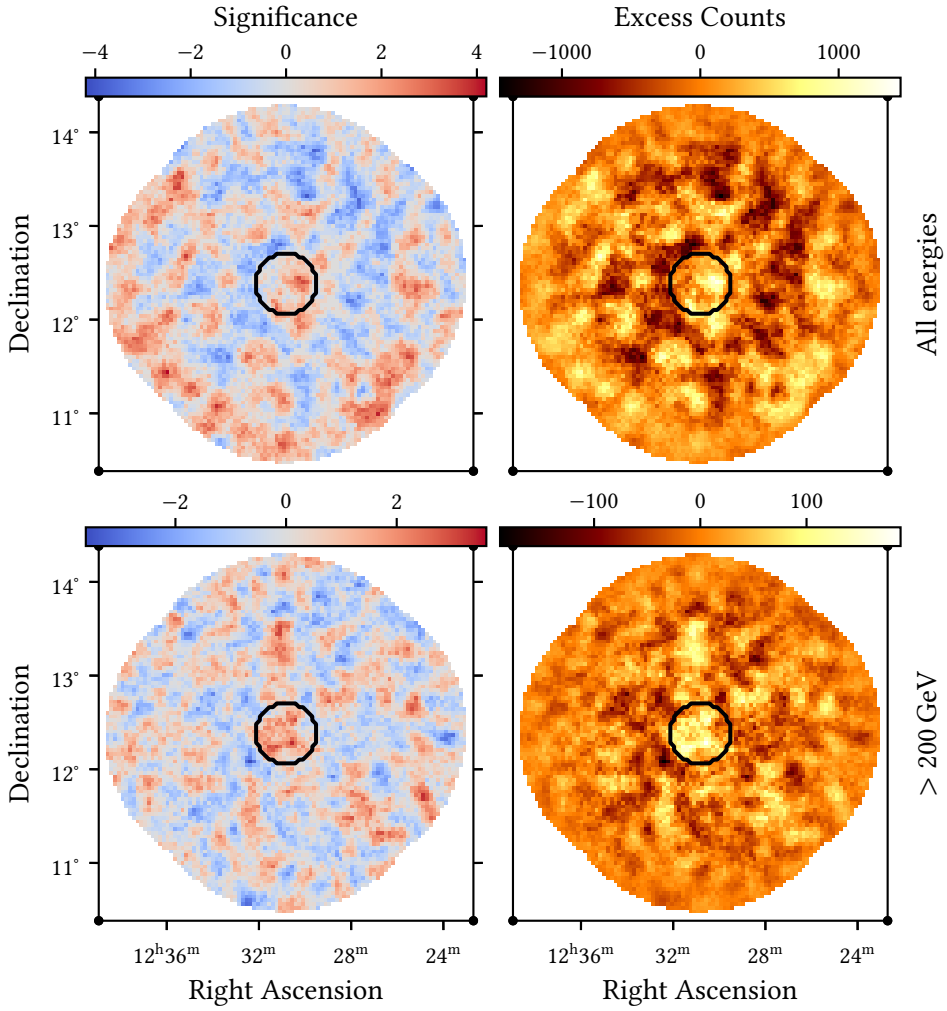

Figure 3.7: Significance and excess maps as obtained with the `ExcessMapEstimator` on the stacked dataset. Top: Significances and excess estimated on the full dataset. Bottom: Significances and excess estimated on the reduced dataset with only the energies above 200 GeV contributing.

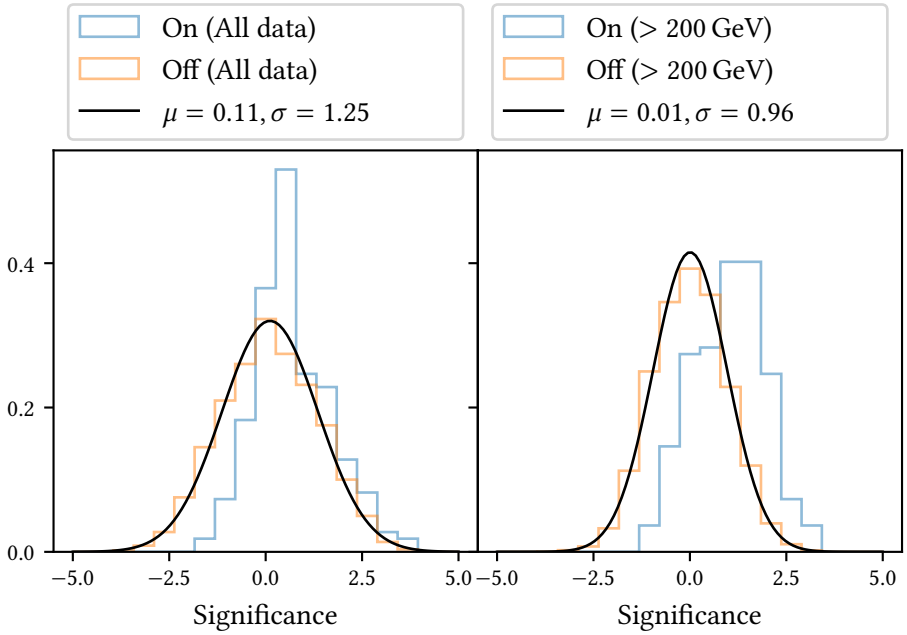

Figure 3.8: Histograms of the significance values. On and off refer to bins inside and outside the marked region in Figure 3.7. Left: Full dataset / upper part of Figure 3.7. Right: Reduced dataset / lower part of Figure 3.7. The distribution in the source region is shifted slightly towards positive values.

3.4 Modelling the Source

It is not possible to claim a detection of the source with these results. Despite that, it is interesting to compare the measured excess to previous measurements of M87 in a low state. Since the excess is small, the position and spatial extension are not treated as free parameters. Instead, the source is modeled as a point source at the nominal position. For the spectral shape, an unbroken power-law model of the form Equation 3.6 is assumed. Further setting the reference energy E_0 to 784 GeV allows for a direct comparison to published results from H.E.S.S and MAGIC and for a power-law model only changes the normalization Φ_0.

The parameters resulting from a fit on the stacked dataset are listed in Table 3.1 and shown in Figure 3.9 with measurements from H.E.S.S and MAGIC during low-states. For comparison with the published results, the integral flux above the energy of 400 GeV is included as well.

The results obtained here are compatible with other low-state measurements, given that these also show some variation. Taking into account that there are no reported flares of M87 in the observed timeframe and the results from [62] indicate that the flux during a low-state should indeed be constant over longer timescales, this can be seen as a confirmation of the LST-1 performance.

Table 3.1: Parameters of the power-law models and integral flux over 400 GeV obtained in different years and activity states.

$\frac{\Phi_0}{10^{-12}\,\mathrm{TeV^{-1}\,s^{-1}\,cm^{-2}}}$	γ	$\frac{\Phi_{>400\,\mathrm{GeV}}}{10^{-12}\,\mathrm{s^{-1}\,cm^{-2}}}$	Observation
0.46 ± 0.15	2.62 ± 0.35	0.51 ± 0.22	H.E.S.S 2004 (low) [59]
2.01 ± 0.28	2.22 ± 0.15	1.97 ± 0.44	H.E.S.S 2005 (high) [59]
0.92 ± 0.24	2.21 ± 0.21	0.90 ± 0.44	MAGIC 2005-2007 (low) [128]
1.30 ± 0.23	2.31 ± 0.17	1.31 ± 0.38	VERITAS 2007 (low) [60]
5.06 ± 0.66	2.30 ± 0.17	5.09 ± 1.00	MAGIC 2008 (high) [129]
8.03 ± 0.51	2.19 ± 0.07	7.82 ± 0.80	VERITAS 2010 (high) [130]
0.71 ± 0.06	2.41 ± 0.07	0.74 ± 0.08	MAGIC 2012-2015 (high) [62]
1.00 ± 0.71	2.35 ± 0.07	1.44 ± 0.88	This work

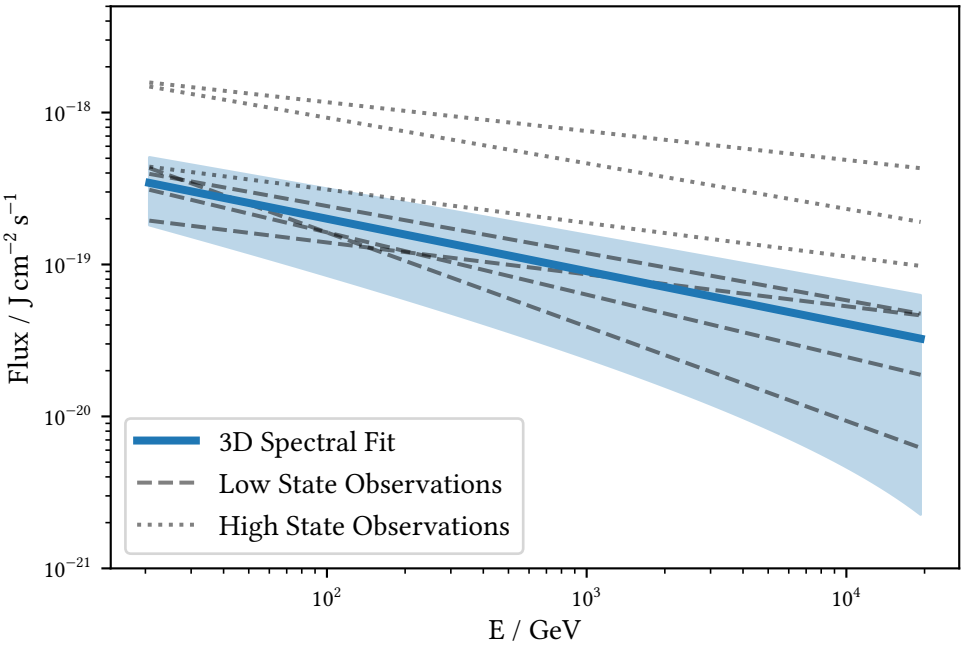

Figure 3.9: Obtained spectral fit along with other measurements of M87 during low and high states. Model parameters are the same as in Table 3.1. The resulting spectrum from this analysis is consistent with other measurements during states of low emission.

3.5 Upper Limits on Dark Matter Annihilation

M87 is also a prime target for dark matter searches, especially since the origin of the low-state emission is still unclear [131, 132]. Due to the limited angular resolution of IACTs and the low measured flux, it is not possible to confidently differentiate between different emission scenarios like emission from the point source, a component from interacting cosmic rays and the dark matter flux. Instead, the most robust approach is to assume that the low-state emission arises purely from the annihilation of dark matter[2] . Since it is unlikely that the baryonic matter, which is accreted through the black hole, does not contribute to the measured excess at all, limits derived with this assumption are generally on the conservative side.

The expected flux from dark matter annihilation in a region of the sky $\Delta\Omega$ can be described with a particle physics term $^{\mathrm{d}\Phi}/_{\mathrm{d}E}$ and an astrophysical term including the dark matter density ρ, as written down in a simplified form in Equation 3.9. The result of evaluating the integrals in the astrophysical term is commonly referred to as the J-factor.

$$\Phi = \frac{\mathrm{d}\Phi}{\mathrm{d}E} \int_0^{\Delta\Omega} \int_{\mathrm{l.o.s.}} \rho^2 \, \mathrm{d}l \, \mathrm{d}\Omega \tag{3.9}$$

There are different models on how dark matter could interact, but gamma rays are never produced directly because of the lack of electromagnetic interaction. Instead, in the WIMP-scenario, the dark matter is expected to couple to other standard model particles through weak interaction, which then produce gamma rays in their own interactions as described in Equation 3.10.

$$\frac{\mathrm{d}\Phi}{\mathrm{d}E} \propto \frac{1}{m_{DM}^2} \sum_f \langle \sigma v \rangle_f \frac{\mathrm{d}N_\gamma^f}{dE} \tag{3.10}$$

The problem of how efficiently gamma rays are produced from dark matter is, therefore, moved to the question of how large the thermally-averaged annihilation cross-section $\langle \sigma v \rangle$ to produce standard model particles is. To avoid the dependence on specific beyond standard model physics and simplify the fitting, limits are usually calculated under the assumption of pure annihilation channels, meaning only a single type of standard model particles is produced. Then, for each assumed channel, the only free parameter is $\langle \sigma v \rangle$. To estimate the produced gamma rays through the interaction of the standard-model particles, the spectra included in `gammapy` are used, which are based on [134].

To calculate the astrophysical source term, a certain density distribution ρ of the dark matter particles has to be assumed. Modeling ρ is done under the assumption of a smooth profile with spherical symmetry that can be described analytically with few free parameters. Constraining these parameters is based on estimating the gravitational potential from X-ray or optical observations of baryonic matter that is gravitationally bound to the object. These can, for example, be stars, which are assumed to be members of the galaxy.

One of the most commonly used parametrizations is the NFW-Profile:

$$\rho(r) = \rho_s \left(\frac{r}{r_s} \right)^{-1} \left(1 + \frac{r}{r_s} \right)^{-2}, \tag{3.11}$$

[2] This is, for example, also assumed in [133].

which describes a wide range of halos with only two parameters: The normalisation ρ_s and the scale radius r_s, which describes the size of the halo. In the case of M87, the data points towards a more cored profile, meaning one that has a less steep decline in a core region around the center [135, 136, 137].

In this analysis, two models from [138, table 3] are used, that have been estimated from multiple tracer populations using a Jeans-analysis taking into account not only the stellar mass but also the central black hole. Besides a standard NFW-Profile, a generalized version of the form Equation 3.12 is used with an additional core region described by the core radius r_c and an exponent γ, where $r_c = 0$ and $\gamma = 1$ reproduce the standard NFW-Profile.

$$\rho(r) = \rho_s \frac{r_s}{r + r_c}^{\gamma} \left(1 + \frac{r}{r_s}\right)^{\gamma - 3}, \tag{3.12}$$

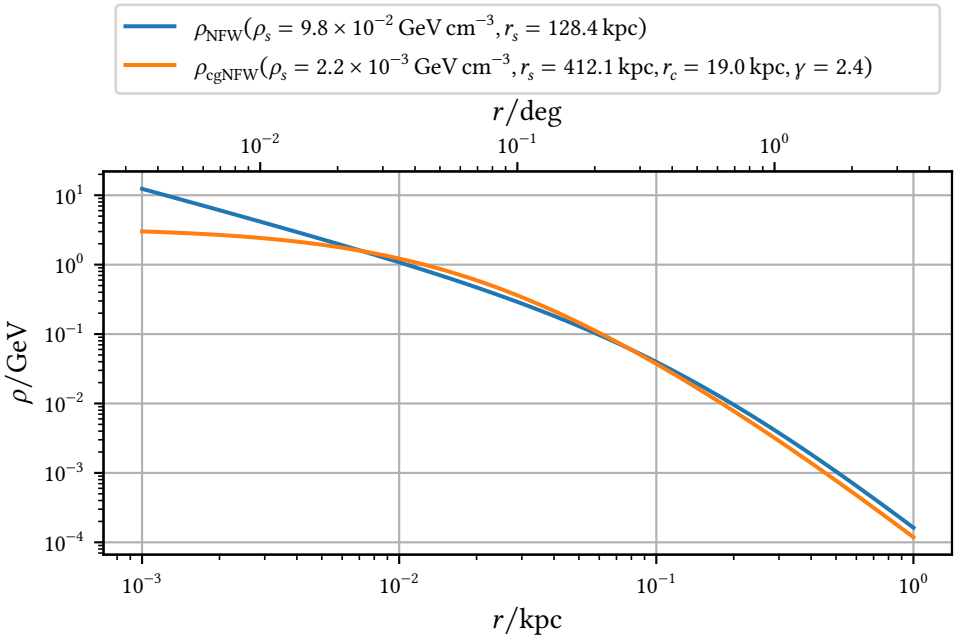

Figure 3.10: Tested dark matter profiles. Parameters from [138, table 3]. To lower radii, the density predicted by the NFW-Profile keeps on increasing, whereas the cgNFW-Profile is flat. Both models describe the observational data.

The density profiles are shown in Figure 3.10. If the dark matter distribution can indeed be reasonably approximated by a simple analytical description, it is reasonable to assume that it is centered on the supermassive black hole and not dislocated. However, the source is clearly extended and, due to the construction of the background, the excess outside of the source-region might not be as reliable as the one within. To still make confident statements about upper limits on the cross-section, the source should be mostly contained in this region, which is checked in Figure 3.11 and Figure 3.12. In all cases, the differential flux falls below 10 % within 0.1 deg and more than 50 % of the integral flux is contained. At least for the spatial models tested here, the extension is therefore rather small compared to the F.o.V..

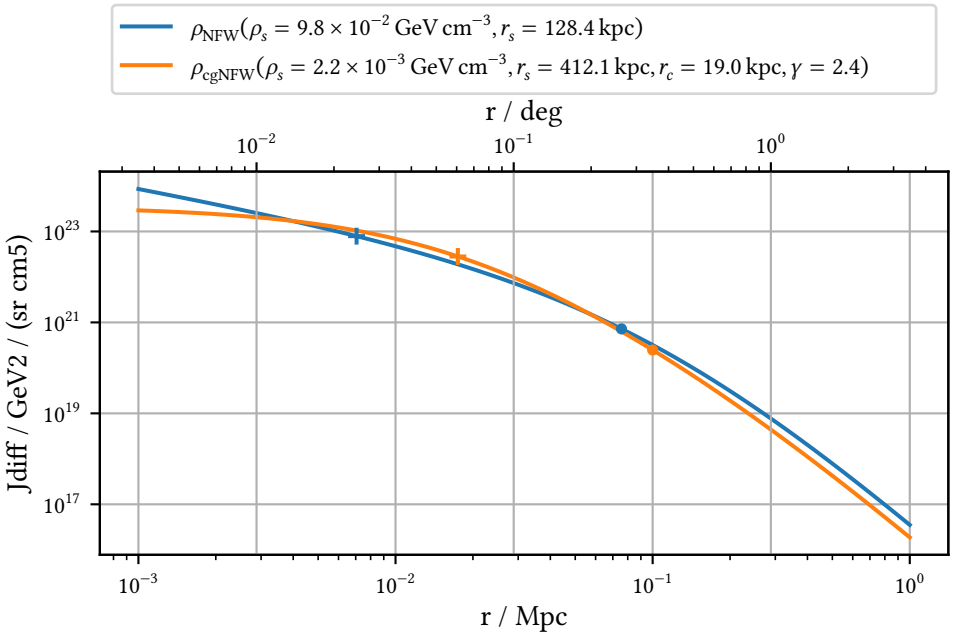

Figure 3.11: Differential J-factor for the two tested profiles. Markers show the distance at which the differential J-factor falls below 10 %/0.1 % of the maximum.

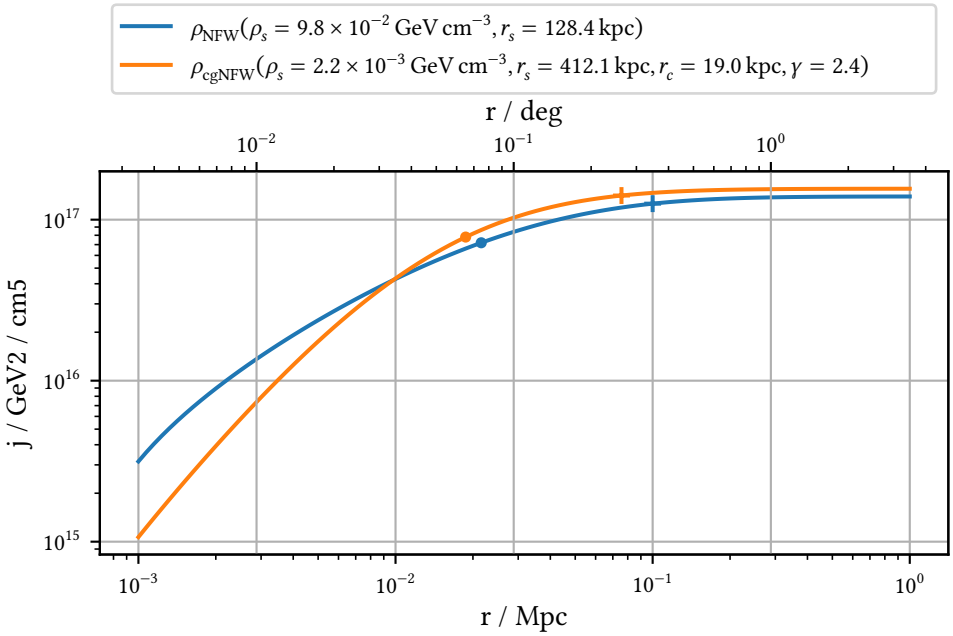

Figure 3.12: Integral J-factor for the two tested profiles. Markers show the distance at which 50 %/90 % of the total value are enclosed.

For every model, the limits are estimated at a confidence level of 95 %. In addition to the values obtained on the measured excess, the limits expected under the null-hypothesis of zero excess are calculated to get a measure of the best-case telescope performance and the expected spread of the limits due to different statistical realisations.

Instead of performing the analysis for many randomly drawn datasets, the expected limits and their spread are calculated using an Asimov dataset and the asymptotic behavior of the test statistic following [139, 140, 141]. An Asimov dataset, in this context, represents a dataset where the evaluation of operators, such as the expectation value, yields the true values for all of the parameters.

It can be shown, that in the case of a single parameter of interest, the strength parameter μ, the test statistic follows a non-central chi-squared distribution and the parameter is normally distributed with a standard deviation of σ_μ [142][3]. One can then calculate this σ_μ from the inverse covariance matrix, that can be obtained from `iminuit` on an Asimov dataset that was generated with an assumed strength parameter of zero. The $\pm N\sigma_\mu$ bands around the median expected limit then follow as:

$$\text{median} = \sigma_\mu \Phi^{-1}(1-\alpha) \tag{3.13}$$

$$\text{band}_{N\sigma_\mu} = \sigma_\mu \left(\Phi^{-1}(1-\alpha) \pm N\right) \tag{3.14}$$

with Φ the cumulative distribution function of the standard normal distribution and $\alpha = 0.95$ the confidence level.

The upper limits, that have been retrieved on the actual observations can then be compared to this expectation, which is shown in Figure 3.13 and Figure 3.14 for the two different density profiles. The main conclusions that can be drawn here, are:

Compared to existing analyses [143, 38, 144, 145], the expected limits, assuming only the background, are less constraining by one to two orders of magnitude. A limiting factor compared to analyses of Milky Way dwarf galaxies is the lower J-factor: For example, [143] assumes an integral J-factor of $1.1 \times 10^{19}\,\text{GeV}^2/\text{cm}^5$, which enters the limits linearly in the one-dimensional case. While M87 contains more mass and its halo is massive, its distance is also larger than the one to a typical satellite galaxy by around three orders of magnitude. It is also not uncommon for published limits on dark matter annihilation to include more than 100 h of data compared to the 11.12 h used here. On the analysis side, the main improvement will come with the addition of the other LSTs, which will greatly improve the reconstruction compared to the monoscopic analysis, which is unable to reach the same background rejection without the added coincidence trigger.

Second, the observed limits are incompatible with the expected distribution of upper limits. This is expected given that there was an excess measured and shows once again that the observed counts are in tension with a pure background expectation.

Lastly, the different parametrizations do not change the results substantially with the cored profile leading to slightly more constraining results.

[3] I chose to follow the conventions of the relevant statistics papers here. Beware, that both, Φ and σ already have different uses in the context of calculating the flux.

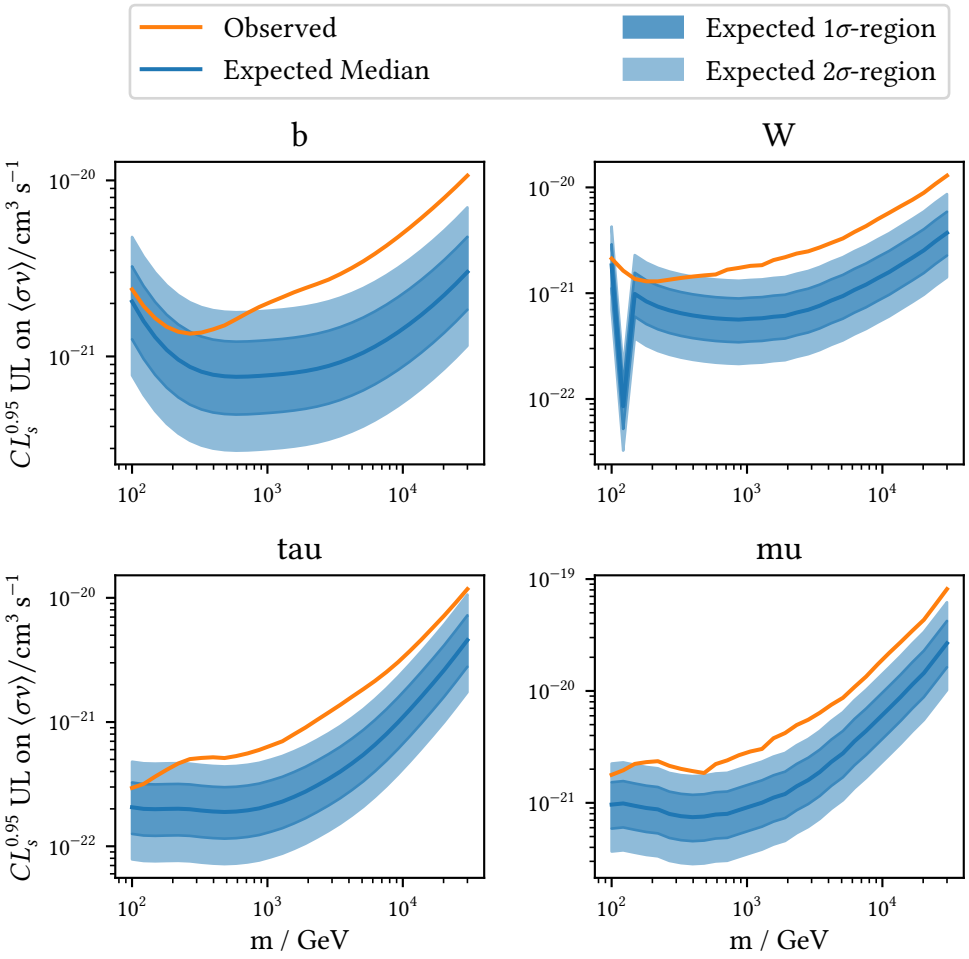

Figure 3.13: Expected and observed upper limits for the tested NFW-Profile and multiple annihilation channels. The observed limits are incompatible with a pure background expectation.

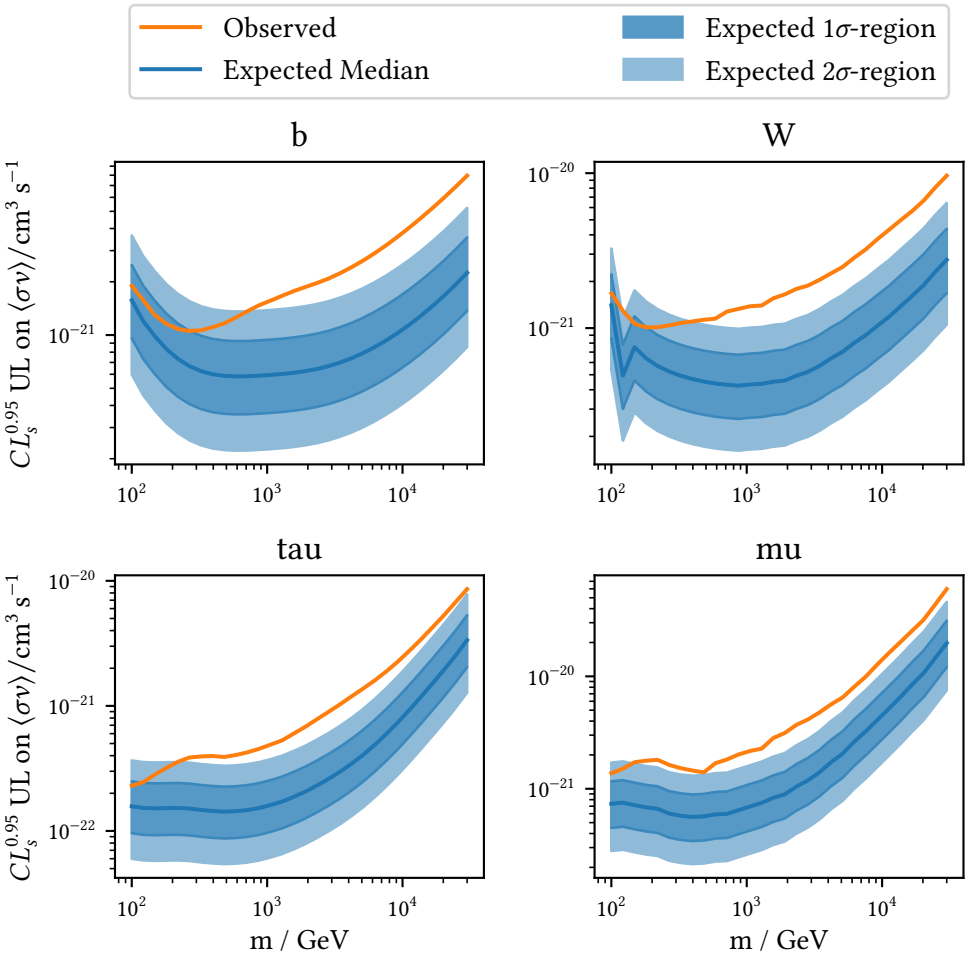

Figure 3.14: Expected and observed upper limits for the tested cgNFW-Profile and multiple annihilation channels. The observed limits are incompatible with a pure background expectation.

Chapter 4

Conclusion and Outlook

To advance the field of very-high gamma-ray astronomy, more sensitive experiments than the current generation will be needed. In the near future, this task will be fulfilled by the upcoming CTAO with its two observation sites at La Palma and in the Atacama desert of Chile.

The first telescope of the northern array, the LST-1, is already producing scientific results as part of the commissioning process. In the past years, the reliability and performance of the telescope has been constantly improved to the point that, in many aspects, the performance of the existing MAGIC telescopes can be approached with a single telescope and challenging sources are focused on.

The analysis performed in this thesis illustrates both the impressive performance LST-1 can achieve already in its current form and the limitations resulting from the current monoscopic operation. From 28.47 h of total observation time, 11.12 h of high-quality data from the radio galaxy M87 have been analyzed. This efficiency is undoubtedly lower than foreseen for the final array. On the one hand, some issues with data-taking during commissioning are expected, but on the other hand, IACTs always rely on good weather and a clear sky. Here, LST-1 suffers from the limited availability of simulations to describe different atmospheric properties. In general, the way simulations, model training, and the calculation of IRF-components are handled is not optimal, with only a few select declination lines simulated. For most sources, this currently leads to the case shown in Figure 2.17, where the observations are systematically offset from the simulations. On top of that, the existence of a second, different grid for evaluating of point-like IRF-components is an active topic of discussion.

Analyzing the observed data, the count maps show a small overfluctuation from the source region. The measured excess from the assumed source position is consistent with the assumption that the source was in a low-state in the observed timeframe but is not significant enough to claim a detection of the source yet. A limiting factor certainly is the high amount of issues during observations, leaving less than half of the data for the analysis. Since the source has been observed by other experiments in the past, LST-1 is continuing to observe the source and will likely be able to claim a detection at some point.

From the observations, a three-dimensional background model was constructed to compute significance maps and test dark-matter annihilation models. The low-energy shape of the background acceptance was found to deviate significantly from the assumption of radial symmetry, showing that, even for a single telescope, more general parametrizations are beneficial. Currently, the data format can describe three-dimensional background models, but not any IRF-components such as the effective area A_{eff}. The effect on the IRF-components and possible parametrizations is currently a high-priority topic for CTAO and `gammapy`, and will become

even more relevant once multiple telescopes are observing.

Another problem highlighted during the background modeling is the importance of strong directional reconstruction: For a single-source observation as performed here, the main issue arises from the limited maximum size of the source exclusion due to the small wobble-distance that LST-1 chose to use. In future sky surveys, multiple regions will need to be excluded depending on the observed portion of the sky. Having large exclusion regions makes getting complete coverage in the F.o.V. a challenging task. Analytic descriptions of the telescope acceptance would relax the requirements on the amount of background data, but so far they have not been able to properly describe the energy-dependent shape of the acceptance.

The directional reconstruction will certainly improve a lot once the other LSTs, which are currently under construction, are operational and the array can observe in a stereoscopic setup. With these, CTAO is expected to finally significantly outperform the current generation of experiments. Getting all telescopes operational will require significant efforts on the software and simulation side: While it is not a problem to analyze stereoscopic data in `ctapipe`, the development of LST-specific code still largely happens in `lstchain`, which uses its own datamodel. First tests to produce LST-1 data directly from CTAO software have already been performed, but more work will be needed to ensure the smooth operation of the whole array.

Bibliography

1. I. Neutelings. *Electromagnetic spectrum*. 2024.
   https://tikz.net/electromagnetic_spectrum/
2. A. Povel. *How to create a electromagnetic spectrum using pgfplots package (together with colormaps)*. 2024.
   https://tex.stackexchange.com/questions/348491/
3. H. J. Walker. "A brief history of infrared astronomy". *Astronomy and Geophysics* 41:5, 2000, pages 5.10–5.13. ISSN: 1366-8781.
   DOI: 10.1046/j.1468-4004.2000.41510.x
4. J. C. Maxwell. "VIII. A dynamical theory of the electromagnetic field". *Philosophical transactions of the Royal Society of London* 155, 1865, pages 459–512.
   DOI: 10.1098/rstl.1865.0008
5. V. F. Hess. "Über Beobachtungen der durchdringenden Strahlung bei sieben Freiballonfahrten". *Z. Phys.* 13, 1912, page 1084.
   https://cds.cern.ch/record/262750
6. Nobel Prize Outreach AB. *The Nobel Prize in Physics 1936*. 2024.
   https://www.nobelprize.org/prizes/physics/1936/summary/
7. W. T. Sullivan. "Karl Jansky and the discovery of extraterrestrial radio waves". In: *The Early Years of Radio Astronomy: Reflections Fifty Years after Jansky's Discovery*. Cambridge University Press, 1984, pages 3–42.
   https://ui.adsabs.harvard.edu/abs/1984eyra.book....3S
8. C. Keller. "X-rays from the Sun". *Experientia* 51, 1995, pages 710–720.
   DOI: 10.1007/BF01941268
9. W. L. Kraushaar and G. W. Clark. "Search for Primary Cosmic Gamma Rays with the Satellite Explorer XI". *Phys. Rev. Lett.* 8, 3 1962, pages 106–109.
   DOI: 10.1103/PhysRevLett.8.106
10. T. A. Prince, J. C. Ling, W. A. Mahoney, G. R. Riegler, and A. S. Jacobson. "A high-resolution measurement of the 2.223 MeV neutron capture line in a solar flare". *Astrophysical Journal, Letters to the Editor* 255, 1982, pages L81–L84.
    DOI: 10.1086/183773

11. The Fermi-LAT collaboration, J. Ballet, P. Bruel, T. H. Burnett, and B. Lott. "Fermi Large Area Telescope Fourth Source Catalog Data Release 4 (4FGL-DR4)". *CoRR*, 2023.
DOI: 10.48550/arXiv.2307.12546

12. T. Weekes et al. "Observation of TeV Gamma-rays from the Crab Nebula using the Atmospheric Cherenkov Imaging Technique". *Astrophysical Journal* 342, 1989, pages 379–395.
DOI: 10.1086/167599

13. R. L. Workman et al. "Review of Particle Physics". *PTEP* 2022, 2022, page 083C01.
DOI: 10.1093/ptep/ptac097

14. A. Knierim. *Multi-Messenger Milky Way*. 2024.
https://github.com/aknierim/multi_messenger_milky_way/

15. P. M. W. Kalberla et al. "The Leiden/Argentine/Bonn (LAB) Survey of Galactic HI - Final data release of the combined LDS and IAR surveys with improved stray-radiation corrections". *A&A* 440:2, 2005, pages 775–782.
DOI: 10.1051/0004-6361:20041864

16. K. Land and A. Slosar. "Correlation between galactic HI and the cosmic microwave background". *Physical Review D* 76:8, 2007. ISSN: 1550-2368.
DOI: 10.1103/physrevd.76.087301

17. M. Remazeilles, C. Dickinson, A. Banday, M.-A. Bigot-Sazy, and T. Ghosh. "An improved source-subtracted and destriped 408-MHz all-sky map". *Monthly Notices of the Royal Astronomical Society* 451:4, 2015, pages 4311–4327.
DOI: 10.1093/mnras/stv1274

18. E. Carretti et al. "S-band Polarization All-Sky Survey (S-PASS): survey description and maps". *Monthly Notices of the Royal Astronomical Society* 489:2, 2019, pages 2330–2354. ISSN: 1365-2966.
DOI: 10.1093/mnras/stz806

19. W. Reich, E. Fürst, C. Haslam, P. Steffen, and K. Reif. "A radio continuum survey of the Galactic Plane at 11 CM wavelength. I-The area L= 357.4 to 76 deg, B=-1.5 to+ 1.5 deg". *Astronomy and Astrophysics Supplement Series* 58, 1984, pages 197–199.
https://ui.adsabs.harvard.edu/abs/1984A&AS...58..197R

20. W. Reich, E. Fürst, P. Reich, and K. Reif. "A radio continuum survey of the Galactic Plane at 11 CM wavelength. II-The area L= 358-76 deg, B=-5 to 5 deg. III". *Astronomy and Astrophysics Supplement Series* 85, 1990, pages 633–690.
https://ui.adsabs.harvard.edu/abs/1990A&AS...85..633R

21. E. Fürst, W. Reich, P. Reich, and K. Reif. "A Radio Continuum Survey of the Galactic Plane at 11-CENTIMETER Wavelength-Part Three-the Area 76DEG< L< 240DEG". *Astronomy and Astrophysics Supplement* 85, 1990, page 691.
https://ui.adsabs.harvard.edu/abs/1990A&AS...85..691F

22. T. M. Dame, D. Hartmann, and P. Thaddeus. "The Milky Way in Molecular Clouds: A New Complete CO Survey". *Astrophysical Journal* 547:2, 2001, pages 792–813.
DOI: 10.1086/318388

23. M.-A. Miville-Deschênes and G. Lagache. "IRIS: A New Generation of IRAS Maps". *Astrophysical Journal, Supplement Series* 157:2, 2005, pages 302–323.
DOI: 10.1086/427938

24. M. G. Hauser et al. "The COBE diffuse infrared background experiment search for the cosmic infrared background. I. Limits and detections". *The Astrophysical Journal* 508:1, 1998, page 25.
DOI: 10.1086/306379

25. T. Kelsall et al. "The COBE diffuse infrared background experiment search for the cosmic infrared background. II. Model of the interplanetary dust cloud". *The Astrophysical Journal* 508:1, 1998, page 44.
DOI: 10.1086/306380

26. R. Arendt et al. "The COBE diffuse infrared background experiment search for the cosmic infrared background. III. Separation of galactic emission from the infrared sky brightness". *The Astrophysical Journal* 508:1, 1998, page 74.
DOI: 10.1086/306381

27. E. Dwek et al. "The COBE diffuse infrared background experiment search for the cosmic infrared background. IV. Cosmological implications". *The Astrophysical Journal* 508:1, 1998, page 106.
DOI: 10.1086/306382

28. D. P. Finkbeiner. "A Full-Sky Hα Template for Microwave Foreground Prediction". *Astrophysical Journal, Supplement Series* 146:2, 2003, pages 407–415.
DOI: 10.1086/374411

29. ESA and DPAC. *Multi-Messenger Milky Way*. 2024.
https://sci.esa.int/web/gaia/-/60196-gaia-s-sky-in-colour-equirectangular-projection

30. S. L. Snowden et al. "ROSAT Survey Diffuse X-Ray Background Maps. II." *Astrophysical Journal* 485:1, 1997, pages 125–135.
DOI: 10.1086/304399

31. Fermi LAT Collaboration. *LAT Data Products - Weekly Photon Files*. 2024.
https://heasarc.gsfc.nasa.gov/FTP/fermi/data/lat/weekly/photon/

32. W. Atwood et al. "The large area telescope on the Fermi gamma-ray space telescope mission". *The Astrophysical Journal* 697:2, 2009, page 1071.
DOI: 10.1088/0004-637X/697/2/1071

33. IceCube Collaboration et al. "Observation of high-energy neutrinos from the Galactic plane". *Science* 380:6652, 2023, pages 1338–1343.
DOI: 10.1126/science.adc9818

34. D. Caprioli. "Particle Acceleration At Shocks: an Introduction". *CoRR*, 2023.
DOI: 10.48550/arXiv.2307.00284

35. M. Kachelriess. “Lecture Notes on High Energy Cosmic Rays”. *CoRR*, 2008.
DOI: 10.48550/arXiv.0801.4376

36. A. R. Bell. “The acceleration of cosmic rays in shock fronts - I.” *Monthly Notices of the Royal Astronomical Society* 182, 1978, pages 147–156.
DOI: 10.1093/mnras/182.2.147

37. J. Larmor. “IX. A dynamical theory of the electric and luminiferous medium.—Part III. Relations with material media”. *Philosophical Transactions of the Royal Society of London. Series A, Containing Papers of a Mathematical or Physical Character* 190, 1897, pages 205–300.
https://royalsocietypublishing.org/doi/pdf/10.1098/rsta.1897.0020

38. M. L. Ahnen et al. “Limits to dark matter annihilation cross-section from a combined analysis of MAGIC and Fermi-LAT observations of dwarf satellite galaxies”, 2016.
DOI: 10.1088/1475-7516/2016/02/039

39. V. Acciari et al. “Constraining Dark Matter Lifetime With a Deep Gamma-Ray Survey of the Perseus Galaxy Cluster With Magic”. *Physics of the Dark Universe* 22, 2018, pages 38–47.
DOI: 10.1016/j.dark.2018.08.002

40. A. Boyarsky, D. Malyshev, and O. Ruchayskiy. “A comment on the emission from the Galactic Center as seen by the Fermi telescope”. *Physics Letters B* 705:3, 2011, pages 165–169.
DOI: 10.1016/j.physletb.2011.10.014

41. M. Ackermann et al. “The Fermi galactic center GeV excess and implications for dark matter”. *The Astrophysical Journal* 840:1, 2017, page 43.
DOI: 10.3847/1538-4357/aa6cab

42. F. Calore, I. Cholis, C. McCabe, and C. Weniger. *Physical Review D* 91:6, 2015, page 063003.
DOI: 10.1103/PhysRevD.91.063003

43. O. Macías-Ramírez, C. Gordon, A. M. Brown, and J. Adams. “Evaluating the gamma-ray evidence for self-annihilating dark matter from the Virgo cluster”. *Phys. Rev. D* 86, 7 2012, page 076004.
DOI: 10.1103/PhysRevD.86.076004

44. M. Volonteri, M. Habouzit, and M. Colpi. “The origins of massive black holes”. *Nature Reviews Physics* 3:11, 2021, pages 732–743

45. H. Netzer. “Revisiting the unified model of active galactic nuclei”. *Annual Review of Astronomy and Astrophysics* 53, 2015, pages 365–408.
DOI: 10.1146/annurev-astro-082214-122302

46. F. Aharonian et al. “Is the giant radio galaxy M87 a TeV gamma-ray emitter?” *A&A* 403:1, 2003, pages L1–L5.
DOI: 10.1051/0004-6361:20030372

47. *NRAO’s Baseline Episode 3: Viewing Active Galaxies*. 2024.
https://public.nrao.edu/news/key-feature-powerful-radio-galaxies/ visited on 2024-02-16

48. The Pierre Auger Collaboration et al. “Observation of a large-scale anisotropy in the arrival directions of cosmic rays above 8×10^{18} eV”. *Science* 357:6357, 2017, pages 1266–1270.
DOI: 10.1126/science.aan4338

49. C. Messier, H. Frommert, and C. Kronberg. “Catalog of Nebulae and Star Clusters”. *Connoissance des Temps*, 1784.
http://www.messier.seds.org/xtra/history/m-cat81.html

50. E. P. Hubble. “Extragalactic nebulae”. *Astrophysical Journal* 64, 1926, pages 321–369.
DOI: 10.1086/143018

51. O. G. Kashibadze, I. D. Karachentsev, and V. E. Karachentseva. “Structure and kinematics of the Virgo cluster of galaxies”. *A&A* 635, 2020, A135.
DOI: 10.1051/0004-6361/201936172

52. R. de Grijs and G. Bono. “Clustering of Local Group Distances: Publication Bias or Correlated Measurements? VI. Extending to Virgo Cluster Distances”. *The Astrophysical Journal Supplement Series* 246:1, 2019. ISSN: 1538-4365.
DOI: 10.3847/1538-4365/ab5711

53. G. J. Stanley and O. B. Slee. “Galactic Radiation at Radio Frequencies. II. The Discrete Sources”. *Australian Journal of Scientific Research A Physical Sciences* 3, 1950, page 234.
DOI: 10.1071/CH9500234

54. F. N. Owen, J. A. Eilek, and N. E. Kassim. “M87 at 90 Centimeters: A Different Picture”. *The Astrophysical Journal* 543:2, 2000, pages 611–619.
DOI: 10.1086/317151

55. EHT Collaboration et al. “First M87 event horizon telescope results. IV. Imaging the central supermassive black hole”. *arXiv preprint arXiv:1906.11241*, 2019.
DOI: 10.3847/2041-8213/ab0e85

56. E. Byram, T. Chubb, and H. Friedman. “Cosmic X-ray sources, galactic and extragalactic”. *Science* 152:3718, 1966, pages 66–71.
DOI: 10.1126/science.152.3718.66

57. H. L. Marshall et al. “A High-Resolution X-Ray Image of the Jet in M87”. *The Astrophysical Journal* 564:2, 2002, page 683.
DOI: 10.1086/324396

58. ESO and EHT Collaboration. *A view of the M87 supermassive black hole in polarised light.* 2024.
https://www.eso.org/public/images/eso2105a/

59. F. Aharonian et al. “Fast Variability of Tera-Electron Volt γ Rays from the Radio Galaxy M87”. *Science* 314:5804, 2006, pages 1424–1427.
DOI: 10.1126/science.1134408

60. V. Acciari et al. “Observation of Gamma-Ray Emission from the Galaxy M87 above 250 GeV with VERITAS*”. *The Astrophysical Journal* 679:1, 2008, page 397.
DOI: 10.1086/587458

61. A. A. Abdo et al. “Fermi Large Area Telescope gamma-ray detection of the radio galaxy M87”. *The Astrophysical Journal* 707:1, 2009, page 55.
DOI: 10.1088/0004-637X/707/1/55

62. MAGIC Collaboration et al. “Monitoring of the radio galaxy M 87 during a low-emission state from 2012 to 2015 with MAGIC”. *Monthly Notices of the Royal Astronomical Society* 492:4, 2020, pages 5354–5365.
DOI: 10.1093/mnras/staa014

63. P. Charlot et al. “The third realization of the International Celestial Reference Frame by very long baseline interferometry”. *A&A* 644, 2020, A159.
DOI: 10.1051/0004-6361/202038368

64. F. Schmidt and Karlsruhe Institute of Technology. *CORSIKA – an Air Shower Simulation Program*. 2024.
https://www.iap.kit.edu/corsika/

65. H. J. Bhabha and W. Heitler. “The passage of fast electrons and the theory of cosmic showers”. *Proceedings of the Royal Society of London. Series A-Mathematical and Physical Sciences* 159:898, 1937, pages 432–458.
DOI: 10.1098/rspa.1937.0082

66. K. Bernlöhr. “Impact of atmospheric parameters on the atmospheric Cherenkov technique”. *Astroparticle Physics* 12:4, 2000, pages 255–268.
DOI: https://doi.org/10.1016/S0927-6505(99)00093-6

67. A. Abeysekara et al. “The High-Altitude Water Cherenkov (HAWC) observatory in México: The primary detector”. *Nuclear Instruments and Methods in Physics Research Section A: Accelerators, Spectrometers, Detectors and Associated Equipment* 1052, 2023, page 168253.
DOI: 10.1016/j.nima.2023.168253

68. P. A. Čerenkov. “Visible Radiation Produced by Electrons Moving in a Medium with Velocities Exceeding that of Light”. *Phys. Rev.* 52, 4 1937, pages 378–379.
DOI: 10.1103/PhysRev.52.378

69. A. Curcio et al. “Electro-Optical Detection of Coherent Radiation Induced by Relativistic Electron Bunches in the Near and Far Fields”. *Physical Review Applied* 9, 2018.
DOI: 10.1103/PhysRevApplied.9.024004

70. K. Bernlöhr. “Simulation of imaging atmospheric Cherenkov telescopes with CORSIKA and sim_telarray”. *Astroparticle Physics* 30:3, 2008, pages 149–158. ISSN: 0927-6505.
DOI: https://doi.org/10.1016/j.astropartphys.2008.07.009

71. I. Frank and I. Tamm. “Coherent Visible Radiation of Fast Electrons Passing Through Matter”. In: *Selected Papers*. Ed. by B. M. ”Bolotovskii, V. Y. Frenkel, and R. Peierls. Springer Berlin Heidelberg, Berlin, Heidelberg, 1991, pages 29–35.
DOI: 10.1007/978-3-642-74626-0_2

72. CTA Consortium. “Design concepts for the Cherenkov Telescope Array CTA: an advanced facility for ground-based high-energy gamma-ray astronomy”. *Experimental Astronomy* 32, 2011, pages 193–316.
DOI: 10.1007/s10686-011-9247-0

73. J. Cortina and M. Teshima. “Status of the Cherenkov Telescope Array’s Large Size Telescopes”. *CoRR*, 2015.
ARXIV: 1508.06438 [astro-ph.IM]

74. J. M. Davies and E. S. Cotton. “Design of the quartermaster solar furnace”. *Solar Energy* 1:2, 1957, pages 16–22. ISSN: 0038-092X.
DOI: 10.1016/0038-092X(57)90116-0

75. K. Schwarzschild. *Untersuchungen zur geometrischen optik...* Vol. 1. Weidmann, 1905.
https://wp.optics.arizona.edu/jsasian/wp-content/uploads/sites/33/2016/02/Schwarzschild-II.pdf

76. A. Couder. “Sur un type nouveau de télescope photographique”. *Comptes Rendus* 183:45, 1926, pages 1276–1279

77. R. Lessard, J. Buckley, V. Connaughton, and S. Le Bohec. “A new analysis method for reconstructing the arrival direction of TeV gamma rays using a single imaging atmospheric Cherenkov telescope”. *Astroparticle Physics* 15:1, 2001, pages 1–18. ISSN: 0927-6505.
DOI: https://doi.org/10.1016/S0927-6505(00)00133-X

78. CTA Observatory and CTA Consortium. *CTAO Instrument Response Functions - prod5 version v0.1*. Version v0.1. Zenodo, 2021.
DOI: 10.5281/zenodo.5499840

79. CTA-LST Project. “Observations of the Crab Nebula and Pulsar With the Large-Sized Telescope Prototype of the Cherenkov Telescope Array”. *CoRR*, 2023.
DOI: 10.48550/arXiv.2306.12960

80. J. Cortina (for the CTAO LST collaboration Collaboration). “First detection of VHE gamma-ray emission from FSRQ OP 313 with LST-1”. *The Astronomer’s Telegram* 16381, 2023, page 1.
https://www.astronomerstelegram.org/?read=16381

81. K. Kosack et al. *Top-level Data Model Specification*. Technical report. 2024.
Note: Internal document of CTAO

82. R. Lopez-Coto et al. *cta-observatory/cta-lstchain: v0.10.7 - 2024-02-01*. Version v0.10.7. 2024.
DOI: 10.5281/zenodo.10604579

83. R. López-Coto et al. (for the CTA LST Project Collaboration). “Physics Performance of the Large Size Telescope prototype of the Cherenkov Telescope Array”. In: *Proceedings, 37th International Cosmic Ray Conference*. Vol. 395. Berlin, Germany, 2021, page 806.
DOI: 10.22323/1.395.0806

84. C. R. Harris et al. “Array programming with NumPy”. *Nature* 585:7825, 2020, pages 357–362.
DOI: 10.1038/s41586-020-2649-2

85. P. Virtanen et al. “SciPy 1.0: Fundamental Algorithms for Scientific Computing in Python”. *Nature Methods* 17, 2020, pages 261–272.
DOI: 10.1038/s41592-019-0686-2

86. F. Pedregosa et al. “Scikit-learn: Machine Learning in Python”. *Journal of Machine Learning Research* 12, 2011, pages 2825–2830.
https://www.jmlr.org/papers/volume12/pedregosa11a/pedregosa11a.pdf?ref=https:/

87. The pandas development team. *pandas-dev/pandas: Pandas*. 2020.
DOI: 10.5281/zenodo.3509134

88. J. D. Hunter. “Matplotlib: A 2D graphics environment”. *Computing in Science & Engineering* 9:3, 2007, pages 90–95.
DOI: 10.1109/MCSE.2007.55

89. B. Khélifi et al. “Gammapy: Present Status and Future Roadmap”. *CoRR*, 2023.
ARXIV: 2308.13389 [astro-ph.IM]

90. M. Linhoff et al. *cta-observatory/pyirf: v0.8.1 – 2023-03-16*. Version v0.8.1. 2023.
DOI: 10.5281/zenodo.7741289

91. Astropy Collaboration. “The Astropy Project: Sustaining and Growing a Community-oriented Open-source Project and the Latest Major Release (v5.0) of the Core Package”. *The Astrophysical Journal* 935:2, 167, 2022, page 167.
DOI: 10.3847/1538-4357/ac7c74

92. M. Linhoff et al. (for the CTA Consortium and Observatory Collaboration). “ctapipe – Prototype Open Event Reconstruction Pipeline for the Cherenkov Telescope Array”. In: *Proceedings, 38th International Cosmic Ray Conference*. Vol. 444. 703. Nagoya, Japan, 2023.
DOI: 10.22323/1.444.0703

93. C. Nigro, T. Hassan, and L. Olivera-Nieto. *Evolution of Data Formats in Very-High-Energy Gamma-ray Astronomy*. 2021.
ARXIV: 2109.14661 [astro-ph.IM]

94. R. Orito, et al, for the CTA Consortium. “Development of PMT Clusters for CTA-LST Camera”. In: *Proceedings, 32th International Cosmic Ray Conference*. Beijing, China, 2011.
DOI: 10.7529/ICRC2011/V09/1091

95. A. Sanuy et al. “Wideband (500 MHz) 16 bit dynamic range current mode PreAmplifier for the CTA cameras (PACTA)”. *Journal of Instrumentation* 7:01, 2012, page C01100.
DOI: 10.1088/1748-0221/7/01/C01100

96. A. Okumura et al. “Prototyping hexagonal light concentrators using high-reflectance specular films for the large-sized telescopes of the Cherenkov Telescope Array”. *Journal of Instrumentation* 12:12, 2017. ISSN: 1748-0221.
DOI: 10.1088/1748-0221/12/12/p12008

97. S. Masuda et al. “Development of the Photomultiplier Tube Readout System for the First Large-Sized Telescope of the Cherenkov Telescope Array”. *CoRR*, 2015.
ARXIV: 1509.00548 [astro-ph.IM]

98. J. Adam et al. "The MEG detector for μ +⟶e+ γ decay search". *The European Physical Journal C* 73:4, 2013. ISSN: 1434-6052.
DOI: 10.1140/epjc/s10052-013-2365-2

99. Paul Scherrer Institut. *DRS4 datasheet*.
https://www.psi.ch/en/drs visited on 2024-02-13

100. J. Aleksić et al. "The major upgrade of the MAGIC telescopes, Part I: The hardware improvements and the commissioning of the system". *Astroparticle Physics* 72, 2016, pages 61–75. ISSN: 0927-6505.
DOI: https://doi.org/10.1016/j.astropartphys.2015.04.004

101. L. A. Tejedor et al. "An Analog Trigger System for Atmospheric Cherenkov Telescope Arrays". *IEEE Transactions on Nuclear Science* 60:3, 2013, pages 2367–2375.
DOI: 10.1109/TNS.2013.2257852

102. P. Peñil, L. Á. Tejedor, J. A. Barrio, and M. López. "A Trigger Interface Board To Manage Trigger and Timing Signals in Cta Large-Sized Telescope and Medium-Sized Telescope Cameras". *CoRR*, 2017.
ARXIV: 1709.04692 [astro-ph.IM]

103. T. Saito et al. "Commissioning of the camera of the first Large Size Telescope of the Cherenkov Telescope Array". In: *Proceedings of 37th International Cosmic Ray Conference — PoS(ICRC2021)*. ICRC2021. Sissa Medialab, 2021.
DOI: 10.22323/1.395.0718

104. D. Hadasch et al. "Development of Slow Control Boards for the Large Size Telescopes of the Cherenkov Telescope Array". *CoRR*, 2015.
ARXIV: 1509.01364 [astro-ph.IM]

105. P. Gliwny et al. *Low-level correction procedures for DRS4*. Technical report. 2024.
Note: Internal document of CTAO/LST

106. M. Jacquemont et al. "GammaLearn: a Deep Learning framework for IACT data". In: *36th International Cosmic Ray Conference*. Vol. ICRC2019. Madison, United States, 2019, page 705.
https://hal.science/hal-02197399

107. D. Nieto et al. *CTLearn: Deep Learning for Gamma-ray Astronomy*. 2019.
ARXIV: 1912.09877 [astro-ph.IM]

108. A. M. Hillas. "Cerenkov Light Images of EAS Produced by Primary Gamma Rays and by Nuclei". In: *19th International Cosmic Ray Conference (ICRC19), Volume 3*. Vol. 3. International Cosmic Ray Conference. 1985, page 445.
https://ntrs.nasa.gov/api/citations/19850026666/downloads/19850026666.pdf

109. *SLURM Workload Manager*.
https://slurm.schedmd.com/ visited on 2024-02-22

110. M. Ahnen et al. "Performance of the MAGIC telescopes under moonlight". *Astroparticle Physics* 94, 2017, pages 29–41. ISSN: 0927-6505.
DOI: https://doi.org/10.1016/j.astropartphys.2017.08.001

111. T. Bretz. “Zenith angle dependence of the cosmic ray rate as measured with imaging air-Cherenkov telescopes”. *Astroparticle Physics* 111, 2019, pages 72–86. ISSN: 0927-6505. DOI: 10.1016/j.astropartphys.2019.02.004

112. D. Heck, J. Knapp, J. Capdevielle, G. Schatz, T. Thouw, et al. “CORSIKA: A Monte Carlo code to simulate extensive air showers”. *Report fzka* 6019:11, 1998. DOI: 10.5445/IR/270043064

113. E. Garcia, T. Vuillaume, and L. Nickel. *The lstMCpipe library*. 2022. DOI: 10.48550/arXiv.2212.00120

114. H. Laurent and R. L. Rivest. “Constructing optimal binary decision trees is NP-complete”. *Information processing letters* 5:1, 1976, pages 15–17. http://people.csail.mit.edu/rivest/pubs/HR76.pdf

115. L. Breiman. “Random forests”. *Machine learning* 45, 2001, pages 5–32. DOI: 10.1023/A:1010933404324

116. A. Fattorini. “Hadronic accelerators in the universe”. PhD thesis. TU Dortmund, 2023. DOI: 10.17877/DE290R-24027

117. R. M. Dominik, M. Linhoff, and J. Sitarek. “Interpolation of Instrument Response Functions for the Cherenkov Telescope Array in the Context of pyirf”. *arXiv preprint arXiv:2309.16488*, 2023

118. C. Deil et al. *Data formats for gamma-ray astronomy - version 0.3*. 2022. DOI: 10.5281/zenodo.7304668

119. T.-P. Li and Y. Ma. “Analysis methods for results in gamma-ray astronomy”. *The Astrophysical Journal* 272, 1983, pages 317–324. DOI: 10.1086/161295

120. I. Vovk, M. Strzys, and C. Fruck. “Spatial likelihood analysis for MAGIC telescope data”. *Astronomy & Astrophysics* 619, 2018, A7. DOI: 10.1051/0004-6361/201833139

121. S. Mender. “Spectral and spatial analysis of MAGIC telescope data in a standardized format”. PhD thesis. Technische Universität Dortmund, Fakultät Physik, 2023. DOI: 10.17877/DE290R-24082

122. L. Mohrmann et al. “Validation of open-source science tools and background model construction in γ-ray astronomy”. *A&A* 632, 2019, A72. DOI: 10.1051/0004-6361/201936452

123. M. C. Strzys et al. “Pybkgmodel-a background modelling toolbox for the CTA”. In: *38th International Cosmic Ray Conference*. 2023, pages 1–17. DOI: 10.3929/ethz-b-000653302

124. M. de Bony and G. Emery. *acceptance_modelisation*. 2024. https://github.com/mdebony/acceptance_modelisation

125. W. Cash. “Parameter estimation in astronomy through application of the likelihood ratio”. *Astrophysical Journal* 228, 1979, pages 939–947. https://adsabs.harvard.edu/full/1979ApJ...228..939C

126. F. James and M. Roos. "Minuit: A System for Function Minimization and Analysis of the Parameter Errors and Correlations". *Comput. Phys. Commun.* 10, 1975, pages 343–367.
DOI: 10.1016/0010-4655(75)90039-9

127. H. Dembinski et al. *scikit-hep/iminuit*. Version v2.25.2. 2024.
DOI: 10.5281/zenodo.10638795

128. J. Aleksić et al. "MAGIC observations of the giant radio galaxy M 87 in a low-emission state between 2005 and 2007". *Astronomy & astrophysics* 544, 2012, A96.
DOI: 10.1051/0004-6361/201117827

129. J. Albert et al. "Very high energy gamma-ray observations of strong flaring activity in M87 in 2008 February". *The Astrophysical Journal* 685:1, 2008, page L23.
DOI: 10.1086/592348

130. E. Aliu et al. "VERITAS observations of day-scale flaring of M87 in 2010 april". *The Astrophysical Journal* 746:2, 2012, page 141.
DOI: 10.1088/0004-637X/746/2/141

131. S. Saxena, A. Summa, D. Elsässer, M. Rüger, and K. Mannheim. "Constraints on dark matter annihilation from M87: Signatures of prompt and inverse-Compton gamma rays". *The European Physical Journal C* 71, 2011, pages 1–5.
DOI: 10.1140/epjc/s10052-011-1815-y

132. F. M. Rieger and F. Aharonian. "Probing the central black hole in M87 with gamma-rays". *Modern Physics Letters A* 27:28, 2012. ISSN: 1793-6632.
DOI: 10.1142/s0217732312300303

133. K. Christy, J. Kumar, and P. Sandick. "Constraining p-wave dark matter annihilation with gamma-ray observations of M87". *Physical Review D* 108:10, 2023, page 103042.
DOI: 10.1103/PhysRevD.108.103042

134. M. Cirelli et al. "Pppc 4 Dm Id: a Poor Particle Physicist Cookbook for Dark Matter Indirect Detection". *Journal of Cosmology and Astroparticle Physics* 2011:03, 2011, pages 051–051.
DOI: 10.1088/1475-7516/2011/03/051

135. J. D. Murphy, K. Gebhardt, and J. J. Adams. "GALAXY KINEMATICS WITH VIRUS-P: THE DARK MATTER HALO OF M87". *The Astrophysical Journal* 729:2, 2011, page 129.
DOI: 10.1088/0004-637X/729/2/129

136. R. Ruffini, C. R. Argüelles, and J. A. Rueda. "On the core-halo distribution of dark matter in galaxies". *Monthly Notices of the Royal Astronomical Society* 451:1, 2015, pages 622–628. ISSN: 0035-8711.
DOI: 10.1093/mnras/stv1016

137. D. H. Weinberg, J. S. Bullock, F. Governato, R. K. de Naray, and A. H. G. Peter. "Cold dark matter: Controversies on small scales". *Proceedings of the National Academy of Sciences* 112:40, 2015, pages 12249–12255.
DOI: 10.1073/pnas.1308716112

138. L. J. Oldham and M. W. Auger. “Galaxy structure from multiple tracers – II. M87 from parsec to megaparsec scales”. *Monthly Notices of the Royal Astronomical Society* 457:1, 2016, pages 421–439. ISSN: 0035-8711.
DOI: 10.1093/mnras/stv2982

139. S. Fröse. *asympTotic lIkelihood-based Tests for daRk mAtTer sEarch*. 2023.
https://github.com/StFroese/TITRATE/tree/main.
Note: The title is correct. The author really wanted to make an ”acronym” (titrate) work in the most disgusting way.

140. G. Cowan, K. Cranmer, E. Gross, and O. Vitells. “Asymptotic Formulae for Likelihood-Based Tests of New Physics”. *The European Physical Journal C* 71:2, 2011, page 1554.
DOI: 10.1140/epjc/s10052-011-1554-0

141. M. Rieger. “Search for Higgs boson production in association with top quarks and decaying into bottom quarks using deep learning techniques with the CMS experiment”. PhD thesis. RWTH Aaachen University, 2019.
DOI: 10.18154/RWTH-2019-06415

142. A. Wald. “Tests of statistical hypotheses concerning several parameters when the number of observations is large”. *Transactions of the American Mathematical society* 54:3, 1943, pages 426–482.
DOI: 10.1090/S0002-9947-1943-0012401-3

143. J. Aleksić et al. “Optimized dark matter searches in deep observations of Segue 1 with MAGIC”. *Journal of Cosmology and Astroparticle Physics* 2014:02, 2014, page 008.
DOI: 10.1088/1475-7516/2014/02/008

144. M. Ahnen et al. “Indirect Dark Matter Searches in the Dwarf Satellite Galaxy Ursa Major Ii With the Magic Telescopes”. *Journal of Cosmology and Astroparticle Physics* 2018:03, 2018, pages 009–009.
DOI: 10.1088/1475-7516/2018/03/009

145. A. Abramowski et al. “H.E.S.S. constraints on dark matter annihilations towards the sculptor and carina dwarf galaxies”. *Astroparticle Physics* 34:8, 2011, pages 608–616. ISSN: 0927-6505.
DOI: 10.1016/j.astropartphys.2010.12.006

146. J. Binney and S. Tremaine. *Galactic dynamics*. Vol. 20. Princeton university press, 2011. ISBN: 9781400828722

147. J. F. Navarro, C. S. Frenk, and S. D. M. White. “The Structure of Cold Dark Matter Halos”. *The Astrophysical Journal* 462:nil, 1996, page 563.
DOI: 10.1086/177173

148. M. Meyer, D. Horns, and H.-S. Zechlin. “The Crab Nebula As a Standard Candle in Very High-Energy Astrophysics”. *Astronomy & Astrophysics* 523:nil, 2010, A2.
DOI: 10.1051/0004-6361/201014108

149. J. Aleksić et al. “Measurement of the Crab Nebula spectrum over three decades in energy with the MAGIC telescopes”. *Journal of High Energy Astrophysics* 5, 2015, pages 30–38.
DOI: 10.1016/j.jheap.2015.01.002

150. E. Aliu et al. (VERITAS Collaboration). “VERITAS Deep Observations of the Dwarf Spheroidal Galaxy Segue 1”. 85, 2012, page 062001.
DOI: 10.1103/PhysRevD.85.062001

Glossary

AEFF Effective Area. Component of the IRF, that describes the detector efficiency. 51, 52, 70, 71, 87

EDISP Energy Dispersion. Component of the IRF, that models the quality of the energy reconstruction. 51, 70

K_0 Modified Bessel function of the second kind. 18

PSF Point Spread Function. Component of the IRF, that models the quality of the directional reconstruction. 51, 54, 57, 59, 70

S/N Signal-to-noise ratio. 60, 61

Φ Cumulative distribution of the standard gaussian distribution. 83

α Confidence level. Propertion of estimated intervals, that contain the true parameter. 83

β Relative velocity expressed in units of c_0. 18, 19

δ Angle between telescope pointing and geomagnetic alignment. 51

$\langle \sigma v \rangle$ thermally-averaged annihilation cross-section. 80

$\mu(\omega)$ Frequency-dependent permeability. 19

μ_0 Vacuum permeability, physical constant. 18

μ A scale parameter for the assumed signal. 83, 103

σ_μ Standard deviation of the strength parameter μ. Relates to the distribution of the test-statistic in the asymptotic case. 83

σ Significance of a detection according to [119]. 60

θ Distance to the zenith, 90 deg - altitude. 37, 51, 59

$c(\omega)$ Speed of light in matter. Generally lower than c_0 and varying with frequency. 18

c_0 Speed of light in vacuum. 18, 20, 103

$n(\omega)$ Frequency-dependent index of refraction of a medium. 19

`ExcessMapEstimator` Computes correlated excess and significance maps. For details, see the Online documentation. 76, 77, 112

`LST-OSA` Onsite processing framework. Online documentation. 35

`Tophat2DKernel` Isotropic smoothing filter implemented in astropy. Online Documentation. 76

`acceptance_modelisation` Software to model the telescope background. Development on github. 62

`astropy` Community Python Library for Astronomy. Online documentation. 26

`ctapipe` Low-level data processing pipeline for CTAO. Online Documentation. 26, 31, 88, 104

`gammapy` Core library for the CTAO Science tools. Online documentation. ii, 26, 65, 69–71, 76, 80, 87

`iminuit` Python-interface to the Minuit2 ibrary. Online documentation. 70, 83

`lstchain` Main analysis pipeline for the LST-1 based on `ctapipe`. Development on Github. ii, 26, 31, 35, 41, 43–45, 51, 62, 88

`lstmcpipe` Software to orchestrate lstchain scripts on the slurm cluster. Online Documentation. 42

`matplotlib` Library for creating static, animated, and interactive visualizations in Python. Online documentation. 26

`numpy` Fundamental package for scientific computing in Python. Online documentation. 26

`pandas` Library providing high-performance, easy-to-use data structures and data analysis tools. Online documentation. 26

`pybkgmodel` Software to model the telescope background. Development on Github. 62

`pyirf` Prototype for the generation of Instrument Response Functions. Online documentation. 26

`scikit-learn` Machine-learning framework in python. Online Documentation. 26, 43, 44

`scipy` Open-source software for mathematics, science, and engineering. Online documentation. 26

cgNFW-Profile Generalized version of the NFW-Profile with a cored central region. 81, 85

Cherenkov light Emission produced during the passage of charged particles through a dielectric medium if the local speed of light is exceeded. 27, 37, 41, 48, 52

Crab Nebula Remnant of a supernova from 1054. Consists of the nebula with steady gamma-ray flux and a pulsar in the center. 5, 34, 62

dynamic cleaning Dynamic cleaning. The threshold is calculated relative to the brightest pixels. Implemented here. 32

Fermi Gamma-ray Space Telescope Space observatory for gamma rays up to $\approx$ 300 GeV. Formerly called: Gamma-ray Large Area Space Telescope (GLAST). 9, 15

Gamma-Ray Burst Short, violent phenomena leading to a very high flux of gamma rays for up to a few hours. 34

Jeans-analysis Method to constrain the gravitational potential using gravitationally bound objects. For a detailed overview read for example [146]. 81

loss-function Objective function to minimize in the statistical analysis of data, e.g. in model fitting. 43

M87 Target source analyzed in this thesis. Can refer to the AGN or the galaxy depending on the scientific context. 34, 36

Monte Carlo period Timeframe, for which a set of simulations is deemed valid. 42

NFW-Profile Standard profile for the modeling of dark-matter halos going back to Julio Navarro, Carlos Frenk and Simon White [147]. 80, 81, 84, 104

off-observation Observation, that is not pointed towards a known source. Instead, a dark patch of the sky is observed to understand the background acceptance. 34

pedestal event Events that are triggered in fixed timeframes. Since genuine showers are rare compared to the size of the readout window, these events contain mostly electronic noise and can be used to calibrate the camera. 36

Random Forest Ensemble of randomized decision trees. Here, the scikit-learn implementation is used. Online documentation. 43

Roque de los Muchachos Mountain on the canary island La Palma. Location of MAGIC, LST-1 and other telescopes. 22

shifters People operating the telescope during night-time for the purpose of data-taking. Groups stay on the island for $\approx$ 3 weeks between full moon phases. Every such period is called a shift, hence the name shifters. 35, 39

Slurm Workload Manager Workflow management system. Online documentation. 35

tailcuts cleaning Image cleaning used for LST data. Implemented here. 31

time-delta cleaning Time delta cleaning. Implemented here. 31, 32

Whipple 10m-telescope Fred Lawrence Whipple Observatory. Located at Mount Hopkins and constructed in 1968. 5

wobble-distance Offset between pointing position and assumed source position. Observing multiple offset positions allows for a simultaneous background estimation and similar source exposure in different parts of the F.o.V.. 35, 52, 55, 88

Acronyms

4FGL fourth Fermi Large Area Telescope catalog. 4, 12

ADC analog-to-digital converter. 27, 28

AGN Active Galactic Nucleus. 9, 10, 13, 15, 105

c.o.g. center of gravity. 65

CMB Cosmic Microwave Background. 9

CORSIKA COsmic Ray SImulations for KAscade. 41

CTAO Cherenkov Telescope Array Observatory. ii, 3, 21–23, 26, 27, 29, 52, 87, 88, 104

DL0 datalevel 0. 29

DL1 datalevel 1. 29, 31–33, 35, 36, 41, 42

DL1A datalevel 1 a (cleaned images). 32

DL1B datalevel 1 b (image parameters). 32, 41, 43

DL2 datalevel 2. 41, 48, 50, 51

DL3 datalevel 3. 26, 41, 51, 59, 61, 71

DL4 datalevel 4. 69, 73, 75

DRS4 Domino Ring Sampler 4. 27, 28

EHT Event Horizon Telescope. 13, 14

ESO European Southern Observatory. 22

F.o.V. Field of View. 32, 34–37, 42, 50, 52–54, 59, 62–67, 71, 72, 81, 88, 106, 111

H.E.S.S High Energy Stereoscopic System. 22, 62, 78, 79

HAWC High-Altitude Water Cherenkov. 17

HEGRA High-Energy-Gamma-Ray Astronomy. 14

IACT Imaging Atmospheric Cherenkov Telescope. ii, 5, 15, 17–22, 25, 35, 36, 41, 50, 52, 54, 80, 87

ICRS International Celestial Reference System. 15, 71

IRF Intrument Response Function. 51, 52, 59, 62, 63, 65, 71, 87, 103

KASCADE KArlsruhe Shower Core and Array DEtector. 41

l.o.s. line-of-sight. 12

L0 level 0 trigger. 28

L1 level 1 trigger. 28

Lidar Light imaging, detection and ranging. 37–39

LST Large-Sized Telescope. 21–23, 62, 83, 88

LST-1 Large-Sized Telescope Prototype. ii, 3, 23, 26–29, 34, 35, 37, 42, 48, 52, 54, 55, 59, 62, 65, 78, 87, 88, 104, 105, 111

MAGIC Major Atmospheric Gamma Imaging Cherenkov (Telescopes). 15, 23, 28, 37, 42, 54, 55, 62, 78, 79, 87, 105, 111

MEG Mu to Electron Gamma. 27

MSE mean squared error. 44, 45

MST Medium-Sized Telescope. 22, 23

NSB Night-Sky Background. 29, 35–37, 111

OGADF open gamma-ray astro data format. 26, 52, 54

p.e. photon count equivalents. 29–31, 38, 39, 42

PCA Principal Component Analysis. 34

PMT photomultiplier tube. 27, 28, 42

R0 raw data-level 0. 26, 28

R1 raw data-level 1. 29

SCB slow control board. 28

simtel sim-telarray. 41, 42

SST Small-Sized Telescope. 22, 23

TIB Trigger Interface Board. 28

VERITAS Very Energetic Radiation Imaging Telescope Array System. 14, 79

WIMP Weakly Interacting Massive Particle. 80

Crab Nebula

As discussed in Section 2.8, the Crab Nebula is, at the current point in time, a worst-case scenario for constructing a background-model at least with the method described here due to the string signal coupled with a currently still poor directional reconstruction. At low energies, the signal events that are reconstructed outside of the exclusion region create hard to deal with artifacts in the count maps. In addition, the F.o.V. for observations of the Crab Nebula is notably brighter than for M87, which requires the use of fine-tuned simulation.

However, here I used the same setting for the analysis of the simulations and the training of the models as for the main analysis. The analysis is performed using a slightly different, closer declination line and therefore also different models compared to the M87 analysis, but lacks the fine-tuning of simulated images to match the higher NSB-level. These normally need to be performed to minimise mismatches between simulations and observations. This certainly influences the results especially at low energies where the images are less bright compared to the background noise than at high energies.

With this in mind, I analyzed some sample observations of the Crab Nebula to make sure the results are at least sensible and to understand where things begin to fall apart for a bright source. A reasonable, albeit not perfect description is achieved upwards from 200 GeV. This is shown in Figure 1, where some issues in the background can still be made out. At 400 GeV, the background seems to be well modeled (Figure 2).

In Figure 3, the measured excess is fitted to a LogParabola-model along with often cited reference spectra. At low energies, the reconstructed flux is significantly higher than the one observed by MAGIC, which often acts as a reference. This has, to differing degrees, been observed in all LST-1-analyses. Using only events in the source region or at energies where the background is well described changes the results only slightly.

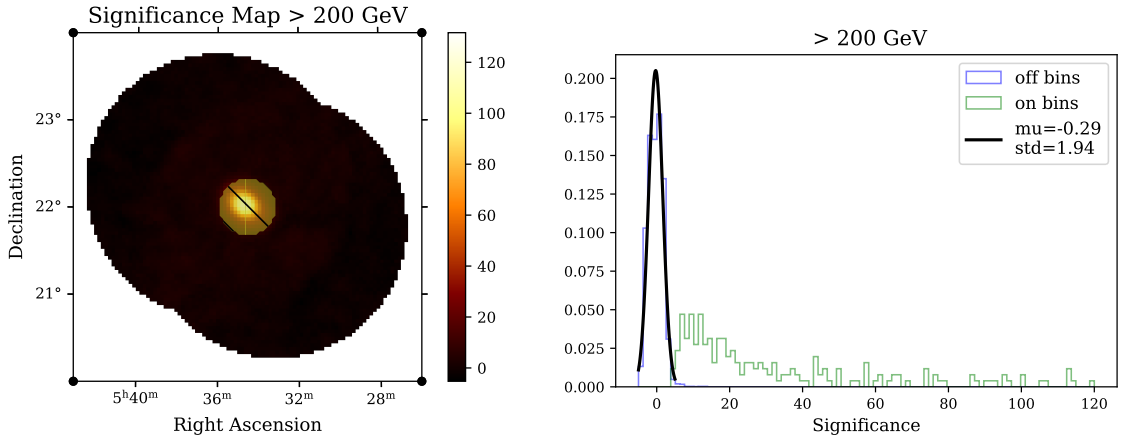

Figure 1: Spatial significance values as estimated with the `ExcessMapEstimator` above 200 GeV. Left: Spatial distribution. Right: Histogram of significances in the on- and off-regions. The on-region is indicated on the left.

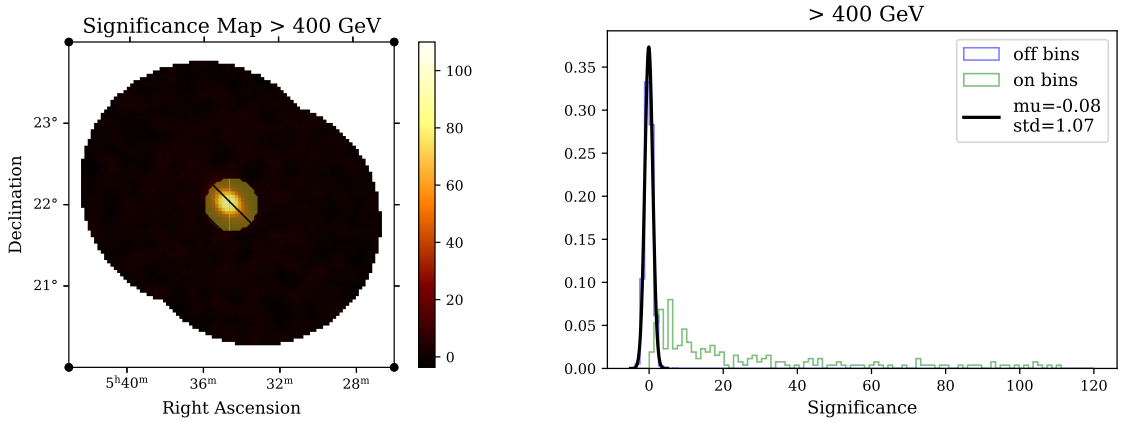

Figure 2: Spatial significance values as estimated with the `ExcessMapEstimator` above 400 GeV. Left: Spatial distribution. Right: Histogram of significances in the on- and off-regions. The on-region is indicated on the left.

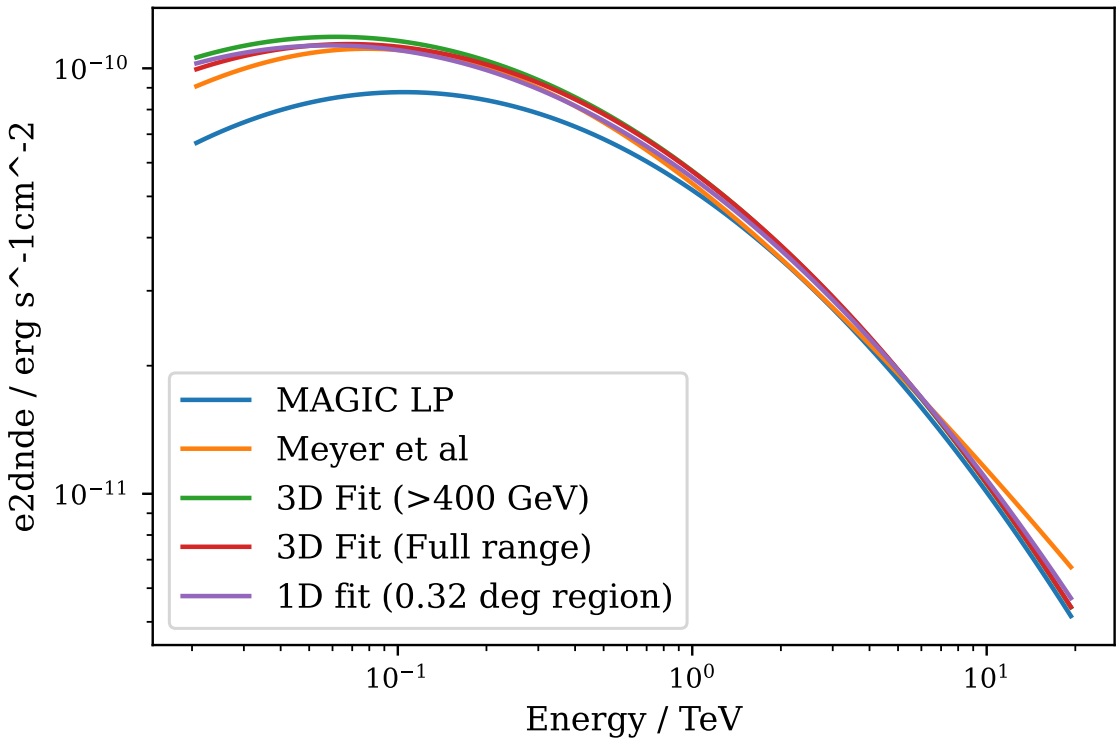

Figure 3: Log-Parabola fit of the Crab Nebula Spectrum performed on a small sample of observations. In the one-dimensional case, only the events within the source region contributes, which removes some events, that are reconstructed further away at low energies. The reference spectra are the ones from [148] and [149].

Validation of Asimov Approximation

Here, the validity of the asymptotic approximation in Section 3.5 is checked. For different masses of the dark matter particle and annihilation channels, the asymptotic description of the test statistic is compared to the test statistic calculated on different statistical realisations of the background and source models. In all cases, the asymptotic formulae from [140] accurately describe the distributions.

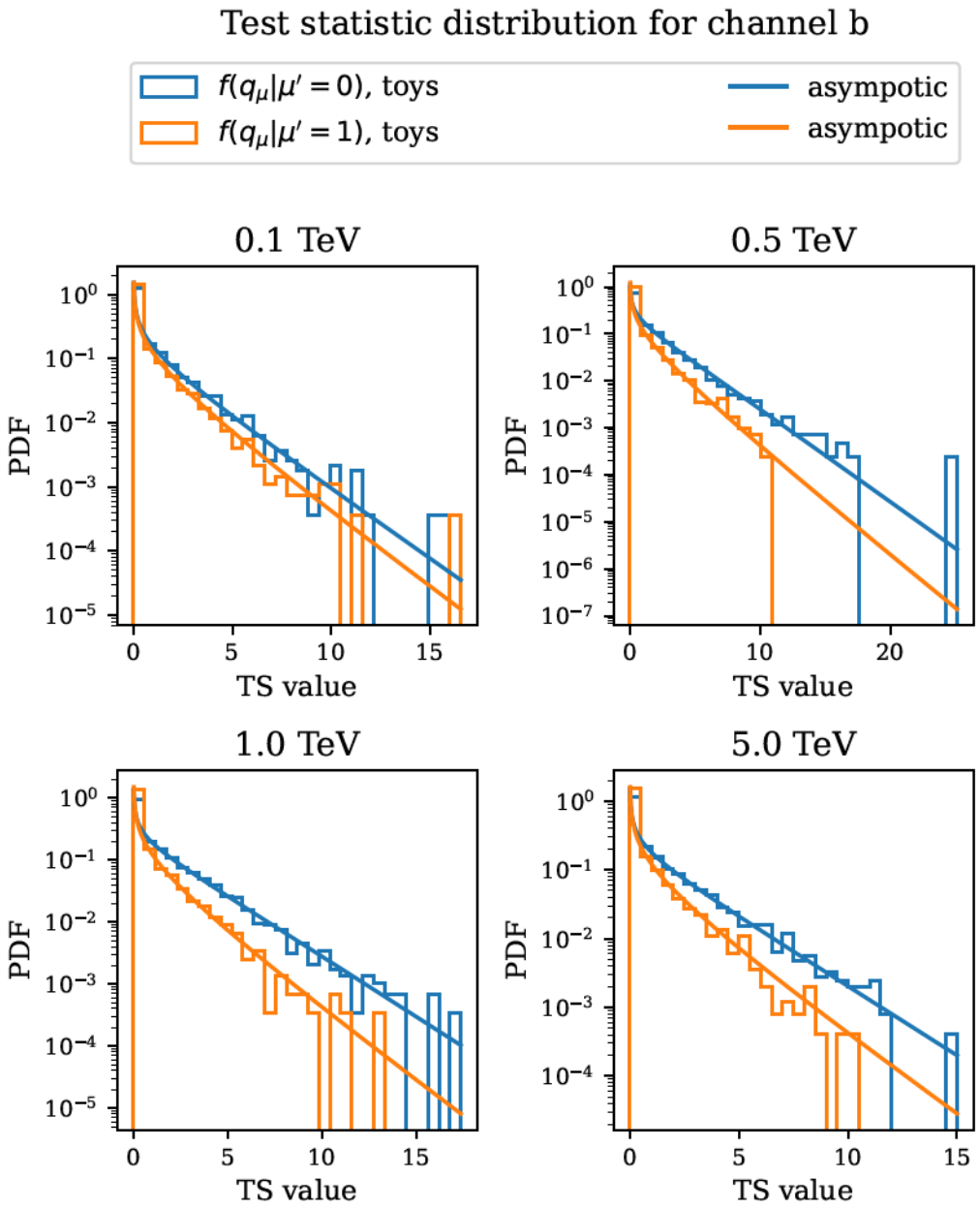

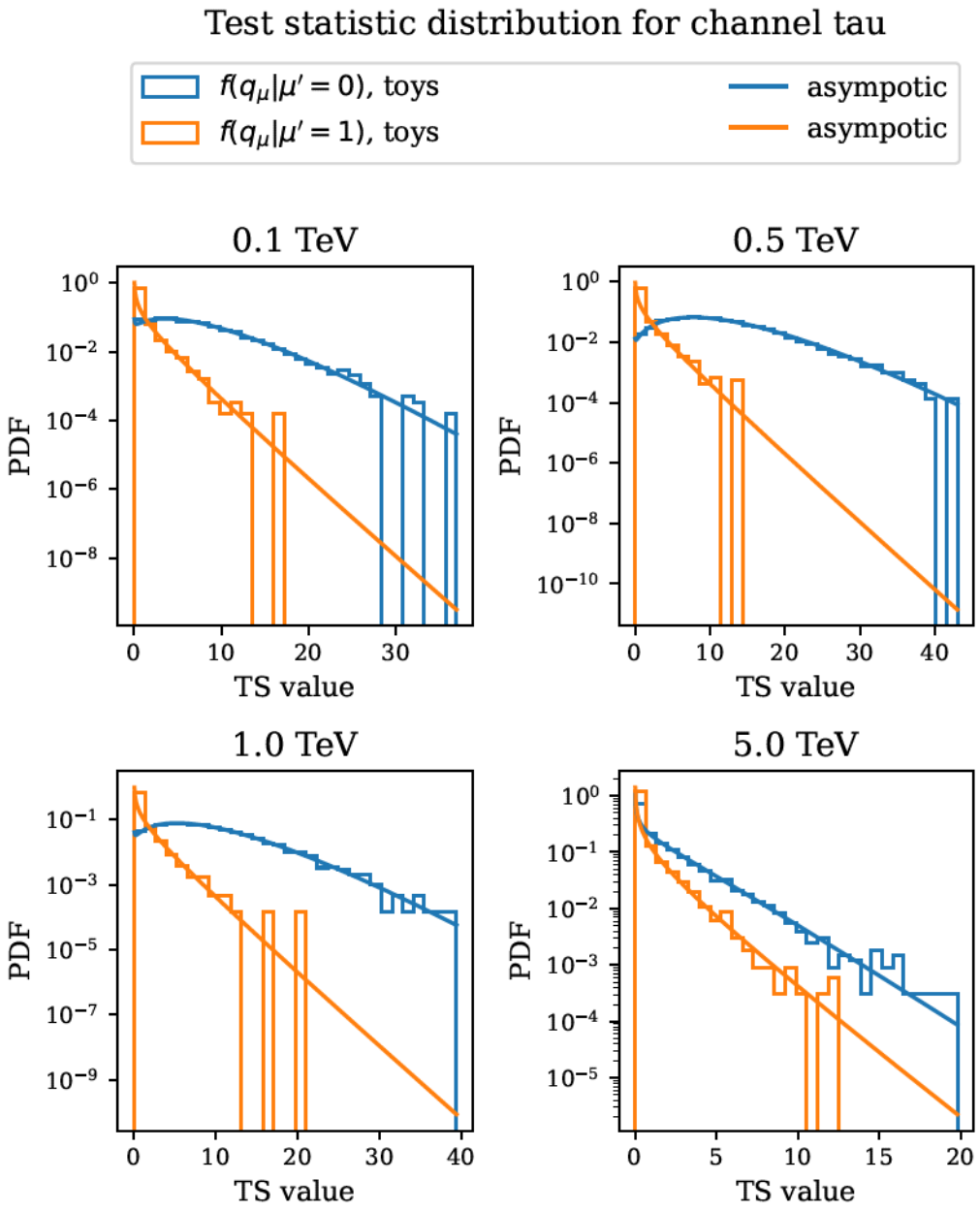
Test statistic distribution for channel tau
$f(q_\mu|\mu'=0)$, toys
$f(q_\mu|\mu'=1)$, toys
asympotic
asympotic
0.1 TeV
0.5 TeV
1.0 TeV
5.0 TeV
PDF
TS value

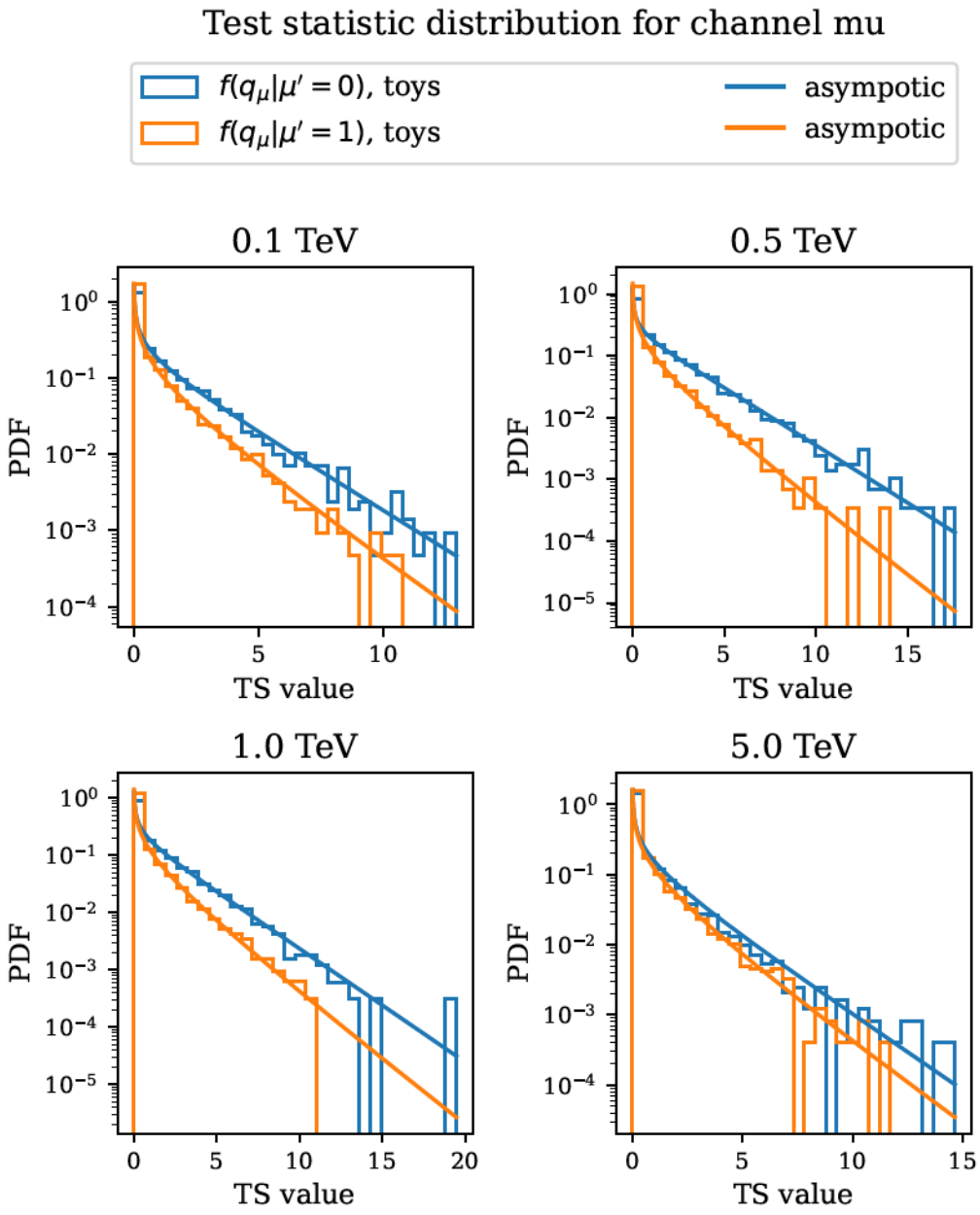
Test statistic distribution for channel mu
$f(q_\mu|\mu'=0)$, toys
$f(q_\mu|\mu'=1)$, toys
asympotic
asympotic
0.1 TeV
0.5 TeV
1.0 TeV
5.0 TeV
PDF
TS value

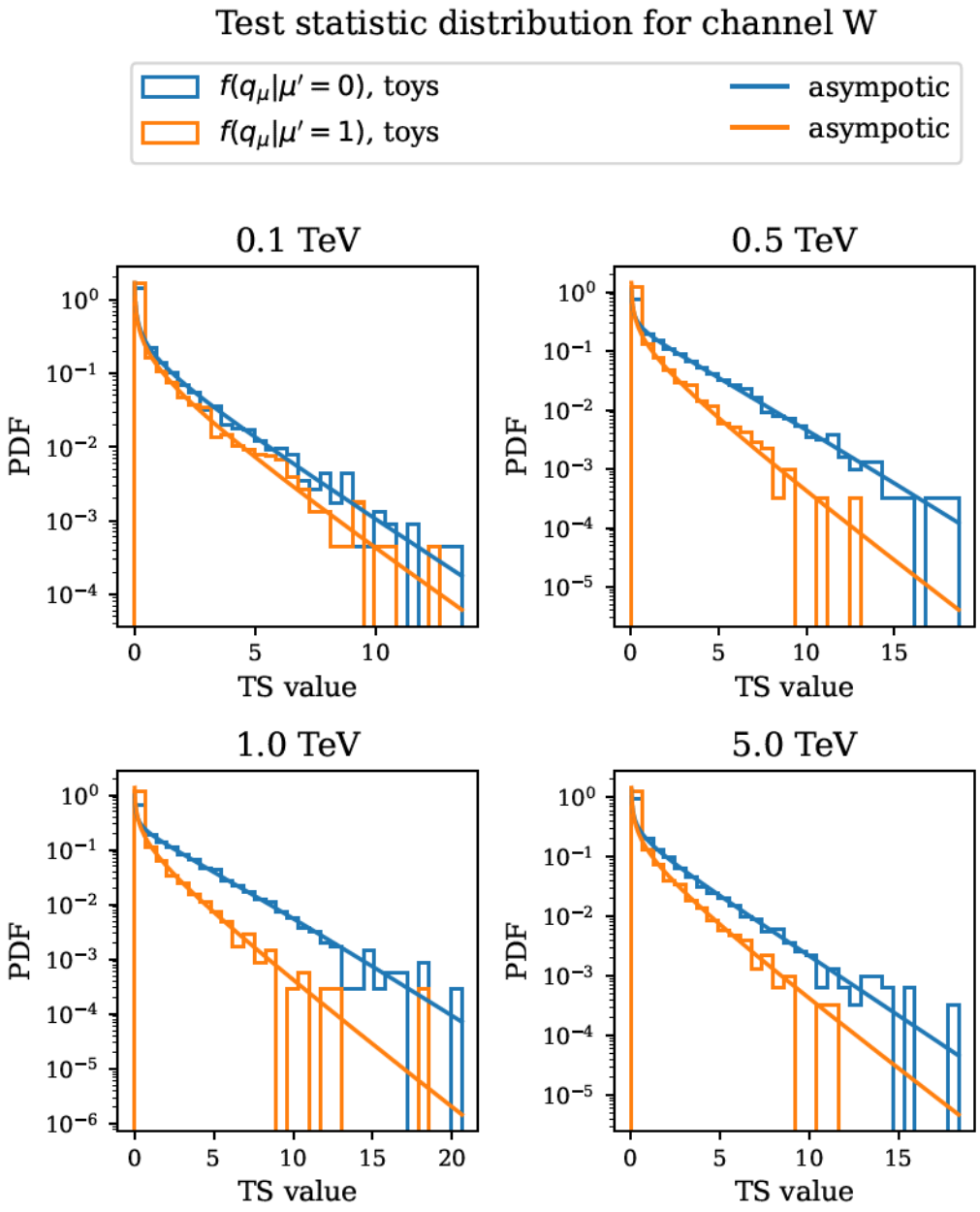
Test statistic distribution for channel W
$f(q_\mu|\mu'=0)$, toys
$f(q_\mu|\mu'=1)$, toys
asympotic
asympotic
0.1 TeV
0.5 TeV
1.0 TeV
5.0 TeV
PDF
TS value

Dummy Limits on Segue 1

Purely to put the performance of the analysis / telescope into perspective, I calculated the expected upper limits for a halo that resembles the one of Segue-1 using the instrument response and background from this M87 analysis and assuming ten times the observation time. This would be a setup similar to the one used in [143].

In practice, the diffuse emission from the milky way and the comparatively large extension of the source would likely complicate the analysis. On top of that, they include some systematic uncertainties, which are omitted here. Nevertheless, it is interesting and reassuring to see that the limits in this case are competitive with the ones published in that paper and [150].

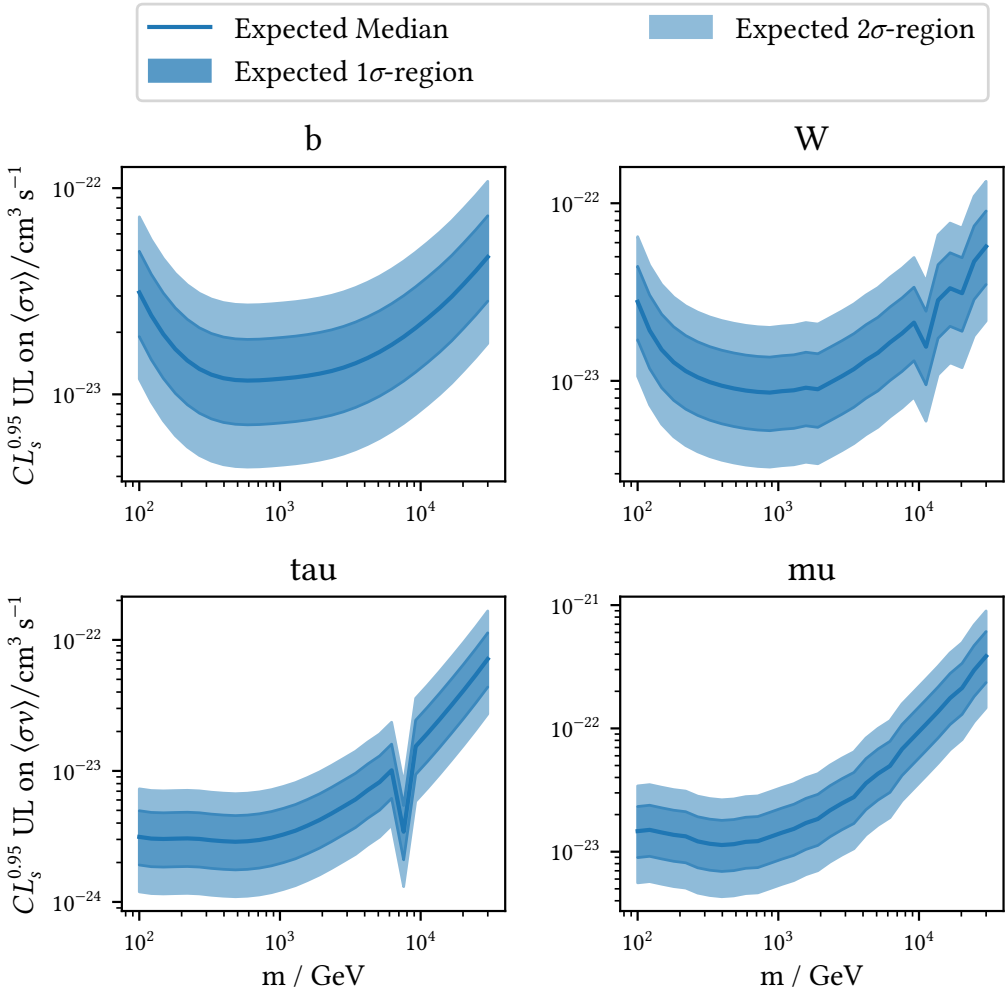

Figure 4: Hypothetical upper limits for a segue 1 observation with 10 times the observation time.

Configuration Files

Pipeline


```
{
  "production": "20230901_v0.10.4_allsky_base_prod",
  "declination": "dec_931",
  "lstchain_enviroment": "../envs/lstchain.yml",
  "n_off_regions": 1,
  "train_size": 0.4
}
```


Data Selection


```
{
  "source": "M87",
  "source_ra_deg": 187.70593076,
  "source_dec_deg": 12.39112329,
  "pedestal": { "ul": 2, "ll": 1, "sigma": null },
  "cosmics": { "ul": 8000, "ll": 2000, "sigma": null },
  "cosmics_10": { "ul": 80, "ll": 20, "sigma": null },
  "cosmics_30": { "ul": 8, "ll": 2, "sigma": null },
  "time_start": "2020-01-01",
  "time_stop": "2024-02-01",
  "max_zenith_deg": 90,
  "never_include": [3744, 4507, 4508, 4509, 7185, 7186, 7187, 7188, 7189]
}
```


lstchain


```
{
  "source_config": {
    "EventSource": {
      "allowed_tels": [1],
      "max_events": null
    },
    "LSTEventSource": {
      "default_trigger_type": "ucts",
      "allowed_tels": [1],
      "min_flatfield_adc": 3000,
      "min_flatfield_pixel_fraction": 0.8,
      "calibrate_flatfields_and_pedestals": false,
      "EventTimeCalculator": {
        "dragon_reference_counter": null,
```

```
      "dragon_reference_time": null
    },
    "PointingSource": {
      "drive_report_path": null
    },
    "LSTR0Corrections": {
      "calib_scale_high_gain": 1.088,
      "calib_scale_low_gain": 1.004,
      "drs4_pedestal_path": null,
      "calibration_path": null,
      "drs4_time_calibration_path": null
    }
  }
},
"events_filters": {
  "intensity": [80, Infinity],
  "width": [0, Infinity],
  "length": [0, Infinity],
  "wl": [0, Infinity],
  "r": [0, Infinity],
  "leakage_intensity_width_2": [0, 0.2],
  "event_type": [32, 32]
},
"n_training_events": {
  "gamma_regressors": 1.0,
  "gamma_tmp_regressors": 0.5,
  "gamma_classifier": 0.5,
  "proton_classifier": 1.0
},
"tailcut": {
  "picture_thresh": 8,
  "boundary_thresh": 4,
  "keep_isolated_pixels": false,
  "min_number_picture_neighbors": 2,
  "use_only_main_island": false,
  "delta_time": 2
},
"tailcuts_clean_with_pedestal_threshold": {
  "picture_thresh": 8,
  "boundary_thresh": 4,
  "sigma": 2.5,
  "keep_isolated_pixels": false,
  "min_number_picture_neighbors": 2,
```

```
    "use_only_main_island": false,
    "delta_time": 2
  },
  "dynamic_cleaning": {
    "apply": true,
    "threshold": 267,
    "fraction_cleaning_intensity": 0.03
  },
  "random_forest_energy_regressor_args": {
    "max_depth": 30,
    "min_samples_leaf": 10,
    "n_jobs": -1,
    "n_estimators": 150,
    "bootstrap": true,
    "criterion": "squared_error",
    "max_features": "auto",
    "max_leaf_nodes": null,
    "min_impurity_decrease": 0.0,
    "min_samples_split": 10,
    "min_weight_fraction_leaf": 0.0,
    "oob_score": false,
    "random_state": 42,
    "verbose": 0,
    "warm_start": false
  },
  "random_forest_disp_regressor_args": {
    "max_depth": 30,
    "min_samples_leaf": 10,
    "n_jobs": -1,
    "n_estimators": 150,
    "bootstrap": true,
    "criterion": "squared_error",
    "max_features": "auto",
    "max_leaf_nodes": null,
    "min_impurity_decrease": 0.0,
    "min_samples_split": 10,
    "min_weight_fraction_leaf": 0.0,
    "oob_score": false,
    "random_state": 42,
    "verbose": 0,
    "warm_start": false
  },
  "random_forest_disp_classifier_args": {
```

```
    "max_depth": 30,
    "min_samples_leaf": 10,
    "n_jobs": -1,
    "n_estimators": 100,
    "criterion": "gini",
    "min_samples_split": 10,
    "min_weight_fraction_leaf": 0.0,
    "max_features": "auto",
    "max_leaf_nodes": null,
    "min_impurity_decrease": 0.0,
    "bootstrap": true,
    "oob_score": false,
    "random_state": 42,
    "verbose": 0,
    "warm_start": false,
    "class_weight": null
  },
  "random_forest_particle_classifier_args": {
    "max_depth": 30,
    "min_samples_leaf": 10,
    "n_jobs": -1,
    "n_estimators": 100,
    "criterion": "gini",
    "min_samples_split": 10,
    "min_weight_fraction_leaf": 0.0,
    "max_features": "auto",
    "max_leaf_nodes": null,
    "min_impurity_decrease": 0.0,
    "bootstrap": true,
    "oob_score": false,
    "random_state": 42,
    "verbose": 0,
    "warm_start": false,
    "class_weight": null
  },
  "energy_regression_features": [
    "log_intensity",
    "width",
    "length",
    "x",
    "y",
    "wl",
    "skewness",
```

```
    "kurtosis",
    "time_gradient",
    "leakage_intensity_width_2",
    "az_tel",
    "alt_tel"
  ],
  "disp_method": "disp_norm_sign",
  "disp_regression_features": [
    "log_intensity",
    "width",
    "length",
    "wl",
    "skewness",
    "kurtosis",
    "time_gradient",
    "leakage_intensity_width_2",
    "az_tel",
    "alt_tel"
  ],
  "disp_classification_features": [
    "log_intensity",
    "width",
    "length",
    "wl",
    "skewness",
    "kurtosis",
    "time_gradient",
    "leakage_intensity_width_2",
    "az_tel",
    "alt_tel"
  ],
  "particle_classification_features": [
    "log_intensity",
    "width",
    "length",
    "x",
    "y",
    "wl",
    "signed_skewness",
    "kurtosis",
    "signed_time_gradient",
    "leakage_intensity_width_2",
    "log_reco_energy",
```

```
    "reco_disp_norm",
    "reco_disp_sign",
    "az_tel",
    "alt_tel"
  ],
  "allowed_tels": [1],
  "write_pe_image": false,
  "mc_image_scaling_factor": 1,
  "image_extractor": "LocalPeakWindowSum",
  "image_extractor_for_muons": "GlobalPeakWindowSum",
  "CameraCalibrator": {
    "apply_waveform_time_shift": false
  },
  "time_sampling_correction_path": "default",
  "LocalPeakWindowSum": {
    "window_shift": 4,
    "window_width": 8,
    "apply_integration_correction": true
  },
  "GlobalPeakWindowSum": {
    "window_shift": 4,
    "window_width": 8,
    "apply_integration_correction": true
  },
  "timestamps_pointing": "ucts",
  "train_gamma_src_r_deg": [0, Infinity],
  "source_dependent": false,
  "mc_nominal_source_x_deg": 0.4,
  "mc_nominal_source_y_deg": 0.0,
  "volume_reducer": {
    "algorithm": null,
    "parameters": {}
  },
  "calibration_product": "LSTCalibrationCalculator",
  "LSTCalibrationCalculator": {
    "systematic_correction_path": null,
    "squared_excess_noise_factor": 1.222,
    "flatfield_product": "FlasherFlatFieldCalculator",
    "pedestal_product": "PedestalIntegrator",
    "PedestalIntegrator": {
      "sample_size": 10000,
      "sample_duration": 100000,
      "tel_id": 1,
```

```
      "time_sampling_correction_path": null,
      "charge_median_cut_outliers": [-10, 10],
      "charge_std_cut_outliers": [-10, 10],
      "charge_product": "FixedWindowSum",
      "FixedWindowSum": {
        "window_shift": 6,
        "window_width": 12,
        "peak_index": 18,
        "apply_integration_correction": false
      }
    },
    "FlasherFlatFieldCalculator": {
      "sample_size": 10000,
      "sample_duration": 100000,
      "tel_id": 1,
      "time_sampling_correction_path": null,
      "charge_product": "LocalPeakWindowSum",
      "charge_median_cut_outliers": [-0.5, 0.5],
      "charge_std_cut_outliers": [-10, 10],
      "time_cut_outliers": [2, 38],
      "LocalPeakWindowSum": {
        "window_shift": 5,
        "window_width": 12,
        "apply_integration_correction": false
      }
    }
  },
  "waveform_nsb_tuning": {
    "nsb_tuning": false,
    "nsb_tuning_ratio": 0.52,
    "spe_location": "lstchain/data/SinglePhE_ResponseInPhE_expo2Gaus.dat"
  }
}
```

IRFs

```
{
  "DL3Cuts": {
    "max_gh_cut": 0.8,
    "min_gh_cut": 0.3,
    "gh_efficiency": 0.9
  },
  "IRFFITSWriter": {
    "energy_dependent_theta": false,
```

```
    "energy_dependent_gh": true,
    "point_like": false,
    "overwrite": true
  },
  "DataReductionFITSWriter": {
    "source_ra": "187.70593076 deg",
    "source_dec": "12.39112329 deg"
  },
  "DataBinning": {
    "fov_offset_min": 0.0,
    "fov_offset_max": 2.0,
    "fov_offset_n_edges": 6,
    "true_energy_min": 0.02,
    "true_energy_max": 20,
    "true_energy_n_bins": 15,
    "reco_energy_min": 0.02,
    "reco_energy_max": 20,
    "reco_energy_n_bins": 15
  }
}
```

Background Model

```
hdu_type: "3D"
prefix: "bkg"

# This is not relly applied. I assign the groups in the notebook
# run_matching:
#  zenith_bin_edges:
#    [0, 90]

binning:
  offset:
    max: "3 deg"
    n_bins: 60
    n_offset_bins: 8
  energy:
    min: "20 GeV"
    max: "20 TeV"
    n_bins: 15
```

Source Exclusion

```
# Region file format: DS9 astropy/regions
global include=1
icrs
circle(187.70593076,12.39112329,0.32000000)
```

Gammapy

```yaml
general:
  log:
    level: info

observations:
  datastore: build/M87/dl3/analysis-thesis
  obs_time:
    start: "2021-01-01"
    stop: "2025-01-01"
  required_irf:
    - aeff
    - edisp
    - bkg

datasets:
  type: 3d
  stack: False
  geom:
    wcs:
      skydir: { frame: icrs, lon: 187.70593076 deg, lat: 12.39112329 deg }
      binsize: 0.04 deg
      width: { width: 4.0 deg, height: 4.0 deg }
      binsize_irf: 0.4 deg
    selection: { offset_max: 2.5 deg }
    axes:
      energy:
        min: 20 GeV
        max: 20 TeV
        nbins: 15
      energy_true:
        min: 20 GeV
        max: 20 TeV
        nbins: 15
  background:
    method: "fov_background"
```

```
    parameters: { "method": "fit" }
    exclusion: build/M87/dl4/analysis-thesis/bkg_exclusion.fits.gz
  on_region:
    {
      frame: icrs,
      lon: 187.70593076 deg,
      lat: 12.39112329 deg,
      radius: 0.2 deg,
    }
  containment_correction: false
  safe_mask:
    methods:
      - "offset-max"
      - "aeff-max"
    parameters:
      offset_max: "1.5 deg"
      aeff_percent: 5
fit:
  fit_range: { min: 20 GeV, max: 10 TeV }

flux_points:
  energy: { min: 20 GeV, max: 10 TeV, nbins: 20 }
  source: M87

light_curve:
  energy_edges: { min: 100 GeV, max: 10 TeV, nbins: 1 }
  source: M87
```

DM Profiles

```
NFW:
- error: 0
  frozen: false
  interp: lin
  is_norm: false
  max: .nan
  min: .nan
  name: r_s
  scale_method: scale10
  unit: kpc
  value: 128.4
- error: 0
  frozen: false
  interp: lin
```

```
    is_norm: false
    max: .nan
    min: .nan
    name: rho_s
    scale_method: scale10
    unit: GeV cm-3
    value: 0.09776320321196776
  cgNFW:
  - error: 0
    frozen: false
    interp: lin
    is_norm: false
    max: .nan
    min: .nan
    name: r_s
    scale_method: scale10
    unit: kpc
    value: 412.1
  - error: 0
    frozen: false
    interp: lin
    is_norm: false
    max: .nan
    min: .nan
    name: rho_s
    scale_method: scale10
    unit: GeV cm-3
    value: 0.002184667192283346
  - error: 0
    frozen: false
    interp: lin
    is_norm: false
    max: .nan
    min: .nan
    name: r_c
    scale_method: scale10
    unit: kpc
    value: 19.0
  - error: 0
    frozen: false
    interp: lin
    is_norm: false
    max: .nan
```

```
min: .nan
name: gamma
scale_method: scale10
unit: ''
value: 2.39
```

Acknowledgments

First, I would like to thank Prof. Dr. Dr. Wolfgang Rhode for providing me with this unique opportunity and for always acting in the best interest of your students! No matter the time or nature of the problem, you are always there to help us out. I also want to thank Prof. Dr. Johannes Albrecht not only for acting as a second supervisor, but more for sparking my interest in particle physics. It was primarily the great KET-lecture, that lead to me recognizing experimental particle physics as the exciting and versatile field that it is.

My gratitude goes to everyone at the chair of astroparticle physics. It was a challenging time, but everyone of you contributed to also make it entertaining and educational. In particular, I want to thank Dominik and Max for making me recognize the possibility of pursuing a PHD in the first place and for introducing me into the field and collaborations. I also want to thank Andrea and Sarah for supporting us all and enabling us to focus on the fun parts of the job!

Thank you, Noah, for countless very interesting discussions about science, vim configuration and everything, and also all of the useful tips for writing and staying focused when things inevitably become difficult. In a similar vein, I want to thank Simone for helping me figure out all of the good, bad and ugly about background modeling. You two also made the lunch-breaks that much more enjoyable at the TUrnpunkt! I also have not forgotten your effort to keep the tradition alive after the group fell apart, Anno.

Beyond that, I want to thank and applaud Stefan for spending months on reading a single research paper and discussing all of the relevant statistical concepts with me. Your perserverance is really inspiring. I also want to thank Rune for helping me time and time again with the SMD-basics and informing me about every upcoming Electric Callboy release, whether I cared or not. Although the dark-matter arc somewhat came to a halt, I also want to thank Céline and David for taking the time to discuss every question I could come up with.

Of course, all of this would not have been possible without the support of the people closest to me: Thank you, Anne, for always being supportive and understanding and thanks to everyone in my family, especially my parents, for being patient with me! I know that you did not see me as much as you wished for during this period and I will do my best to find a better balance in the future!

Funding Acknowledgments:
This work was supported by the BMBF ErUM-Pro and the federal state of North Rhine-Westphalia. I also want to thank the Collaborative Research Center SFB 876, Collaborative Research Center SFB 1491, and the Lamarr Institute for Machine Learning and Artificial Intelligence for supporting the research group.